SCUOLA DI DOTTORATO
UNIVERSITÀ DEGLI STUDI DI MILANO-BICOCCA

Department of Earth and Environmental Sciences (DISAT)

PhD program Chemical Sciences Cycle XXXII

Curriculum in Chemical Sciences

Nanostructured materials for secondary alkali metal ion batteries

Surname Fiore Name Michele

Registration number 788799

Tutor: Ruffo Riccardo

Supervisor: Giorgio Moro

Coordinator: Maria Luce Frezzotti

ACADEMIC YEAR 2018/2019

Declaration of Originality

I hereby declare that I am the sole author of the work here enclosed and that I referenced and acknowledged it. In addition I declare that this document has never been submitted as it is to other institution for qualifications.
Michele Fiore

Acknowledgments

One can but hope they will fail. What are you raving about?

Acronyms

LIBs	Lithium Ion Batteries
SIBs	Sodium Ion Batteries
KIBs	Potassium Ion Batteries
XRD	X-Ray Diffraction
IEA	International Energy Agency
IPCC	International Panel on Climate Change
PSH	Pumped Storage-Hydroelectricity
USA	United States of America
LCO	Lithium Cobalt Oxide
NMC	Lithium Nickel Manganese Cobalt Oxide
LFP	Lithium Iron Phosphate
LMO	Lithium Manganese Oxide
NCA	Lithium Nickel Cobalt Aluminum Oxide
USD	United States Dollar
HEVs	Hybrid Electric Vehicles
EVs	Electric Vehicles
DRC	Democratic Republic of Congo
CEA	Commissariat à l'énergie atomique et aux énergies alternatives

CNRS	Centre national de la recherche scientifique
emf	electromotive force
HOMO	Highest Occupied Molecular Orbital
LUMO	Lowest Unoccupied Molecular Orbital
SEI	Solid Electrolyte Interface
ESW	Electrochemical Stability Window
WISe	Water In Salt Electrolyte
PHEVs	Plug-in Hybrid Electric Vehicles
SSI	Stationary Energy Storage
SEM	Scanning Electron Microscopy
HRTEM	High Resolution Transmission Electron Microscopy
EDX	Energy Dispersive X-Ray Spectroscopy
MRS	Micro Raman Spectroscopy
CCD	Charge-Coupled Device
JCPDS	Joint Committee on Powder Diffraction Standards
XPS	X-Ray Photoelectron Spectroscopy
ACS	American Chemical Society
FEC	Fluoroethylene Carbonate
SAED	Selected Area Electron Diffraction
PAN	Polyacrylonitrile
DMF	N-N-Dymethylformammide
TEOS	Tetraethyl Ortosilicate
GCPL	Galvanostatic cycling with potential limitation
PCGA	Potentiostatic Cycling with Galvanostatic Acceleration
EIS	Electrochemical Impedance Spectroscopy

PAA	Polyacrylic Acid
SOC	State of Charge
CPE	Constant Phase Element
Li-K-FSI	Lithium or Potassium bis(fluorosulfonil)imide
Li-K-TFSI	Lithium or Potassium bis(trifluoromethanesulfonil)imide

Abstract

Lithium-ion batteries currently dominate the market of power sources for portable devices, thanks to their superior energy and power density. The economy of scale and engineering optimizations have driven the cost of LIBs below the 200 $/KWh at the pack level. This catalyzed the market penetration of electric vehicles and made them a viable candidate for stationary energy storage. The rapid market expansion of LIBs however, has raised growing concerns about the future sustainability of this technology. In particular, lithium and cobalt supplies are considered vulnerable, primarily because of the geopolitical implications of their high concentration in only a few countries. In the search for the next generation secondary batteries, the so called *post-lithium ion batteries*, alternatives that do not use rare metals have been extensively investigated in the last 10 years. Sodium-ion batteries attracted considerable attention thanks to the high abundance of the precursors and wide distribution of sodium in the earth's crust. Indeed, if sodium ion secondary batteries can be made practical, a significant relaxation in the constraints on reserves and a great reduction in environmental impact are expected. As it will be pointed out during the dissertation, it is not straightforward to allocate the reduction of the price of the alkali metal ion precursors to the reduction of the battery price. However, the difficulties in the supply of raw materials for LIBs, such as shortages in lithium carbonate and cobalt ores, could make lithium- and cobalt-free systems, such as SIBs and KIBs, attractive and cost-competitive alternatives. Compared to other, more exotic chemistry including Ca^{2+}, Mg^{2+} and Al^{3+} batteries, SIBs are nowadays considered one of the most promising alternative to LIBs. As a matter of fact, excellent performances in terms of both energy and capacity retention have been achieved with cobalt-free cathodes. Despite the extensive research, anode materials for SIBs still represent a serious problem for the commercial exploitation of this technology.
The present doctoral research on SIBs was focused on anode materials, with a particular attention towards conversion oxides. A feature that makes this materials worthy of consideration is their high sodium uptake per formula

unit, making them excellent candidates for high energy sodium-ion batteries. Compared to intercalation materials, conversion-based ones are more challenging to deal with because of the high volume variation during cycling. The expansion and contraction that occurs during cycling can lead to the loss of electric contact between the electrode components, eventually resulting in fast capacity fading. This challenge is addressed by nanostructuring and morphology control, which proved to significantly reduce the pulverization of the active material.
Different anode candidates have been studied during the doctoral work. Despite being far from practical applications because of the high cost of the precursors, cobalt oxide nanofibers have been here explored as a first prototype for conversion materials in sodium ion batteries. The sodiation-desodiation mechanism was analyzed by means of *ex situ* XRD which led to a deeper understanding of the conversion reaction in SIBs. A cost-effective and environmentally benign alternative based on iron oxide was thereafter taken into account. The limits of iron (III) oxide were tackled by combining the advantages of nanostructuring and doping with an aliovalent element. In particular Si-doped Fe_2O_3 nanofibres were synthesized via an easy scalable process based on the electrospinning method. Far from being a pure electrochemical investigation, the effect of silicon doping was reviewed. It was found that Si-addition improved the transport properties as well as induced changes in the crystal structure and morphology.
In the final section of the thesis, potassium-ion batteries (KIBs) were examined as a promising alternative to sodium-ion batteries. KIBs exhibit all the benefits of SIBs, with the additional advantage that graphite, the commercial standard anode material in LIBs, can reversibly accommodate K-ions. On the positive side, prussian blue analogues, and more specifically, potassium manganese hexacyanoferrate (KMnHCFe), has been reported to provide high operating voltages and satisfactory capacity retention. The proposed research activity presented the use of an ionic liquid based electrolyte compatible with the most promising anode and cathode for KIBs. In addition, a high-throughput optimization of the KMnHCFe synthesis is reported. Different concentrations of precursors, chelating agent (K-citrate) and potassium chloride were used to tune the crystal nucleation and growth of the PBA. Selected candidates were then fully characterized, and their electrochemical properties investigated. A significant correlation between the particle size, vacancy content, and capacity is reported. The optimized material exhibits the highest ever reported coulombic efficiency for the KMnHCFe. This find opens up the possibility of highly efficient, high energy potassium ion batteries.

List of Figures

List of Tables

Contents

Chapter 1

Introduction

1.1 Objective of the thesis

The total energy consumption by the entire human civilization has risen to unprecedented levels. Energy production and consumption are some of the major challenges that mankind is facing. Highly efficient energy storage technologies, and in particular secondary batteries, play a momentous role in automotive, industry, and renewable energy sources exploitation. The present research contributes to the investigation of the *post-lithium secondary alkali-metal ion batteries*, namely sodium-ion (SIBs) and potassium-ion batteries (KIBs). Advantages and disadvantages of both the technologies are examined, and experimental work undertaken to synthesize and characterize advanced electroactive materials is presented after an appropriate review of the most recent related literature. A particular attention was given to chemical-physical-electrochemical properties correlations which are essential for an appropriate understanding and development of new materials. This latter approach was applied to conversion based materials for sodium ion batteries (namely cobalt and iron oxides). Their morphology was controlled using a highly-scalable synthesis method and the effect of nanostructuring on the electrochemical properties was investigated. In addition, the reaction mechanism was studied by means of electrochemical methods and *ex-situ* X-ray diffraction, highlighting the importance of the intermediates that form upon sodiation/de-sodiation. Regarding the research on potassium ion batteries, the rationale selection of the electrolyte and the investigation of a wide parameter space for the synthesis of the most promising cathode for KIBs, led to highly efficient and stable electrochemical performances. The reaction mechanism resulting in the excellent capacity retention was finally investigated via *operando* XRD.

1.2 Structure of the thesis

The report of the doctoral activity has been intentionally divided into two main sections. The first half of the thesis will present the subject of study, and will provide to the reader the required notions for the full comprehension of the research activity. The second half, core of the dissertation, will present the experimental activity carried out during the PhD.
Chapter II briefly describes the current world energy landscape and the key energy storage technologies. Particular attention is given to pros and cons of electrochemical energy storage. The major challenges that this technology is facing nowadays are analyzed, together with the motivation for switching from Lithium-ion to Sodium- or Potassium-ion batteries.
Chapter III describes the most important theoretical notions that will allow the reader to fully comprehend the experimental described later on.
Chapter IV and *Chapter V* review the major literature findings for Sodium-ion and Potassium-ion batteries.
Chapter VI reports the experimental work carried out on Co_3O_4. Despite the fact that cobalt oxide will be hardly employed as anode material for SIBs because of the high price of cobalt precursors, the material has been chosen as a prototype for the investigation of conversion materials. The consequences of an intermediate phase on the electrochemical properties are reported and analyzed.
Chapter VII focuses on the environmentally friendly iron oxide as a promising conversion-based anode material for SIBs. Rather than addressing the limits of iron (III) oxides through the synthesis of carbon composites, extensively investigated in literature, the effect of combining the advantages of the nanostructuring and the doping with an aliovalent element on the electrochemical performances is reported.
Chapter VIII outlines the extensive research activity carried out on graphite and potassium manganese hexacyanoferrate, respectively the most promising anode and cathode for KIBs. The careful selection of the electrolyte and the optimization of the cathode synthesis opens up the possibility of highly efficient potassium ion batteries.
Finally, *chapter IX* reviews the doctoral work and draws conclusions and perspectives for future research.

Chapter 2

World energy landscape and grid energy storage

2.1 Introduction

This introductory chapter provides a brief description of the world energy landscape. The attention is be primary directed to the global energetic problem that humanity is facing nowadays. In particular, the reasons why stationary energy storage is becoming a key technology for the increasing integration of renewable energy sources on the grid system are evaluated. The different available technologies are be thereafter analyzed, with a particular attention to electrochemical energy storage. Finally, a due description of the pathway that led to the success of electrochemical storage technologies, such as lithium-ion batteries that currently dominate the market of portable devices, is be presented together with the major limitations, and possible solutions, that still hinder their full exploitation for grid storage.

2.2 World Energy Outlook

Major transformations are underway for the global energy sector, from growing electrification and expansion of renewables (with solar photo-voltaic charging ahead), to oil markets that are entering a period of renewed uncertainty and volatility, including a possible supply gap in the early 2020s.[1] Demand for natural gas is on the rise, erasing talk of a glut as China emerges as a giant consumer. However, there is no single pathway for how the world will use energy in the coming decades. Indeed, across all regions and fuels, policy choices made by governments will determine the shape of the future energy system.

Global energy consumption steadily increased over the last years (Figure

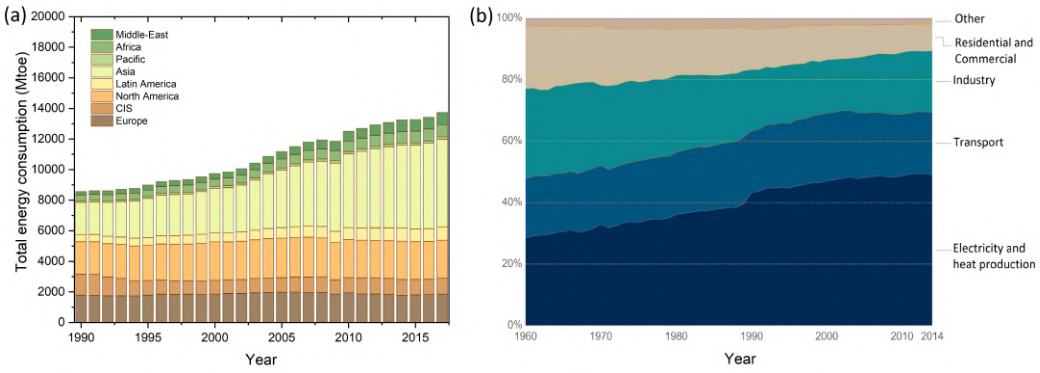

Figure 2.1: (a) Global energy consumption in different regions of the world in Million of tonnes of Oil Equivalent (Mtoe) between 1990 and 2017; (b) evolution of the CO_2 emissions by source between 1960 and 2014. Source: International Energy Agency, *IEA*

2.1a). The demand is set to grow by more than 25% by 2040, with the majority of growth coming from developing economies, led by India. Interestingly, low carbon technologies and natural gas are likely to cover more than 80% of this increase in demand.[1] Nevertheless, global carbon emissions, and in particular those associated with energy and heat production, keep on rising (Figure 2.1b), with Asia, and in particular China, representing the dominant source of emissions since the early 2000s.[2]. Moreover, the world falls short of achieving universal energy access and improve air quality.

The increased emission of CO_2 and other greenhouse gasses as a result of human activity has already produced measurable consequences on the energetic balance of our planet. This is related to the increasing amount of energy irradiated by the sun being trapped by the carbon dioxide richer atmosphere and transformed in thermal agitation, producing quantifiable local temperature anomalies. In this scenario, it is understandable how political interest in climate change rose from the late 1980s when scientific concerns about global warming grew. In 1988 the International Panel on Climate Change (IPCC) was established and new global climate change policies where gradually undertaken by the governments. These efforts culminated in the subscription of the so called *Kyoto Protocol* (1997) and in the *Paris agreement* (2015). However, the agreements were not always binding and the many differences in countries' perceptions on how the problem should be dealt with (in par-

[1] IEA data: https://www.iea.org/weo2018/
[2] IEA data: https://www.iea.org/statistics/co2emissions/

ticular the differences between developed and developing countries) have so far limited the effectiveness of climate change policies. Based on the existing and announced policies, the world is currently not on track to meet main energy-related components of the Sustainable Development Goals.[3] Reaching climate goals means wind and solar power generators growing faster, with the share of renewables in the power mix rising to two thirds by 2040 up from a quarter today. It means almost 1 billion electric cars on the road by 2040, compared to 4 million today. This requires new technologies such as carbon capture, utilization and energy storage to enter the scene on a vast scale.
Renewable energy sources are the world fastest growing energy sources, however a severe drawback and a limit to future increased share in energy production is their inherently intermittent nature.[1] If renewables are to become the major source of energy in the next century, capturing energy produced at one time for use at a latter time (Energy Storage) can become essential to guarantee a reliable grid system.
In terms of power, grid energy storage appears nowadays dominated by pumped-storage hydroelectricity (PSH) (Figure 2.2). Although this tech-

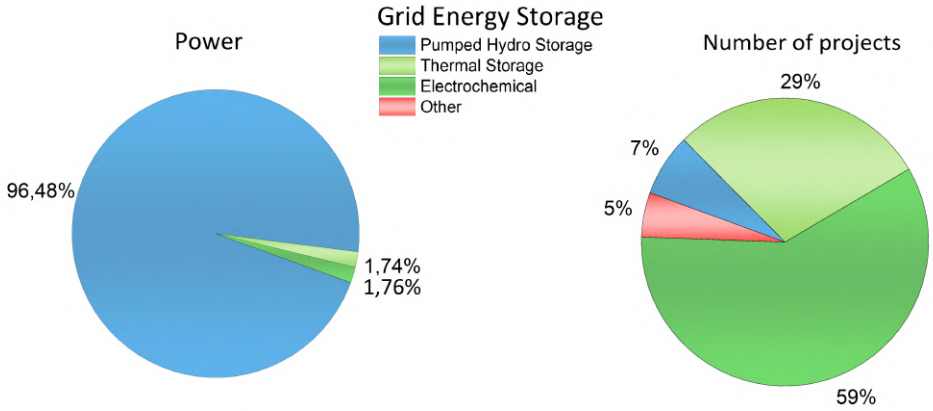

Figure 2.2: Power and relative number of projects currently online, divided by the major sources. Source: Global Energy Storage Database, *https://www.energystorageexchange.org/*

nique is by many reported as the most cost-effective way of storing large amounts of electrical energy, the high capital cost and the significant geographical restrictions (low energy density of pumped storage requires a large natural body located nearby, and either large flows or large differences in height between reservoirs) are critical factors that may stunt the future expansion of this technology. The benefits of long service life (up to 75 years) of

[3] IEA data: https://www.iea.org/sdg/renewables/

PHS, are counterbalanced by a round-trip energy efficiency between 70-80%, significantly lower than the over 90% efficiency achieved by electrochemical energy storage (EES). In the last 20 years numerous new projects were set up to rely on thermal and electrochemical energy storage rather than PHS. In particular EES, thanks to its additional high flexibility and fast response can be surprisingly advantageous. Domestic energy storage, for example, can represent a beneficial shortcut between energy production and consumption. Complete-or at least partial grid autonomy, might be achieved coupling local exploitation of renewable energy sources with in-place battery storage. Moreover, a capillary penetration of secondary batteries for commercial and residential buildings (these alone represent around 40% of the total energy consumption), setting up the so called *smart-grid*, would limit waste and increase energy utilization efficiency. And all of this would require smaller infrastructures and therefore lower investments pro-capite. Nevertheless, several obstacles limit the full exploitation of secondary batteries for grid energy storage. Firstly, choosing which battery chemistry would be more suitable for a stationary energy storage application is not trivial. Secondly, reliability and service life need to be improved. Finally, the cost per kWh (although significantly decreased over the years) is often still too high for practical applications. To obtain a better grasp on how rechargeable batteries ended up to be an essential technological asset in modern society, an instructive description of their birth and development is provided in the next section.

2.3 Brief history of batteries

In a letter dated 20 March 1800 addressed to the President of the Royal Society of London, Alessandro Volta announced to the world scientific community the invention of the 'electric pile', the device that would reshape the concept of energy source. At the same time a new discipline was born: electrochemistry. The origin of electrochemitry is romantically related to the work of Luigi Galvani, since it triggered Volta's attention towards a work he would have maybe never undertaken.[2] As a matter of fact, when Volta reproduced Galvani's classic experiment in which a frog's leg twitches when touched by a series of two different metals, the result grasped Volta's interest. As an accurate thinker that he was, he then started to selectively analyze one experimental variable at a time, soon realizing that Galvani's theory to explain the discovery was unfounded: this was the beginning of the famous Galvani-Volta controversy that went on until Galvani's death in 1798. Volta was convinced that the frog was an extremely sensitive electrometer, capable of revealing quantities of electricity that other instruments were unable to

detect. Wanting to scientifically prove the existence of such an electrification, Volta started to think about how to amplify the effect. This was the beginning of the path that lead him to the 'pile'.[3]
Volta's work had a tremendous impact on the progress of the electrochemical science by catalyzing the rapid evolution of batteries with the discovery of many important electrochemical systems. In 1866 Georges-Lionel Leclanché unveiled his work on a battery based on a zinc rod anode and a manganese oxide-carbon mixture as a cathode, immersed in a aqueous ammonium chloride solution.[4] Interestingly, the same concept is still used in the commonly known Carbon-Zinc and Alkaline primary batteries (Figure 2.3). Soon after

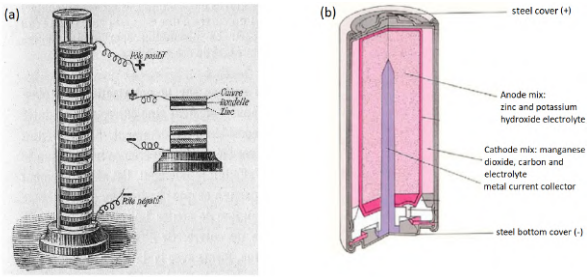

Figure 2.3: Schematic representation of: (a) the Volta pile (b) a modern alkaline battery (c) a zinc-carbon battery

Lechalnche discovery, the French scientist Gaston Plamte invented in 1859 the lead-acid secondary battery and, in 1901, the Swedish engineer Waldmar Jungner proposed the Nickel-Cadmium battery. These two systems are also the base of the batteries used nowadays respectively for car ignition and in portable electronics. After the Leclancé, Jungner and Plantè discoveries not much innovation took place as those systems met the requirements of the contemporary technology. The situation changed in the late 1960s due to a series of new needs in portable energy devices:

1. the progress of implantable medical devices that needed high energy density and long lasting reliable energy sources;

2. the need, for military purposes, of high energy and high power sources;

3. the increasing market request, of consumer electronic devices.

The most crucial fault of conventional batteries was the lack of high energy density (i.e. Watt-Hours stored per unit of weight and volume). The example of pacemakers is significant. This device had to rely on two zinc-mercury batteries in series.[5] As a result, it was very heavy, bulky and the batteries

run down their charge in two years, meaning it had to be replaced by a new surgical procedure, with serious stress for the patients. The breakthrough arrived with the development of a new battery that exploited lithium. This kind of battery coupled a lithium metal anode with a iodine-base cathode (i.e. lithium-iodine battery), and provided an energy density of about 250 $Wh{\cdot}kg^{-1}$, almost five times higher than that of zinc mercury oxide. The new developed batteries had a tremendous impact on the pacemaker's efficiency since it resulted in a great reduction of weight and volume, as well as operational life (extended to 6 to 7 years, Figure 2.4).[6]

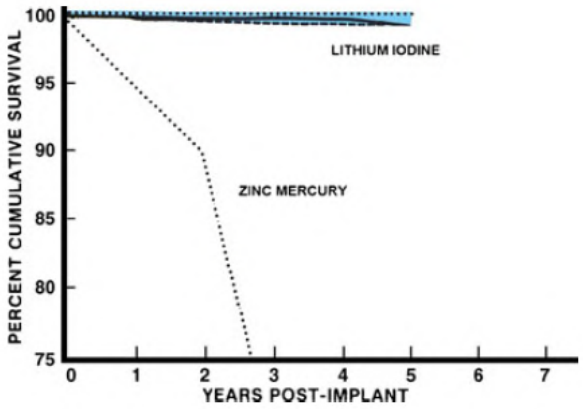

Figure 2.4: Comparison between the durability of an early zinc-mercury oxide and lithium-iodine batteries for pacemakers

2.3.1 The early stage of lithium-ion batteries

The success of the lithium-iodine system paved the route for a new family of batteries that could meet the requirements for a wide diffusion of consumer electronic devices. In this initial stage the batteries generally employed a manganese dioxide cathode and a metallic lithium anode,[7] and were of primary type. However, an obvious interest stimulated the research for secondary systems. The breakthrough came in 1978 with the development of the *insertion* (or *intercalation*) materials.[8] This class of materials can reversibly accept and release lithium ions in and out of their structure: a reversible evolution of both the electronic and crystal structure is required. Transition metal compounds, such as titanium sulfide, can exchange lithium ions through its layered structure, and this process is associated with a change in the valence state of the transition metal. Exploiting this type of materials, the firsts secondary batteries that used liquid organic electrolytes appeared

in the market between the late 1970s and the early 1980s. However, some operational faults, including fire accidents, soon suggested that some problems associated with the anode prevented safe and long operation of these batteries. Due to its high reactivity, lithium metal reacts with the electrolyte to form a lithium permeable passivation layer on its surface (the so called 'Solid Electrolyte Interface' or 'SEI'); however irregularities on its surface may lead to uneven plating and stripping of lithium and, as a consequence, dendrite formation, that eventually grow and short the system. In extreme cases, these events can overheat the battery, causing thermal runaway and explosion. Two different options were possible to solve these safety issues: (1) a choice of an electrolyte that assured optimized lithium deposition and avoided shorts or (2) replacement of the lithium metal with a more stable anode active material. The feasibility of the first choice was demonstrated by Armand in 1978 who proposed a polymer-lithium salt (e.g. lithium triflate and poly(ethylene oxide), *PEO*) complex.[9−10] Later on, this concept was exploited by Hydro Québec in Canada and 3M Company in the USA that used a laminated battery module based on lithium metal as an anode. Despite this and other successful projects, the lithium polymer battery hardly found commercialization, mainly because the risks associated with its operation were never fully overcome. The second and winning-approach relied on a new concept that considered the combination of two insertion electrodes. During charge, the negative electrode can accommodate lithium ions and the positive one acts as a lithium source, whereas in discharge the process is reversed. The electrochemical process of the cell involved the transfer of lithium cations between the two electrodes. If fully understood, this system is actually a concentration cell in which lithium ions *rock* across the electrodes: a new type of system was born, the so called *lithium rocking chair battery*. The concept of a rocking chair battery dates back to the late 1970s and its practical use demonstrated after a few years. However, more than 10 years were required to reach the consumer market thanks to Sony Corporation in 1991.[11,12,13] The fundamental discovery for the success of the rocking chair battery was provided by Goodenough (that won Nobel prize in 2019) when he proposed the $LiCoO_2$ cathode. Although other cathode materials have been developed, most of the commercial production of lithium rocking chair batteries still relies on lithium cobalt oxide. Only recently, with the rising concerns regarding the Cobalt supply chain and refining, manufacturers are shifting to different cathode chemistries, particularly for automotive and grid storage applications (Figure 2.5).[14]

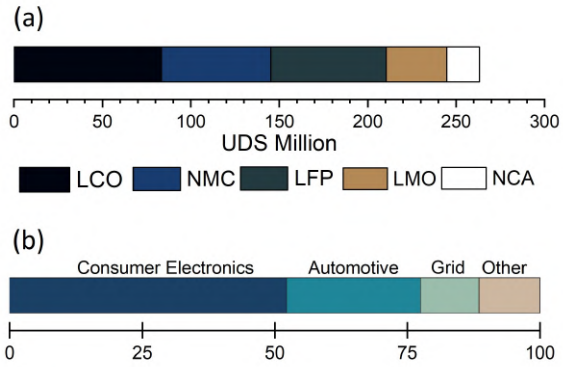

Figure 2.5: (a) U.S. Lithium-ion battery raw materials market size by cathode materials; (b) Lithium ion battery market: application analysis. Source: Lithium-ion battery market analysis and segment forecast to 2025, *Grand View Research Inc*, 2018.

2.3.2 The market of Lithium ion batteries and recent applications

Thanks to their specific properties, mainly in terms of energy density, lithium ion batteries overtook both conventional (e.g. Nickel-Cadmium) and younger systems (e.g. Nickel-Metal Hydride).[15] it is therefore not surprising that the global lithium-ion battery market exploded after their commercialization in 1991(Figure 2.6), reaching over 24 Billion USD in 2016. Their success for a vast number of applications also emerges from their versatility. Indeed, multiple cathode (e.g. $LiFePO_4$,$LiCoO_2$,$LiMn_2O_4$,$LiNiCoAlO_2$) and anode (e.g. graphite, Si-graphite, $Li_4Ti_5O_{12}$) chemistries are currently available.[14]

2.3.3 The new era and the concerns on raw materials for LIBs

The outstanding success, however, does not mark the end of LIBs. Once the market of consumer electronics is conquered, new challenges appear in the future of these devices. The continuous decrease of oil resources and the growing concern on climate changes call for a larger use of green, alternative energy sources. Further, the replacement of internal combustion cars with more efficient, controlled emissions vehicles, such as hybrid electric vehicles (HEVs) and full electric vehicles (EVs) depicts a specific demand from our society. On the other hand, renewable resources are intrinsically intermit-

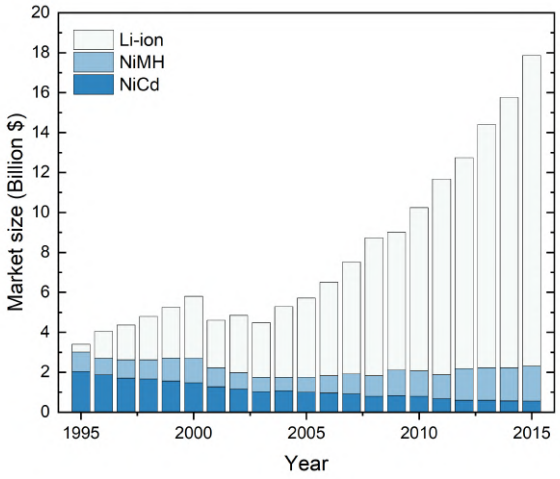

Figure 2.6: The market of rechargeable batteries. Comparison between Li-ion, Nickel metal Hydride (NiMH) and Nickel Cadmium (NiCd) batteries between 1995 and 2015. Source: Avvicenne Energy

tent and their discontinuity in operation requires suitable storage systems to efficiently run renewable energy plants. In this scenario LIBs, thanks to their high-energy efficiency, appear as the ideal candidates for this purpose. However, although these batteries are established commercial products, further research and development is required to improve their performance and meet the new requirements. In particular, improvements in safety, cost, and energy density are needed.

Tesla is the first company that made their performing lithium batteries the core technology of high-end full electric vehicles. They also incorporated LIBs in stationary storage devices for medium-small scales, especially for domestic use. This made electrochemical storage available for uses that, if coupled with local and even domestic renewable energy sources, can surpass the current energy network. This transition towards a green-energy future with the associated sustained growth in the demand of LIBs within transportation and stationary storage sectors, motivates detailed investigations on whether future raw materials supply will reconcile with resulting material requirements for these batteries.[14] Scientists indeed, started questioning the future sustainability of a lithium economy: will lithium, with the exponential increase in the row material demand, become the new gold?[16] Moreover, not only lithium but also the supply of each of the elements used in LIBs must be considered, as they together represent between 70% and 85% of the total

cell cost. About half of that 80% is due to the anode and cathode active materials (Figure2.7).[14]

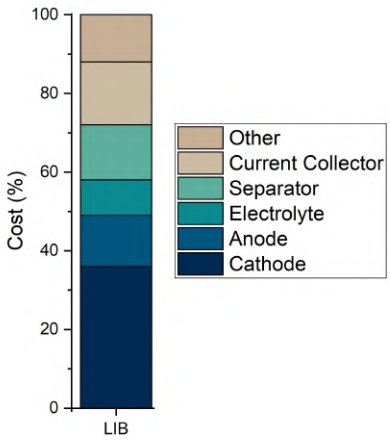

Figure 2.7: Manufacturing cost for LIBs divided per single contribution to the overall cost

Although a full socio-economical analysis of the supply chain of the elements needed to for a full LIB is beyond the scope of this work, the most important ones such as Li, Mn, Co, Ni and C will be shortly considered.
Figure 2.8(a) shows on the y axis what is generally called 'static depletion index' that represents the reserves for each element (defined as the part of a resource base that could be economically extracted or produced in 2017), normalized by annual mine production, plotted versus the fraction of mining that comes from the top producing country. The lower and more concerning values for this figure come from Ni and Mn; however, they have been relatively constant over a 15-year time period, suggesting that the demand can drive the supply towards continued economical extraction. The x axis, instead, indicates how much of the total production of one element is geographically concentrated. Low values indicate a geographically diversified material supply, while high values correspond to geographically concentrated resources. It can be seen that the supply of Co and natural graphite are the most concentrated with respectively 50% and over 65% of the production coming from the top country. This is shown also in Figure 2.8(b) where it can be seen that the majority of Co, C as well as Li extraction come from only a few countries. These concentrations have been considered concerning, as one factor that normally makes a material critical is the possibility of

supply disruptions caused by government policy or socio-political instability. Based on this brief exploration, potential concerns for Co, natural graphite

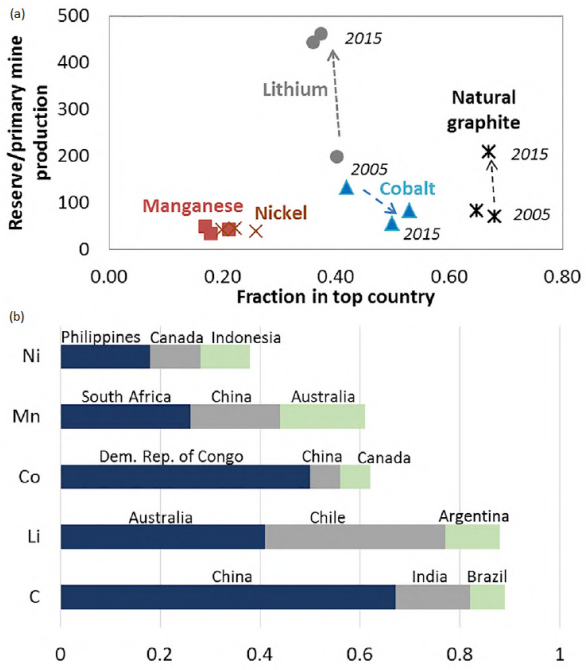

Figure 2.8: (a) Static metrics of resource use for Ni,Mn,Co,Li and natural graphite fraction in top country versus static depletion over time; (b) Production fraction by country.[14]

and Li may arise, whereas no detectable supply concerns are found for Ni or Mn, which is consistent with other reports presented in literature.
Natural graphite, whose static depletion index increased significantly in recent years, has multiple end of uses that include refractory applications, steel-making, brake linings and batteries, which requires flake and spherical graphite. This diversity in demand implies a low battery use of natural graphite (up to 10% in 2014).[17] The major concern regarding graphite is that over 65% of its production is concentrated in China (for this reason the European Commission included graphite among its critical mineral raw materials in 2010).[18] However, the crustal abundance of graphite is quite high (there is potential for increased production in India, United Stated, Brazil and through Africa), and synthetic graphite can be substituted to natural graphite (although the price is almost the double, according to some estimates).
The production and availability of Co is generally considered more concern-

ing, as Cobalt is produced as by-product or co-product of Ni and Cu. According to an estimate by the Cobalt Developement Instituton in 2015, half of Cobalt production can be attributed to the Ni industry, 35% to the Cu industry and 9% to other metals (including the platinum group), while only 6% comes from primary Co production.[19] If the demand for Ni and Cu were to drop, one could expect a reduction in Co production from the main suppliers. In addition, since over 50% of world mining production comes from Democratic Republic of Congo (DRC), the Co supply can be greatly affected by the geopolitical stability of this country. In the 1970s, for example, institutional inefficiency and political unrest led to supply disruptions of cobalt. This, combined with increasing Co demand and decreasing producer inventories, caused prices to increase by over 400%. Although the supply disruption was only temporary and the year-end production of Co from DRC exceeded the previous year's production, the Cobalt market suffered.[20] Not only the Co is globally concentrated in mining, but it is also concentrated in refining. The global trade links of cobalt ores, concentrates, and other intermediate products is dominated by a small group of countries. In particular, China's import from DRC accounts alone for almost 40% of the total global trade value. Despite various risks may damage the stability of the Co supply chain some recent changes might mitigate some of these risks. Firstly, it is expected that improvement in extraction technologies would make the cobalt supply to respond more effectively to changes in its demand. Secondly, after the London Metal Echange, which is the world larges exchange market for a variety of metals, started training Co in the mid 2010, its annual price volatility dropped significantly and both producers and consumers will benefit from the effectiveness of this exchange market.

Finally a focus on the supplies of lithium is due. The availability of lithium has proven to be a controversial topic; contradictory results on whether supply can meet demand in the near future have been reported. Lithium is generally recovered via precipitation of lithium carbonate from the brine salt lakes, or mined from pegmatites, typically found in the mineral spodumene. The mined concentrate is leached and precipitated as lithium carbonate or hydroxide. Recent resource estimates for Li range from 33 to 60 million tonnes, and reserves are around 14 million tonnes.[21] Recent literature agrees on the fact that the challenges are not whether there is enough Lithium, but whether its production can ramp up quickly enough. The recent and rapid consumption of LIBs (+73% from 2010 to 2014) is coupled with only a 28% growth in production, leading to a consumption-production imbalance.[22] Nevertheless, based on the supply diversity and the significant attention this topic has received, many firms are positioned to respond rapidly to disruptions, and increased recycling could mitigate issues around Li supply. In

conclusion, whether LIBs alone can satisfy the rising demand for HEVs, EV and small and/or mid-to-large-format energy storage applications remains unclear. To mitigate these issues, recent research has focused on alternative energy storage systems.

2.4 Sodium-ion batteries

Alkali metals such as sodium, and more recently potassium, are considered appealing alternative power sources due to the wider availability of their resources and similar chemistry to that of LIBs. At the dawn of LIBs, sodium, the fourth most abundant element on earth, was also taken into consideration, and in the 1970s some works describing the sodium ion transport in inorganic materials lattice were published. In the late 1980s, prior to the commercialization of LIBs, a few USA and Japanese companies developed a full SIB where a sodium-lead alloy composite and a P2-Na_xCoO_2 were the anode and the cathode respectively.[23] However, despite a remarkable cyclability (over 300 cycles) the lower average discharge voltage of 3,0V compared to 3,7V of the Carbon//$LiCoO_2$ did not attract much attention. After the commercialization of LIBs the research on sodium insertion materials almost disappeared (excluding the research on high-temperature sodium-sulphur), and it was not until the recent years that the number of publications dealing with sodium ion batteries skyrocket.[4] In particular, the renewed interest in SIB followed the Jean Marie Tarascon's article titled *'Is lithium the new gold?'*, which for the first time raised the concern of a possible Li shortage in a few decades.The research on SIBs is far from being just an academic exercise as proved by the vast number of patents filed regarding new active materials, structures and cell architectures. As a matter of fact, in 2015, after the launch in 2012 of the sodium-ion research task force (CEA, *Commissariat à l'énergie atomique et aux énergies alternatives*; CNRS, *Centre national de la recherche scientifique*; *College de France*) the company TIAMAT developed the first Na-ion battery in the industry standard 18650, claiming an improved lifespan and higher charge and discharge current densities compared to standard lithium ion batteries. Nevertheless, to evaluate in practice the savings in adopting sodium is everything but an easy task, and only recently this problem was examined and modeled in detail.[25,26] If on one hand SIBs material precursors are cheaper compared to their LIBs analogues, and may lead to a reduced manufacturing cost, on the other hand the lower energy densities of SIBs can invalidate that advantage and ultimately lead to an increased energy cost ($USD{\cdot}kWh^{-1}$). The materials cost

[41] Scopus data: htttps//www.scopus.com

reduction for the cathode (that accounts for 36% of the the manufacturing of LIB, as shown in Figure 2.7) could be achieved only if expensive elements such as Co and Ni are replaced with cheaper and more abundant ones. At the same time, thanks to the fact that sodium does not alloy with Al, a considerable cost reduction could come from replacing copper with aluminum as the anode current collector. Overall, the cost analysis reported in literature shows that replacing lithium with sodium does not directly nor necessarily reduce the cost per kWh of a battery. However, the aggravation of the identified raw materials issues for LIBs, such as shortages in the supplies of Li and Co, can make lithium- and cobalt-free systems, such as SIBs, attractive and cost-competitive alternatives.

2.5 Potassium-ion batteries

Despite the significant focus on SIBs, non-aqueous potassium-ion batteries remained largely unexplored for long time and have attracted considerable attention only in the last 5 years. Despite the first demonstration of a potassiated graphite dates back to the 1960s,[27] graphite's failure for SIBs discouraged the study of carbonaceous materials for potassium ion batteries (KIBs.) It was not until 2015 that a series of publications reported the reversible potassium intercalation into graphitic materials that leads to the KC_8 phase.[28,29,30] The high capacity and the low working potential of graphite paved the way to high voltage and high energy non-aqueous potassium batteries. From that moment on we witnessed an astounding increase in publications regarding KIBs, and growing research efforts have been dedicated to understanding their electrochemistry and improving their performances. Indeed, new electrode materials and new electrode/battery configurations have been proposed recently. Although KIBs are still far from being fully understood, analyzed and eventually commercialized, the impressive performances already proven in literature represent a very promising starting point. A more in depth analysis of the advantages and disadvantages that potassium has in comparison to sodium and lithium are be proposed in the next chapter.

Bibliography

[1] M. C. Lott and S.-I. Kim, *Technology Roadmap, Energy Storage*. 2014.

[2] S. Trasatti, "1799–1999: Alessandro Volta's 'Electric Pile,'" *J. Electroanal. Chem.*, vol. 460, no. 1–2, pp. 1–4, 1999.

[3] S. Trasatti, "1786–1986: Bicentennial of Luigi Galvani's most famous experiments," *J. Electroanal. Chem. Interfacial Electrochem.*, vol. 197, no. 1–2, pp. 1–4, 1986.

[4] G.-L. Leclanché, "No Title," *Compt Rend*, vol. 83, no. 54, 1866.

[5] S. Ruben, "(1947)," in *Proc Electrochem Soc Meeting, Chicago*, 1947.

[6] B. Scrosati, "History of lithium batteries," *J. Solid State Electrochem.*, vol. 15, no. 7–8, pp. 1623–1630, 2011.

[7] N. S. Ikeda H, Narukawa S, "(1980)," *Proc. 29th Power Sources Con, Electrochem. Soc. Pennington, NJ, USA*, 1980.

[8] M. S. Whittingham, "Chemistry of intercalation compounds: Metal guests in chalcogenide hosts," in *Progress in Solid State Chemistry*, 1978, vol. 12, no. 1, pp. 41–99.

[9] P. Vashishta, J. N. Mundy, and G. K. Shenoy, "Fast ion transport in solids," in *Fast ion transport in solids-electrode and electrolytes conference*, 1979.

[10] M. Armand, J. Chabagno, and M. Duclot, "Extended abstract of The Second International Meeting on Solid Electrolytes," *Ext. Abstr. Second Int. Meet. Solid Electrolytes*, 1978.

[11] D. W. Murphy and J. N. Carides, "Low Voltage Behavior of Lithium / Metal," *J. Electrochem. Soc.*, vol. 126, no. 3, pp. 349–351, 1979.

[12] M. Lazzari and B. Scrosati, "A Cyclable Lithium Organic Electrolyte Cell Based on Two Intercalation Electrodes," *J. Electrochem. Soc.*, vol. 127, no. 3, p. 773, 1980.

[13] T. Nagaura, *Progress in Batteries and Solar Cells*, 10th ed. JEC Press Inc., IBA Inc., 1991.

[14] E. A. Olivetti, G. Ceder, G. G. Gaustad, and X. Fu, "Lithium-Ion Battery Supply Chain Considerations: Analysis of Potential Bottlenecks in Critical Metals," *Joule*, vol. 1, no. 2, pp. 229–243, 2017.

[15] A. K. Padhi, K. S. Nanjundaswamy, and J. B. Goodeoungh, "Phospho-olivines as Positive-Electrode Materials for Rechargeable Lithium Batteries," *J. Elecrochemical Soc.*, vol. 144, no. 4, pp. 1188–1194, 1997.

[16] J.-M. Tarascon, "Is lithium the new gold?," *Nat. Chem.*, vol. 2, no. 6, p. 510, Jun. 2010.

[17] D. Olson, *Graphite, in U.S. Geological Survey Minerals Information: Mineral Commodity Summaries (US Geological Survey).* 2013.

[18] A. Feytis, "The bright side of graphite. Industrial Minerals." pp. 31–39, 2010.

[19] "Cobalt supply & demand. Cobalt Facts. https://www.cobaltinstitute.org/about-cobalt. html (Cobalt Development Institute).," *2015*. .

Chapter 3

Brief theoretical background

3.1 Introduction

Galvanic cells and in particular rechargeable batteries are a complex system. If their operating principles can be discussed under a pure electrochemical point of view, their full understanding requires a multidisciplinary approach. Many other disciplines such as materials science, engineering, theoretical physical-chemistry and modeling have all contributed to the success of these energy storing devices. Far from being fully exhaustive, this chapter presents the most important electrochemical and materials science notions, and the working principles of a battery that will allow the reader to easily go through the following chapters. Starting with thermodynamics and kinetics, the most common reaction mechanisms of a modern secondary battery will be reviewed. A theoretical background be provided to the reader, together with the quantities that help defining the performance of a battery.

3.2 General Thermodynamics

The basic working principle of an electrochemical energy storage device involves the conversion of chemical energy into electrical energy. To understand this process, it is important to consider driving forces and the reaction mechanisms that can occur in an electrochemical cell.
Lets first consider a simple chemical reaction between two metals, A and B, which in contact between each other, react to form the product, C:

$$A + B \rightleftharpoons C \tag{3.1}$$

The driving force of this reaction is the difference between the Gibbs free energy of the product (C) and the Gibbs free energy of the reactants:

$$\Delta G_r = \sum \Delta G_f(products) - \sum \Delta G_f(reactants) \tag{3.2}$$

In a full solid state reaction the two solids (A and B) are placed in direct contact and the product (C) begins to form at the interface between them. As the reaction proceeds and C is formed, at least one of the reactants must diffuse through the product and reach the other reactant on the other side. The reactants will be therefore consumed and substituted by C that will grow symmetrically or asymmetrically towards A and B depending on the stoichiometry of the reaction and diffusivity of A and B through C. If the reactants are not in direct contact, the reaction can still take place electrochemically as long as some conditions are satisfied:

- an electronic insulating, ionic conductor (generally referred as *electrolyte*) must be placed between A and B;
- an external electron conducting circuit (that can include a load) must connect A and B.

The first item must contain either A or B ions and guarantees the ionic conductivity, while the latter guarantees the electronic continuity. Driven by thermodynamics, a net flux of charged species flows from A to B or vice versa. For example, in the electrochemical *discharge* depicted in Figure 3.1 A^+ ions move through the electrolyte, and the negatively charged species, namely electrons (e^-), flow through the external circuit and C forms at the interface between B and the electrolyte. Generally speaking the overall reaction can be split into two semi-reactions:

$$Red \rightleftharpoons Ox + ze^- \tag{3.3}$$

On the other side of the electrolyte the corresponding half-reaction is:

$$Ox + ze^- \rightleftharpoons Red \tag{3.4}$$

Where ze^- is the number of electrons exchanged per mole of reduced or oxidized species. Equation 3.3 depicts the oxidation reaction whereas 3.4 is the reduction reaction. Important consequences follow from the overall electron-neutrality of the process, as the process will stop if:

- the ion conduction in the electrolyte no longer occurs
- the external electric circuit is opened

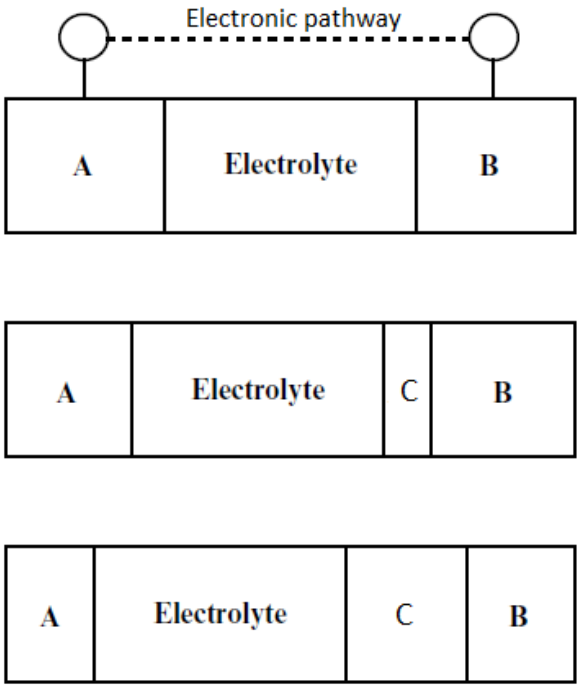

Figure 3.1: Simple depiction of the miscrostructure time evolution during the electrochemical reaction of A and B to form AB. It is assumed that A^+ are the predominant ionic species in the electrolyte. To simplify, the external circuit is shown only in the top image

- the chemical equilibrium is met

It can be demonstrated that the ΔG_r is equal to the non-expansion work done by a system under standard pressure and temperature, and therefore we can write:

$$\Delta G_r = -zFE \tag{3.5}$$

where E is the potential at the equilibrium, when no current is flowing (emf). Conventionally, half-reactions are always reported in the reduction sense, and the potential acquires a positive or negative sign depending on the spontaneity of the reaction. Given a galvanic chain, when standard conditions apply, the emf can be calculated from the standard potential,[1] formally expressed as standard reduction potentials reported against the standard hydrogen electrode (SHE).

3.3 Nernst Equation and variation of the voltage as batteries are discharged

When the circuit is open and no current flowing, and when the conditions vary from the standard ones the potential can change, as expressed in the Nernst Equation.
Given a general half reduction reaction:

$$aOx + ze^- \rightarrow bRed \tag{3.6}$$

The Gibbs free energy of the reaction is:

$$\delta G = \delta G^0 + RTln[\frac{a^b_{Red}}{a^a_{Ox}}] \tag{3.7}$$

From the relation 3.5 we can therefore write:

$$\delta G^0 + RTln[\frac{a^b_{Red}}{a^a_{Ox}}] = -zFE \tag{3.8}$$

rearranging:

$$E = -\frac{\delta G^0}{zF} - \frac{RT}{zF} * ln[\frac{a^b_{Red}}{a^a_{Ox}} \tag{3.9}$$

$\frac{\delta G^0}{zF}$ is constant and represent the standard reduction potential of a given half reduction reaction (E^0). We can finally write:

$$E = E^0 + \frac{RT}{zF} ln[\frac{a^a_{Ox}}{a^b_{Red}}] \tag{3.10}$$

This relation is the so-called $Nerst$ equation and represents be a useful tool to define the cell potential of a general electrochemical cell out of standard conditions when no net current is flowing. Considering a generic redox reaction in an electrochemical cell, the cell potential (E_{cell}) is:

$$E_{cell} = E^0_c - E^0_a + \frac{RT}{zF} ln \frac{1}{Q} \tag{3.11}$$

where E^0_c and E^0_a are the standard reduction potential of the specie that is reduced and the specie that is oxidized respectively and Q is the reaction quotient. If E_{cell} is > 0 the electrochemical cell is a galvanic cell, and if E_{cell} is > 0 it is called an electrolytic cell.
For example, lets consider a lead-acid battery. These kind of batteries are widely used to provide the starting power in virtually every car and marine

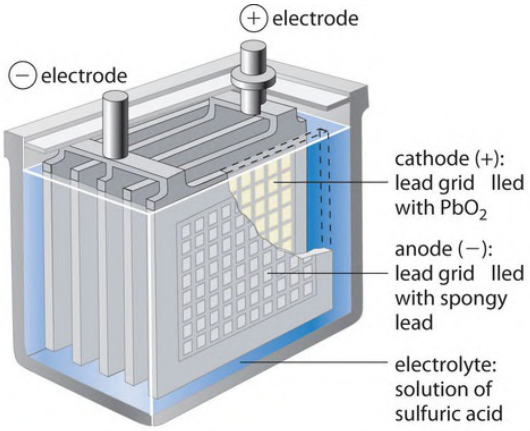

Figure 3.2: A Lead–Acid cell.

engine on the market, and typically consist of multiple cells connected in series. The total voltage of the battery pack is the efm of each cell times the number of cells (Figure 3.2). The anode active material in each cell of a rechargeable battery is a spongy lead metal, and the cathode is powdered lead dioxide (PbO_2). The electrolyte is generally an aqueous solution of sulfuric acid. The positive plate half reaction during discharge is:

$$PbO_2(s) + HSO_4^-(aq) + 3H^+(aq) + 2e^- \rightarrow PbSO_4(s) + 2H_2O(l) \quad (3.12)$$

that has an E^o equal to 1.685V. The associated negative semi-reaction during discharge is:

$$Pb(s) + HSO_4^-(aq) \rightarrow PbSO_4(s) + H^+(aq) + 2e^- \quad (3.13)$$

that has an $E^o = -0.356V$. If the activity of all the electrochemically active species are equal to 1, the overall cell efm is therefore:

$$E^o_{cell} = E_{cathode} - E_{anode} = 1.685V + 0.356V = 2.041V \quad (3.14)$$

It is useful to consider the relation between the cell voltage and the state of charge under equilibrium or near-equilibrium conditions. As shown in the voltage-state of charge profiles for different materials, there are significant differences in their behavior, indicated by the different shapes of their curves. To understand how the theoretical open circuit voltage varies with the state of charge, the so-called *Gibbs Phase Rule* can be considered:

$$F = C - P + 2 \quad (3.15)$$

where C is the number of components (i.e. elements) present, P the number of phases present in the material at a given state of charge, and F is the number of degrees of freedom. The latter therefore indicates the number of intensive thermodynamic parameters that must be specified to define a system and all its associated properties, which in the case of an electrochemical cell are generally temperature, pressure and chemical potential or chemical composition of each of the phase presents. In the case of lithium metal, we have a single element with only one type of atom:

- P is equal to 1
- C is also equal to 1

from equation 3.15, F is equal to to 2. This means that if temperature and pressure are specified, no degrees of freedom are left and therefore all the intensive properties of the system are defined, i.e. have fixed values. Regardless of the amount of lithium present (and the state of charge of the cell), at constant temperature and pressure the potential of the lithium metal negative electrode is constant. The simple examples discussed so far assume that the thermodynamic data are already known. On the other hand, it is possible to use the elctrochemical data to obtain thermodynamic information. A useful tool for this purpose is the Coulometric Titration Technique, the full description of this technique is however beyond the scope of this work and can be found elsewhere.[35] In any case, it is important to notice that the composition dependence of the electrochemical potential, as well as the capacity of binary, ternary or more complex systems are directly related to the thermodynamic properties and compositional ranges of the phases in the respective phase diagram. Their behavior can be understood also under dynamic conditions taking into account deviations from the equilibrium conditions. However, metastable phases may be present that may considerably differ from the absolute-stable phases.

3.4 Kinetics of electrode reactions

In practical applications, the electrode potential is never exactly equal to the theoretical one. Obstacles (or resistances) to the free-flow of ions and electrons always exist. The difference between the equilibrium potential of the electrode expressed by the Nernst relation (E^o) and the potential of the same electrode as a result of external current flowing ($E(i)$) is called overpotential (η)

$$\eta = E(i) - E^o \tag{3.16}$$

Overpotential values can originate from mainly four processes that concur in defining the operational output voltage of the cell:

- mobility of the ions in the electrolyte (Ohmic Drop)
- mobility of the ions and the electrons
- charge transfer at the elecrode/electrolyte interface (CT)
- electronic leakage through the electrolyte

These phenomena concur in defining the final voltage. To better understand the phenomena behind the overpotential, lets focus our attention on a generic electrochemical reduction/oxidation of one electroactive specie (A) in solution at one of the electrodes. We can break down the whole process as:

$$A_{Bulk} \xrightarrow{MT} A_{OHP} \xrightarrow{Chem.} A_{Ads} \xrightarrow{CT} A^{z+/-} \xrightarrow{Chem} A^{z+/-}_{OHP} \xrightarrow{MT} A^{z+/-}_{Bulk} \quad (3.17)$$

The electroactive specie in solution A_{Bulk} is firstly transported (MT) to the active site and depends on diffusion (under a concentration gradient) and migration (under an electrostatic potential gradient). The active site, where the charge transfer (CT) occurs, can be the Outer Helmolz Plane or a specific adsorption site (Ads) closer to the working electrode. In the latter case, the transfer requires extra energy (Chem.). According to the reaction, the path can be easier (just one MT and one CT, as in the Ag^+ deposition on Ag), or can have all the steps (as in the case of oxygen reduction). Every single step of the reaction is characterized by an activation energy together with an initial, intermediate and final state. Every single step of the reaction, can therefore represent the rate determining step and can influence the kinetics of the whole process. The charge transfer's (CT) rate and the mass transport (MT) are directly linked with the electronic current at the interface and the ionic current in the solution, respectively.
Experimentally, most of the rate constants k of solution-phase reactions vary with temperature T in a common fashion: nearly always, lnk is linear with 1/T. This behavior has been firstly recognized by Arrhenius who proposed a mathematical expression, as an empirical generalization of reality, that is found in many distinct cases:

$$k = Ae^{-\frac{E_A}{RT}} \quad (3.18)$$

where E_A, known as activation energy, has the units of a Energy and expresses the height of the maximum energy barrier, that the has to be overcome along the reaction coordinate for the reaction to proceed, and A is

known as the frequency factor. Many events that occur in a cell can follow an Arrhenius-type mechanism. The Charge transfer for example can manifest a linearity with 1/T.
A fundamental relation in electrochemical kinetics is the Butler-Volmer equation which, when the electrode reaction is controlled by the charge transfer, in a one-step, one-electron process, can be written as:

$$i = i_0 A[e^{\beta_a z F \eta / RT} - e^{e^{\beta_c z F \eta / RT}}] \tag{3.19}$$

Where β_a and β_c are the oxidation and reduction symmetry factor, and i_0 is the exchange current, and A is the electrochemically active surface area. This expression describes how the electrical current depends on the potential, and correlates the rate at which the electron transfer is taking place, to the overpotential. There are two limiting cases:

- the low overpotential region, where at $E \approx E_{eq}$, the dependence of current on polarization becomes linear:

$$i = i_0 z F \eta / RT \tag{3.20}$$

- the high overpotential region, the Butler-Volmer reduces to the Tafel equation (a and b are constants at a given temperature):

$$\eta = a_c - b_c log i \tag{3.21}$$

  for the cathodic region when $E \ll E_{eq}$

$$\eta = a - b_a log i \tag{3.22}$$

  for the anodic region when $E \gg E_{eq}$

In addition, the Butler Volmer relation, can be generalized for mass transfer controlled and/or multiple steps reactions.

3.5 Electrolytes for alkali metal ion batteries

The electrolyte is responsible for containing and shuttling the charge carrier ($H^+, Li^+, Na^+, K^+, Mg^{2+}$) between the electrodes. This is generally made possible by dissolving a salt, the source of the ions, in one or more solvents. In room temperature alkali metal ion rechargeable batteries, stringent requirements exist for the electrolytes, as they should have:

1. the widest possible electrochemical stability window (ESW);

2. a high ionic conductivity (in the range of mS/cm), high transference number of the alkali ion (as close as possible to 1) and a low viscosity;

3. a low cost. In particular the salts, as they are generally more expensive compared to the solvents;

4. a low toxicity, stability over time, should be safe and non flammable;

As the stored energy is a function of the average voltage and the capacity (see section 3.6), both of the figures assume a fundamental importance. Thermodynamic stability requires locating the electrode electrochemical potentials μ_A and μ_B within the stability window of the electrolyte, that is determined by the Lowest Unoccupied Molecular Orbital (LUMO) and the Highest Occupied Molecular Orbital (HOMO) of the electrolyte components (Figure 3.3). An anode with an electrochemical potential μ_a above the LUMO will reduce the electrolyte unless a passivation layer creates a barrier to the electron transfer; whereas a cathode with a μ_c below the HOMO will oxidize the electrolyte unless a passivation layer blocks the electron transfer from the electrolyte HOMO to the cathode. Indeed, a passivating solid/electrolyte-interface (SEI) layer at the electrode/electrolyte boundary can provide a kinetic stability. A high conductivity of the electrolyte is required to reduce the resistance to the flow of ions, i.e. to reduce the ohmic drop. Transport numbers help define the contribute to electrolyte conductivity of a solvated ion. With the transference number of a charged specie, defined as the proportion of the total current carried by that ion:

$$t_i = \frac{I_i}{I_t} \tag{3.23}$$

where I_i is the current carried by the ion i, and I_t is the total current carried by all the ions in the electrolyte.

3.5.1 Aqueous electrolytes

So far, the cheapest electrolytes to have been utilized are aqueous based. They are generally either basic or acidic water solutions. Intrinsic limitations to the maximum theoretical voltage of the cell are imposed by water splitting:

$$2H^+ + 2e^- \rightleftharpoons H_2 \; E^o = 0.00V vs NHE \tag{3.24}$$

$$2H_2O \rightleftharpoons O_2 + 4H^+ + 4e^- \; E^o = 1,23V vs NHE \tag{3.25}$$

The standard potentials of the above reactions are pH-sensitive, and therefore depending on the electrolyte formulation, a different electrochemical potential window becomes available (Figure 3.4).

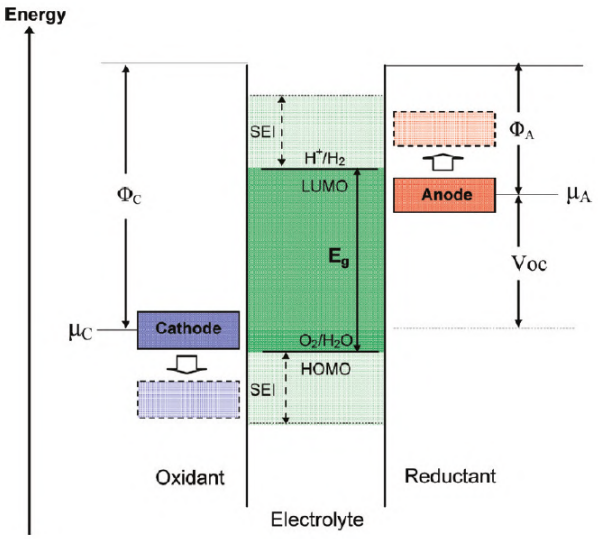

Figure 3.3: Depiction of the energy diagram in an aqueous based electrolyte. I_a and I_c are respectively the anode and the cathode work functions. E_g is the thermodynamic stability window of the electrolyte. If $\mu_A > LUMO$ or $\mu_B < HOMO$ decomposition of the electrolyte will occur, and the SEI may form.[2]

3.5.2 Supercocentrated aqueous electrolytes

Theoretically no more than 1.23V would be achievable in aqueous based electrolytes, nonetheless highly concentrated (superconcentrated) aqueous solutions are emerging as a new class of electrolytes with unusual functionalities beneficial for both advanced batteries and super-capacitors.[3,4,5] This concept was first introduced for organic electrolytes and subsequently extended to aqueous electrolytes in 2015. In their manuscript, Suo et al. mitigated the reductive decomposition of water in a 21mol·kg^{-1} LiTFSI aqueous solution and realized a 2V $Mo_6S_8|LiMn_2O_4$ full cell, that was successfully cycled for over 1000 times.[6]. Yamada el al. designed a hydrate melt $(Li(TFSI)_{0.7}(N(SO_2C_2F_2)_2)_{0.3} * 2H_2O)$, further expanding the ESW.[3] A further development was made by Yang et al., who pre-treated Lithium and Graphite with an artificial SEI and realized in this way a 4V aqueous battery.[7] Most recently, Jiang et al. proposed a Fe-substituted-Mn-hexacyanoferrate prussian blue cathode that was cycled in 22M potassium triflate superconcentrated aqueous solution and achieved a 70% capacity retention at 100C and a lifespan of over 10000 cycles.[8] Scientifically, the basis of concentrated electrolytes introduces new questions, some of which still unanswered, because of the large deviation from the dilute counterparts in

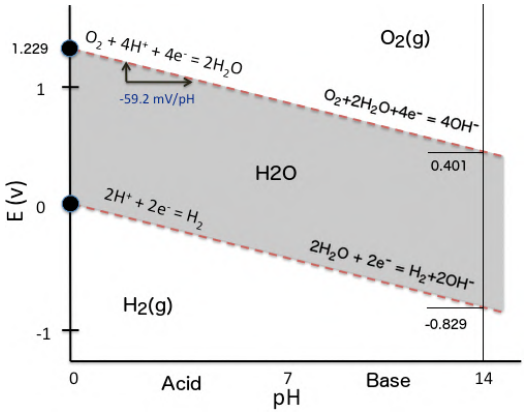

Figure 3.4: The *Pourbaix Diagram* for water. The vertical scale is the electrode potential versus SHE and the horizontal axis is the pH of the electrolyte. Neglecting the overpotential, above the top dashed line oxygen will bubble off the electrode, whereas below the bottom line, hydrogen will be generated. Source Wikipedia

terms of the solution structure, electronic structure, transport mechanism and SEI formation mechanism. When the salt outnumbers the solvent in both number of moles and volume, the definition water-in-salt electrolyte (WISe) applies. The extremely high concentration leads to a different solvation shell of the alkali metal ion, stronger inter-ionic interactions relative to solvent-ion interactions, reduction of the water activity and modifications of the electrode-electrolyte interphasial chemistry, finally resulting in a manipulation of the electrochemical behavior of the electrolyte.[5] In most of the electrolytes, the LUMO is dominated by solvent molecules, and therefore they are the predominantly reduced species that contribute to the SEI formation. At higher concentrations the solvation differs and the strong alkali metal-ion/ion interaction results in a shift of the anion orbital levels; therefore the LUMO starts to become dominated by the anions. These features have been reported primary for the LiTFSI/Acetonytrile superconcentrated electrolytes,[9] but have also been reported for the aqueous ones.[6,3] Despite the high-ion concentration, the room temperature conductivity of the electrolyte remains in the range of tens of mS/cm, comparable, if not higher, to the conductivity of the commercial Li-ion battery electrolytes. The transport mechanism is therefore another important feature that needs to be considered. In highly concentrated electrolytes the motion of ions follows to the Stokes-Einstein Law, but when aggregates and contact ion pairs are present, as in the case of WISe, the transport mechanism differs. A motion correlated with the surroundings has been proposed together with a H_2O rich 3D per-

colating network wherein fast trasport of the alkali metal-ion is possible.[10] Nevertheless, the generality of the proposed transport mechanism and the interphase structures that lead to the SEI formation are still open questions that need to be fully addressed.

3.5.3 Non-aqueous electrolytes

Most of the current research efforts in the investigation of potassium and sodium ion batteries employs aprotic non-aqueous electrolytes. The formulation of the electrolyte generally employs carbonates, ethers, and more recently room-temperature ionic liquids.

3.5.4 Ionic Liquids

Ionic liquids (ILs) are defined as molten salts having melting point lower than 100°C. Following water and organic solvents ILs are now recognized as a third group of solvents (and electrolytes) that have unique properties such as low vapor pressure, high thermal stability and high ionic conductivity. These properties make them particularly appealing for energy storage applications. However, it should be pointed out that the mentioned properties are not necessarily afforded by all ionic liquids as their properties are affected by the Lewis acidity/basicity of the cation-anion, their radial interactions, and their Van der Waals interactions.[11]
ILs for Li-Na-K ion battery electrolytes are generally categorized into 3 types:

- Li-Na-K salts having melting points lower than 100°C;
- Li-Na-K salts dissolved in room temperature ILs;
- Solvent-ILs complex $[A(solvent)_x]^+$ (A: K,Li,Na).

Although it is difficult to predict the melting temperatures of alkali ion salts because of the complexity of the problem, it can be noticed that the melting point of conventional Li/Na/K are typically above 100°C due to the strong electrostatic attractions between the cation and the anion. Nonetheless, if we consider that Li^+ is a strong Lewis acid, according to the HSAB theory, weaker Lewis-basic anions will interact weakly with the alkali metal ion. Moreover, coordinating ether ligands can help dissociating the cation from the central atom of the anions. Similar considerations apply for Na and K. For example, alkali metal oligoether carboxylate maintains a liquid state at ambient temperature.[12] Although the melting points of these salts are low, the ionic conductivity of the molten salts are as low as $10^{-5} - 10^{-4}$ S cm^{-1}

at room temperature, because of their very high viscosity and long lifetime ion pairs.
The most commonly used ionic liquids are composed of alkali metal salts dissolved into room temperature Ionic Liquids. In other words, ILs are used as electrolyte solvents for Li-Na-K salts. The physicochemical properties of this binary mixtures are significantly affected by the structures of cations and anions of the IL. The reductive stability of the ILs is strongly affected by the chemical nature of the cations. Apiphatic Quaternary Ammonium (AQA) cations, including pyrrolidinium ($[C_nmpyr]^+$) and pyperidinium and Aliphatic Quaternary Phosphonium (AQP) cations are known to have good reductive stability.[13,14] The transport properties of such binary mixtures are significantly affected by the organic cations as, in general, increasing their ionic radius increases viscosity and decreases conductivity.[15] Functional groups, conformational freedom, and different interactions with the anion can also influence viscosity and conductivity.[16]
The anodic stability of the ILs is determined by the anion oxidation event. Fluorinated anions are generally preferred, owing to their good anodic stability. Moreover, the Lewis basicity of this type of anions is rather weak, resulting in weak interactions with the organic cations.[17] The anion also influences the ionic mobility of the alkali-metal cation. Indeed, when the salt is dissolved in the IL, the alkali-metal cation (A^+) is solvated by the by IL anions (X^-) resulting in the formation of complexes $[A(X)_x]^{(x-1)-}$. In the case of lithium for example, due to the complex formation, the Li^+ coordination shell radius is bigger compared to the one in common organic electrolytes (ex. Propylene Carbonate), therefore increasing the concentration of Li^+ in solution, the viscosity increases and the ionic conductivity decreases. For the same reason the transference number of Li^+ in an IL is much smaller than the one in molecular solvents.[18,19] A correlation exists between the anion size and the viscosity of the ILs.[16] Not only the anion size, but also its structure is significantly affect the viscosity.[11] Among the ILs with common cation ($[DEME]^+$), the one with the $[FSI]^-$ anionis has the lowest viscosity, enhancing the mobility of the alkali-metal cation.[16] Due to the cation-anion complex formation in the ILs, the anion-alkali metal cation interaction also greatly affects the charge transfer process at the electrode/electrolyte interface.[20,21 For example Matsumoto et al. reported different Charge Transfer resistances (R_{ct}) depending on the anions species of the ILs, on both Li metal and $LiCoO_2$ active materials.[16] A representative example that can help understanding how much the IL anion can influence the electrochemical reaction, is graphite. This well known negative electroactive material for Li-ion batteries can reversibly intercalate Li^+ during

the reduction of graphite, according to the following reaction:

$$6C + Li^+ + e^- \rightarrow LiC_6 \tag{3.26}$$

When an IL based lithium electrolyte is employed it is known that instead of Li^+ the organic cation is inserted in the graphite, this results into the destruction of the layered structure of graphite,[22] Nevertheless, when an [FSI]-based IL is used the intercalation of the organic cation is suppressed and reversible intercalation of Li^+ occurs.[23] It has been proposed that a small amount of $[FSI^-]$ is decomposed during the first lithiation of the graphite, and the decomposition products form a stable passivation layer that prevents the organic cation intercalation.[24] However, the passivation mechanism is still not fully understood and different explanations have been proposed.[25] As will be explained later in the dissertation, the intercalation of potassium into graphite in an ILs based electrolyte has been reported to be affected by the same problem.[26]

3.6 Practical parameters for batteries

Different properties and descriptors concur in defining a battery. According to the final use of a secondary battery, some properties might be more relevant than others and will finally result in a different choice for a specific technology. It is therefore mandatory for the reader to fully understand the meaning of the parameters described in this section as they will be often referred through the entire dissertation.

3.6.1 Energy, Power and Capacity

The most common and widely referred parameter that define the alkali metal-ion uptake theoretically (or practically) achievable by an electrochemically active material is the *Specific Capacity* (measured in $mAh \cdot g^{-1}$). This represents the total charge stored normalized over the mass of active material, and is defined as:

$$C = \frac{\int_{t_0}^{t_f} i(t)dt}{g_{AM}} \tag{3.27}$$

More general and comprehensive parameters are the $Specific\ Energy$ ($Wh \cdot kg^{-1}$) and $Specific\ Power$ ($W \cdot kg^{-}1$). If normalized per volume instead of weight they are referred as *Energy Density* or *Power Density*. The Specific Energy is defined as follows:

$$SpecificEnergy = \frac{\int EdQ}{kg} \tag{3.28}$$

The Specific Power at a time t is:

$$SpecificPower_t = \frac{i_t * E_t}{kg} \tag{3.29}$$

From the provided definitions comes the concept of energy quality. As in a hot source the temperature defines the quality of that energy, in a battery, energy, power and electrochemical potential are tied-up together and the potential can help define a sort of energy quality rankings:

- 3.5V-5.5V High Quality Energy
- 1.5V-3.5V Medium Quality Energy
- 0V-1.5V Low Quality Energy

High voltage is required for a number of applications. For example, in the all-electric and hybrid-vehicles, the manufacturers typically need to operate at 200V. Therefore, it is desirable that individual cells have the highest possible voltage, as fewer cells are necessary.
Another useful parameter that defines the performance of a battery is the maximum theoretical specific energy (MTSE), that takes into account the specific reaction occurring at the electrodes. Given the following reaction:

$$xA + R \rightleftharpoons A_xR \tag{3.30}$$

where x is the number of moles of A that reacts per mole of R. If W_t is the sum of the molecular weight of the reactants, E is the electrochemical potential and F is the Faraday constant, we can write:

$$MTSE = \frac{xEF}{Wt} \tag{3.31}$$

3.6.2 C-rate and Coulombic Efficiency

A common term that specifies the speed at which the cell is charged or discharged respective of its theoretic specific capacity is the $C-Rate$. Used as an alternative to current density, a $nC-Rate$ of charge/discharge corresponds to a current high enough to fully charge or discharge the cell in n hours. For example, a C-Rate of 1C , for a 2 Ah battery, would correspond to 2A applied for 1h of charge/discharge. Conversely, for the same battery, $C/10$ corresponds to 0.2A applied for 10hours.
A second, and very useful tool used to describe the cycling behavior of a cell

is the Coulombic Efficiency (CE), defined per each cycle of Charge/Discharge and calculated as:

$$CE = \frac{Q_{discharge}}{Q_{Charge}} * 100 \tag{3.32}$$

Where $Q_{discharge}$ and Q_{Charge}, generally referred as Discharge and Charge Capacity respectively, are calculated by integrating the the current over time $\int_{t_i}^{t_f} idt$. The CE is always ≤ 100 and addresses the irreversible capacity per each cycle. As it will be further illustrated parasitic reactions and mechanisms of autodischarge can lower the Coulombic efficiency.

3.7 Agreement on the conventions

When talking about electrochemical processes, confusion may arise due to a lack of agreement on the technical terms. Following the IUPAC convention, in this dissertation a positive sign will be assigned to an anodic current, conversely a negative sign will be assigned to a cathodic current.
In a full cell the term *charge* will refer to the migration of the alkali-metal ion from the cathode (positive electrode) to the anode (negative electrode), whereas *discharge* will address the opposite process. Alternatively, the attention will be specifically directed to the anode or cathode material separately. These are commonly studied in half-cells with the alkali metal acting both as reference electrode (RE) and counter electrode (CE). A three electrode setup can also be employed where the CE and RE are separated. In these setups, following the nomenclature from the full cell, when an anodic material is being investigated, the sodium uptake will be referred as the charging phase and will be associated to a negative current. The discharge phase will coincide with the depletion of the alkali-metal cation, and will be coupled to a positive current. The nomenclature will be the opposite if a cathode material is the object of the analysis.

3.8 Electroactive materials for alkali metal rechargeable batteries

This section analyzes the theoretical principles and reaction mechanisms of the most important classes of active materials for aprotic SIBs and KIBs. A list of the compounds and elements belonging to these classes will be provided in the next chapters.

3.8.1 Elemental alkali metal anodes

It was from the early stage of lithium ion batteries that attempts to use the electrochemical reduction-oxidation of the alkali metal in secondary cells were made. The occurring reaction is:

$$M^+ + 1e^- \rightleftharpoons M \tag{3.33}$$

where M represent the metallic alkali metal. Impressive energy densities can be achieved employing the elemental alkali metal anodes thanks to the:

1. extremely negative standard potential reduction of the alkali metal (-3.04V for lithium, -2.71V for sodium, -2.93V for potassium)

2. modest atomic weight of the alkali metal

Table 3.1 compares these and other important parameters for lithium, sodium and potassium.

	Lithium	Sodium	Potassium
E^o_{Red} (V vs SHE) at 25^oC	-3.04	-2.71	-2.93
Atomic Weight ($g{\cdot}mol^{-1}$)	6.94	22.99	39.10
Density ($g\ {\cdot}cm^3$ (RT)	0.534	0.968	0.862
Theoretical Capacity ($mAh{\cdot}g^-1$	3862	1166	685,46
Melting Point (^oK)	453,69	370,87	336,53
Cost of Carbonate (USD ton$^-$1)	6500	200	1000
Cost of industrial grade metal (USD ton$^-$1)	100'000	3000	13'000

Table 3.1: Relevant physical, chemical and other properties of Lithium, Sodium, and Potassium.

Lithium metal has been considered for long time the *holy grail* for LIBs. However, as mentioned in the previous chapter, with the use of elemental alkali metal anodes, several problems arise that have so far hindered the commercialization of the devices that use these types of anodes. The most commonly cited issues are the relatively infinite volume expansion during cycling, the uneven plating and stripping, and the high reactivity of the alkali metal leading to safety concerns. The most puzzling issue is related to the plating process, where maintaining the starting electrode geometry and structure at the microscopic scale is desired. Unfortunately, the intrinsic instability of a flat surface on the microscopic scale during eletroplating, connected to the formation of a positive gradient of the element's chemical

potential in the electrolyte solution immediately adjacent to the depletion region, makes the growth of any even small protuberance on metallic lithium surface favorable. This event repeated during several cycles leads to dendrite growth and branching that can contact the cathode, resulting in the evolution of dead weight, cell failure, internal shortcut and violent exothermic reactions. This deleterious process has been recognized as a major issue both for sodium and lithium systems, and a fundamental role seems to be played by the mechanical constraints and by the solvents employed in electrolyte solution preparation as they affect the SEI formation.
Finally, the melting point of the elemental alkali metal should also be considered. Indeed, if Lithium metal melts well above Room Temperature (RT), Sodium and Potassium melt below 100^oC, giving rise to severe safety concerns if the battery overheats.

3.8.2 Insertion Materials

As the name suggests, insertion reactions involve the insertion of a guest specie into a normally unoccupied interstitial sites in the crystal structure of a host without changing the identity (i.e. basic crystal structure or amounts of the phases in the microstructure) of the latter. Though the chemical composition of the host phase changes as the reaction occurs, little to no changes may be induced in crystalline parameters, such as crystalline planar spacing, crystalline phase and unit cell volume. The guests can be positively or negatively charged ions as well as neutral species, and if the host has a layered-type crystal structure (such as graphite) the reaction is generally called intercalation. Reactions in which the composition of an existing phase is changed by the incorporation of guest species can also be thought of as the solution of the guest into the host material. Such processes are also sometimes referred to as solid solution reactions.
If charged ions, such as lithium, sodium or potassium cations, are inserted into the crystal structure of the host, the addition of an electron is required to balance charges. The electron addition during the insertion of a cation, or removal if the cation is extracted, is generally supported by an electrochemically active specie in the host that can reversibly undergo a redox process. A moderate electronic conductivity of the host and sufficient mobility of the inserted ion in the host crystal structure is generally required to facilitate the incorporation of the ions. Generally, the guest does not occupy randomly distributed locations inside the host crystal structure but resides in specific (low in energy) positions inside the crystal structure, i.e. the reaction is topotactic.

3.8.3 Alloying reaction

Limits in exploitable capacity in insertion and intercalation materials resides in compounds stoichiometry and material stability in accommodating an excessively high or low number of ions, crystalline layered structures can in fact collapse after an excessive depletion of inserted ions or disrupt due to their accumulation. One, extensively studied way to achieve high capacities, up to ten times higher compared to insertion materials, involves the formation of alloys of the alkali metal with Si, P, Sn, Sb and phosphides, among others (Figure 3.5).[27,28]

Silicon for example (theoretical specific capacity of $3600 mAh \cdot g^{-}1$) is one

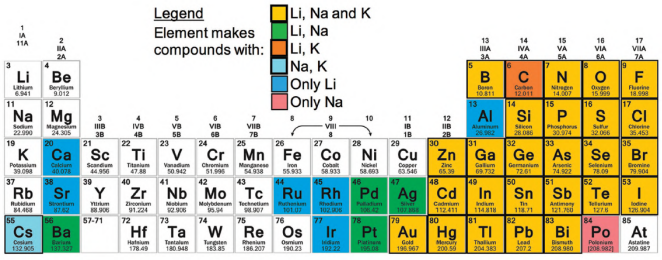

Figure 3.5: Extract of the periodic table showing the elements that alloy with Li,Na,K. From ref.[29]

of the most promising anode materials for the next generation high energy LIBs. The lithiation of silicon proceeds as follows:[27]

$$4Si + 15Li^{+} + 15e^{-} \rightleftharpoons Li_{1}5_{S}i_{4} \tag{3.34}$$

On the other hand, phosphorous has attracted considerable attention as an anode material for sodium ion batteries. The reaction can be written as:

$$P + 3Na^{+} + 3e^{-} \rightleftharpoons Na_{3}P \tag{3.35}$$

As three electrodes are involved in the full sodiation the theoretical specific capacity is $2596 mAh \cdot g^{-1}$.

Nonetheless, alloying materials suffer from severe drawbacks such as irreversible capacities and instability of the solid electrolyte interphase. The fast capacity fading of these materials is connected to the progressive fragmentation of the active material due to mechanical stresses build up during the reaction. These stresses emerge from considerable molar volume discrepancies between reagents and products, and induce cracks and faults in material particles leading to remarkable pulverization of the electrode and continuous exposure of virgin surface to electrolyte solution.

3.8.4 Conversion Materials

Thanks to the transfer of multiple electrons per mole of reactants, high capacities can also be achieved by compounds that undergo conversion with lithium, sodium or potassium. The so-called conversion reactions were studied for the first time in 70s and 80s and dealt with high temperature conversion compounds such as Fe_2O_3 and FeS_2, but recently the attention has been directed to room temperature conversion.The general reaction can be written as:

$$M_aX_b + (bc)D^+ + (bc)e^- \rightleftharpoons aM + bLi_cX \tag{3.36}$$

where M represents a transition metal, X a non-metal (such as F, O, P, N, S, H), and D is the alkali metal. A systematic approach to understand the effect of each element into conversion reactions is by progressive substitution of M and X. Indeed, a correlation exists between the ionicity of the M-X bond and measured operational potential. Fluorides exhibit the highest potential (3 V vs. Li/Li+) while oxides, sulfides and phosphides show intermediate values between 1 and 2 V vs. Li/Li^+.[30] Similarly, the transition metal plays a role in defining the cell potential as it increases with the atomic number of M for compounds with the same stoichiometry.[31]

As in the case of alloying reactions, challenges for conversion reactions come from large irreversible capacities in the first cycle and fast capacity fading due to the large molar volume variation during cycling. Another severe drawback that affects conversion reactions is the low energy efficiency due to large polarization effects. Overpotentials are intrinsic to conversion reactions and their magnitude increases with the increasing ionicity of the M-X bond. The several intermediate steps involved during the reaction and the heterogeneity of the final products have a profound effect on both the cycling stability and energy efficiency. Indeed, although the reaction mechanism is still not fully clear for many conversion reactions, an electronic conducting metal (M) embedded in a lithium, sodium or potassium chalcogenide, halide or hidride has been reported in many cases.[32,33] In the case of lithium it has been observed that only if a composite structure consisting of nanometric metallic particles embedded in a likewise Li_cX matrix is formed during the first lithiation cycle, the diffusion distances remain small enough to allow a reversible cell reaction during the subsequent cycles.

When compared to intercalation reactions, the thermodynamic treatment for conversion is straightforward and the corresponding cell potentials, capacities and energy densities can be easily calculated as long as pure bulk phases and full conversion are assumed. However, conversion reactions often involve multiple amorphous intermediate steps that can affect the electrochemical properties, leading to significant deviations from the thermodinamic proper-

ties. Nevertheless, calculating the thermodynamic properties based on pure bulk phases assuming complete conversion is useful when comparing the energies and general property differences between sodium and lithium-based conversion reactions. If for the same M_aX_b compound we subtract the generalized formula for sodium and lithium conversion reactions:

$$M_aX_b + (bc)Na \rightleftharpoons aM + bNa_cX \tag{3.37}$$

$$M_aX_b + (bc)Li \rightleftharpoons aM + bLi_cX \tag{3.38}$$

we obtain:

$$cLi + Na_x \rightleftharpoons Li_cX + Na \tag{3.39}$$

This means that the potential difference of a lithium and sodium based conversion reaction against the same M_aX_b compound solely depends on the nonmetal X. As an example, lets consider transition metal oxides and $c = 2$. The corresponding cell potential, which as mentioned equals the difference between the conversion with Li or Na, calculated from the Gibbs free energy is +0.96V. Analogues calculations can be made for different conversion reactions with X= H, F, S, Cl, Br, I and the results are reported in Figure 3.6a.[30] As previously mentioned, the volume variation that occurs during cycling is a fundamental challenge that needs to be overcome when considering conversion based materials for practical applications. Figure 3.6b reports the calculated relative volume variation for the most important classes of lithium and sodium conversion based materials. The problems associated with the volume expansion are more severe for sodium due to larger ionic radius that is between 25% and 55% larger compared to lithium, depending on the geometry. For comparison, the volume expansions of conventional intercalation materials such as $LiCoO_2$ and graphite are typically around 10%.

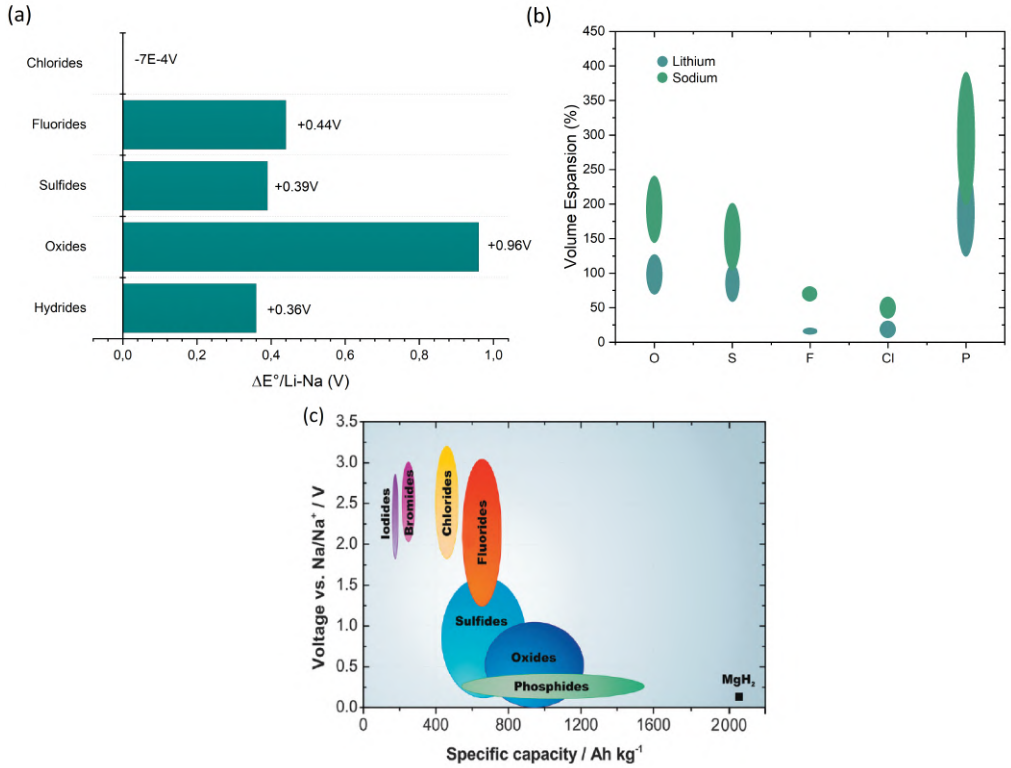

Figure 3.6: (a) Calculated differences in cell potentials between conversion reactions for the main M_aX_b with sodium or lithium, respectively. Positive values mean that replacing lithium with sodium in a conversion reaction will result in a lower cell voltage and vice versa. Calculations assume the formation of ACl, AF, A_2S, A_2O and AH as reaction products (A being Li or Na, respectively) (b) Calculated volume expansions for lithium and sodium based conversion reactions. Values are calculated as follows: volume expansion $(\%) = 100 \cdot ([V(bA_cX) + V(aM)]/V(M_aX_b)) - 100$. (c) Specific capacities and cell potentials vs. Na/Na^+ for conversion reactions of different classes of materials with sodium.[30]

However, cycling stability can be dramatically increased by electrode composition and nanostructuring for alloy based materials, which involve volume changes of a few hundred percent.[27] Similar methods apply for conversion reactions. Nanostructured active materials possess many structure-dependent advantages, which arise from high surface to volume/mass ration, small building block and robust secondary configuration. More specifically, the high surface area increases the number of active sites and reduces the diffusion path of the Na^+ ions, thus improving the reaction kinetics. A stable architecture

can help maintaining the integrity of the electrode and thus achieve good cycling stability.[34] A 150% to 250% volume variation for conversion reactions in sodium environment for oxide-based materials is calculated, whereas the volume variation is around 400% for phosphorus-base compounds. On the other hand, as depicred in Figure 3.6c, sulfides and halides have lower capacities and/or higher voltages compared to oxides. In light of this considerations, it appears straightforward how oxides would be theoretically the best choice, as anode conversion material for sodium batteries. This general principle guided us in specifically investigating transition metal oxides in sodium environment thanks to their favorable properties compared to other conversion compounds.

Bibliography

[1] G. Gritzner, *Handbook of Reference Electrodes*. 2013.

[2] J. B. Goodenough and Y. Kim, "Challenges for rechargeable Li batteries," *Chem. Mater.*, vol. 22, no. 3, pp. 587–603, 2010.

[3] Y. Yamada and A. Yamada, "Review—Superconcentrated Electrolytes for Lithium Batteries," *J. Electrochem. Soc.*, vol. 162, no. 14, pp. A2406–A2423, 2015.

[4] D. P. Leonard, Z. Wei, G. Chen, F. Du, and X. Ji, "Water-in-Salt Electrolyte for Potassium-Ion Batteries," *ACS Energy Lett.*, vol. 3, no. 2, pp. 373–374, 2018.

[5] Y. Yamada, J. Wang, S. Ko, E. Watanabe, and A. Yamada, "Advances and issues in developing salt-concentrated battery electrolytes," *Nat. Energy*, vol. 4, no. 4, pp. 269–280, 2019.

[6] L. Suo *et al.*, "'Water-in-salt'electrolyte enables high-voltage aqueous lithium-ion chemistries," *Science,* vol. 350, no. 6263 pp. 938-943, 2015.

[7] C. Yang *et al.*, "4.0 V Aqueous Li-Ion Batteries," *Joule*, vol. 1, no. 1, pp. 122–132, 2017.

[8] L. Jiang *et al.*, "Building aqueous K-ion batteries for energy storage," *Nat. Energy*, vol. 4, no. 6, pp. 495–503, 2019.

[9] K. Xu, "Electrolytes and interphases in Li-ion batteries and beyond," *Chem. Rev.*, vol. 114, no. 23, pp. 11503–11618, 2014.

[10] O. Borodin *et al.*, "Liquid Structure with Nano-Heterogeneity Promotes Cationic Transport in Concentrated Electrolytes," *ACS Nano*, vol. 11, no. 10, pp. 10462–10471, 2017.

[11] M. Watanabe, M. L. Thomas, S. Zhang, K. Ueno, T. Yasuda, and K. Dokko, "Application of Ionic Liquids to Energy Storage and Conversion Materials and Devices," *Chem. Rev.*, vol. 117, no. 10, pp. 7190–7239, 2017.

[12] O. Zech *et al.*, "Alkali metal oligoether carboxylates - A new class of ionic liquids," *Chem. - A Eur. J.*, vol. 15, no. 6, pp. 1341–1345, 2009.

[13] H. Matsumoto, H. Sakaebe, and K. Tatsumi, "Preparation of room temperature ionic liquids based on aliphatic onium cations and asymmetric amide anions and their electrochemical properties as a lithium battery electrolyte," *J. Power Sources*, vol. 146, no. 1–2, pp. 45–50, 2005.

[14] D. R. MacFarlane, P. Meakin, J. Sun, N. Amini, and M. Forsyth, "Pyrrolidinium imides: A new family of molten salts and conductive plastic crystal phases," *J. Phys. Chem. B*, vol. 103, no. 20, pp. 4164–4170, 1999.

[15] H. Tokuda, K. Hayamizu, K. Ishii, M. A. B. H. Susan, and M. Watanabe, "Physicochemical properties and structures of room temperature ionic liquids. 2. variation of alkyl chain length in imidazolium cation," *J. Phys. Chem. B*, vol. 109, no. 13, pp. 6103–6110, 2005.

[16] H. Matsumoto, H. Sakaebe, and K. Tatsumi, "Li/$LiCoO_2$ Cell Performance Using Ionic Liquids Composed of N,N-Diethyl-N- methyl-N-(2-methoxyethyl)ammonium – Effect of Anionic Structure," *ECS Trans.*, vol. 16, no. 35, pp. 59–66, 2009.

Chapter 4

Electroactive Materials for Sodium Ion Batteries

4.1 Introduction

The research on sodium-ion rechargeable batteries (SIBs) has undergone a positive momentum for ten years now. As it will be presented in this chapter many of the proposed active materials are able to ensure stability and reliability even at high currents and therefore represent important milestones on the path towards commercial full-cells. Advances achieved in carbon and graphite based materials, layered and open framework structures, and sodium storing alloys, denote opportunities going beyond traditional "rocking chair" configuration. Here, are reviewed not only the electrochemical performances but also the chemical and physical working principles of the most promising electroactive materials for negative electrodes. Since the research activity on sodium ions during the doctoral work focused on only the negative side, positive electroactive materials are not be here reviewed. The reader can refer to recent extensive reviews on sodium ion batteries.[1,2]

4.2 Anodes for SIBs

Although the research on anode materials for SIBs has recently drawn the attention of the scientific community, it still represents a challenging task. Among the difficulties experienced approaching the negative side, are the operational potential of the material in a sodium environment, often to high to guarantee an appreciable energy density, poor overall stability and frequent disruption of the material throughout cycling and low Coulombic efficiencies. A widespread criterion in investigating this type of species has been

mimicking the modern research trend in Lithium-ion battery research. This approach, despite being source of extraordinary results often limited to first cycles, is short-sighted towards a possible coupling with a cathode material, in a full cell assembly. Indeed, nowadays research on cathode materials for SIBs, is limited to insertion compounds with gravimetric capacities limited to only few hundreds of $mAh \cdot g^{-1}$. Although beyond the scope of this work, capacity balance inside the cell and thicknesses of active depositions must always be considered as it will become a critical aspect for a commercial SIB. The overwhelming number of compounds proposed in the literature will be, organized into three categories, namely:

1. Intercalation and pseudo intercalation materials;
2. p-block elements (metals, alloys and phosphorous) showing reversible sodiation/de-sodiation reaction;
3. oxides that undergo conversion reaction;

4.3 Insertion anode materials

4.3.1 Carbon Based Materials

Carbonaceous materials were the most immediate and trivial answers to the need of an anode material for sodium ion batteries. Many aspects can be listed among motivations beyond this choice, such as lithium-ion batteries heritage connected to graphite, low costs, environmental friendliness and electrochemical stability. Both lithium and potassium ions can reversibly intercalate into graphite forming the LiC_6 and KC_8 stage-1 graphite intercalation compound (GiC), with reversible specific capacities of $372 mAh \cdot g^{-1}$ and $279 mAh \cdot g^{-1}$ respectively. Here, staging index refers to the number of graphene layers between two successive layers of intercalated alkali metal atoms. On the other hand, despite Na having a ionic radius (1.05 Å) in between that of Li (0.76 Å) and K (1.5 Å), only 12 $mAh \cdot g^{-1}$ are delivered by sodium insertion into graphite. A low stage index for Na-GIC has never been observed under moderate conditions; only higher stage compounds such as NaC_{48}, NaC_{64}, NaC_{80}, have been reported.[3,4,5] Stage 1 Na-GIC formation has been demonstrated to be thermodynamically unfavorable, making sodium plating upon graphite, rather than its intercalation into it, more likely.[6] When Nobuhara et al. calculated the formation energies of AM–GICs they demonstrated that Na–GICs are energetically unstable due to a greater degree of change of the stretched C–C bond lengths in the

graphite layers.[7] Recently Moriwake et al. investigated the change in chemical bonding between graphite and alkali metal (AM) ions.[8] By first-principle calculations on Li, Na, K, Rb, and Cs GICs, the authors found that the formation energies of GICs AMC_6, becomes less negative (less stable) as ion size decreases from Cs to Na (Figure 4.2a). As the electronegativity of alkali

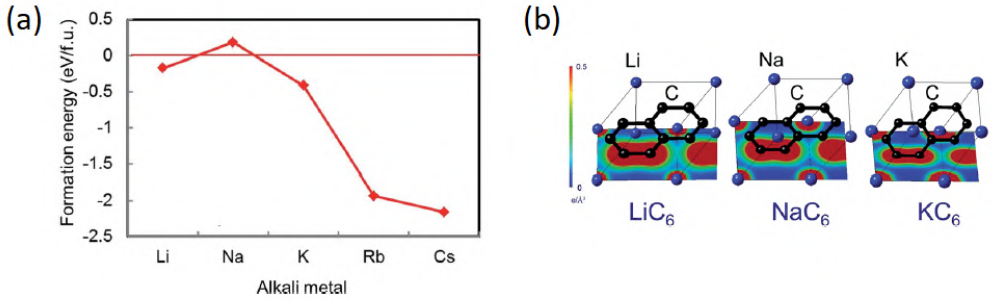

Figure 4.1: (a) Calculated formation energies of AMC_6 for AM:Li, Na, K, Rb,and Cs in order of increasing atomic number. (b) Electron densities for compositions LiC_6,NaC_6 and KC_6 plotted to the same scale. From.[8]

metal atoms decreases down the period, the iconicity of the bond between metal and C atoms increase.As the ion radius decreases, the metal–carbon bond becomes progressively weaker, with formation energies becoming more positive until for Na-GIC the formation energy is positive (i.e., NaC_6 is unstable).The much smaller Li ion represents an exception to this trend, as its bonds with C atoms contain a covalent component, resulting in a negative formation energy. Indeed the electron densities for LiC_6, NaC_6 and KC_6 reported in Figure 4.2b show that in Li–C bonds there is a certain amount of sharing of electrons between atom species, in other words, a non-negligible covalent bond component exists. In contrast to Na-GIC and K-GIC, the increased covalent bonding in Li-GICs is sufficiently large to overcome the decrease in the ionic component, so that Li-GICs are more stable than Na-GICs.
Strategies to overcome the issues of graphite with sodium have been recently proposed. Wen et al. demonstrated that expanding the interlayer distance of graphite along the c axis by introducing functional groups, a capacity of $284mAh \cdot g^{-1}$ was delivered at $20mA \cdot g^{-1}$, with a promising capacity retention of 73% after 2000 cycles when cycled at $100mA \cdot g^{-1}$. This work stressed the importance of both the concentration of oxidized carbon sites, namely surface oxygen, and the necessity to maintain a long-range vertical ordering.[9] Other than expanding the graphite interlayer distance, it has been proven that sodium ions can co-intercalate with specific solvents into the structure

of graphite (solvent co-intercalation). Indeed, in 2014 Jacke et al. were able able to reversibly insert sodium ions using a diglyme-based electrolyte solution. The reported reaction is:[10]

$$C_n + e^- + Na^+ + y\ Solv \rightleftharpoons Na^+(solv)_y\ C_n^- \tag{4.1}$$

The graphite revealed a surprisingly high coulombic efficiency in the first cycle (around 90%), low overpotential (smaller than 100mV) and superior cycle life. The maximum capacity was $100 mAh{\cdot}g^{-1}$ (close to the theoretical one $101.83 mAh{\cdot}g^{-1}$). Structural XRD analysis confirm graphite layers expansion along c axis, leading to a total volume expansion of 15 %. Theoretical studies hypothesized a ether co-intercalation of 1-2 molecules of diglyme considering that alkali metal ions are preferentially coordinated by six oxygen atoms.[11]
As the utilization of pure graphite was discouraged for long time, other carbonaceous materials have been extensively investigated as alternatives. A large number of non-graphitic carbons, including partially crystalline hard carbons and soft carbons, demonstrated a reversible sodium uptake with mechanisms other than pure intercalation (the term non-graphitic refers to the lack of long range periodic structural order). Soft carbons, obtained from the pyrolisis of liquid or gas precursors, are defined as non-graphitic, graphitizable carbons. In this latter case, if the temperature reaches over 1000^oC the long range order of graphite can be restored.[11] On the other hand, hard-carbons, generally obtained from the pyrolisis of solid precursors, are known as a $non-graphitizable$ carbon materials. Even at temperatures as high as 3000^oC indeed, the disordering along the c direction and the in plane hexagonal network of carbon atoms inhibits the graphitization. Compared to this latter class of carbon materials, soft-carbons have lower specific capacities and slightly higher working potential.
Hard carbons have an unique structure of randomly distributed and cross-linked graphitic microdomanis interposed between randomly few graphene layers or amorphous domains (Figure 4.2a). This complex structure that has been described as $falling\ cards$, confers a porous nature to hard carbons, whose degree depends on pyrolisis conditions. As proven by Gomez-Martin and co-workers the structural order can be somewhat controlled by heat treatment parameters, which in turn affect the capacity and charge-discharge profile.[13] In particular, the carbonization temperature appears to have a fundamental role on the sodium storage. Indeed, the literature reports a trend of increasing capacity with the increasing heat treatment temperature between 1200-1500^oC, followed by a decrease at temperatures above 1500^oC.[13] The authors reviewed also how the source of carbon precursor can strongly influence the structure of the hard carbon and the Na^+ uptake kinetics.

The profile of sodium ion insertion into hard carbon generally consists on two different regions (Figure 4.2b): a sloping region above 100 mV, and a second flat region below 0,1V ($vs\ Na^+/Na$). According to the early work of Stevens et al. the sloping region is ascribed to defect-assisted Na insertion into pseudographitic regions, whereas the flat plateau accounts for the sodium adsorption and filling of micropores.[14] Ex-situ X-Ray diffraction, Raman spectroscopy and nuclear magnetic resonance demonstrated the formation of quasi metallic clusters into the micropores of hard carbons.[15,16] However, many authors reported results that contradict this theory and pro-

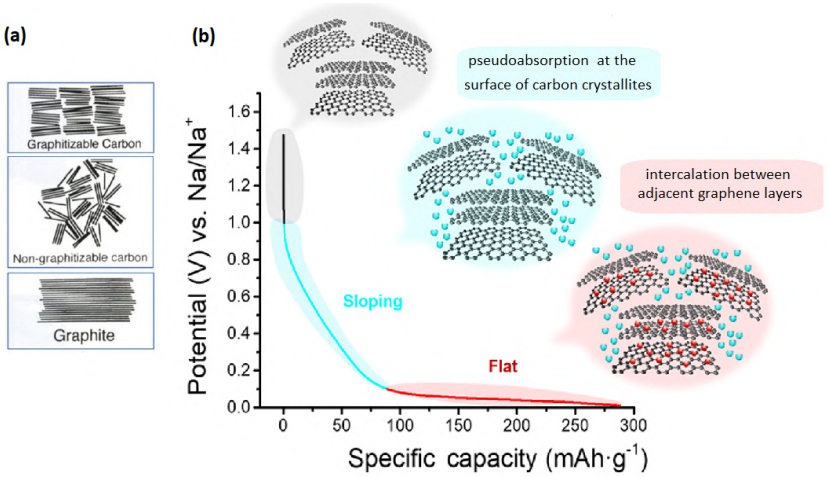

Figure 4.2: (a) Depiction of different carbonaceous materials. From top to bottom: non-graphitic graphitizable carbon, non-graphitic non-graphitizable carbon and graphite. (b) Sodium uptake into hard carbons according to the so called *absorption-intercalation* mechanism

posed an opposite model, i.e. the $absorption - intercalation$ mechanism (Figure 4.2b). Doubts about the intercalation-absorption mechanism arose when Matei-Ghimbeu et al. excluded the nanoporosity filling of micropores in the low-potential flat region with a comprehensive investigation of porosity evolution.[17] The correlations between structural evolution at different temperatures and electrochemical properties made by Gomez-Martin et al. also supported the absorption-intercalation mechanism. The reaction mechanism is still matter of debate in literature, as large discrepancies are reported.[13] From the application point of view, a major drawback of nearly all hard carbons is the significant irreversible capacity correlated with the first sodiation. Low coulombic efficiency in the first cycle is highly energetically problematic since it induces anode and cathode balancing issues, also in terms of sodium ions available inside the cell.

4.3.2 Other insertion anodes

Other inorganic compounds are known to intercalate sodium-ions at potentials close to 0 V (vs Na/Na^+). Among those TiO_2-based materials and layered transition metal carbides have been reported. The environmental friendliness, easily tunable synthesis, non-toxicity, and unique physical properties of titanium oxide make this material object of continuous studies. The oxide, in its different polymorphs (anatase, rutile, brookite and $TiO_2 - B$) has been analyzed for applications that range from photo-catalysis, to sensor technology, medicine and ultimately energy storage. The Ti^{3+}/Ti^{4+} redox couple is electrochemically active at potentials from 0.5 to 1.0 V vs Na/Na^+.[18] The mechanism of sodium uptake by TiO_2 is still controversial. Some studies reported intercalation of sodium ions into nano-sized anatase, whereas other groups proposed a conversion-like process which involves metallic Ti.[19] Sodium titanate ($Na_2Ti_3O_7$) prepared via ball milling has also been found to be active towards sodium and was reported to insert 2 sodium ions per formula unit at low potential ($\approx 0.5V$ vs Na/Na^+) with two stable charge/discharge plateaus.[20] Structural analysis revealed a variation of the joint angles between Ti-O block with the variation of the sodium content. This overall structural flexibility was never observed in transition metal oxides. Recently Longoni et al. revealed the importance of different anatase facets exposure with systematic morphological control. Using a solvothermal method, the authors employed surfactants as capping agent to direct crystal growth. Rhombic Elongated (RE), Rhombic (R) and nanobars (NB)-like particles revealed noticeable difference in the crystal face exposure as well as different electrochemical properties. Combining the electrochemical data and TEM analysis, it was therefore suggested that different facets may inhibit or improve the sodium uptake (Figure 4.3).[18]

Transition metal carbides (MXenes) are a class of 2D transition metal carbides and carbonitrides firstly proposed in 2011.[21] Their general formula is $M_{n+1}X_nT_x$ (n = 1,2,3) where M is an early transition metal, X is carbon or nitrogen and T_x represents surface functionalities (such as hydroxyl, oxygen, fluorine).[22] Mxenes are synthesized by selective etching of the A element from their layered precursors MAX phases a family of over 70 carbides and nitrides. The most studied MXenes are titanium carbides $Ti_3C_2T_x$ and Ti_2CT_x. From when they were proposed for the first time proposed as anode materials for LIBs and NIBs, the debate focused on the reaction mechanism, possibly capacitive/pseudocapacitive involving material surface,[23] or more based on a pure intercalation of desolvated Na ions.[24] Wang et al. tried to shed light onto the mechanism of reaction using DFT and scanning transmission electron microscopy (STEM) and they emphasized the topotactic

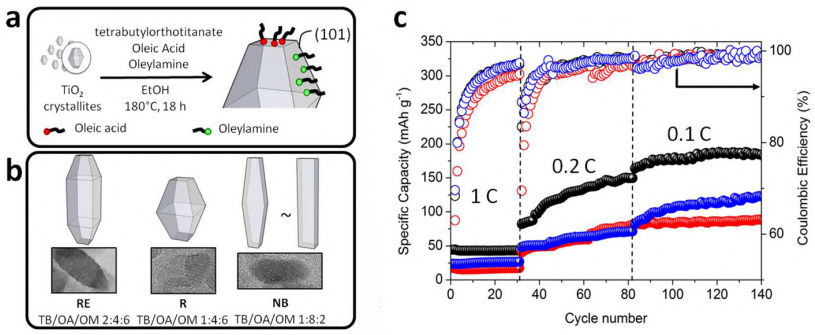

Figure 4.3: (a) Schematic representation of the shape-controlled growth mechanism and synthesis condition of TiO_2 crystallites thanks to the selective capping effect of oleic acid (OA) and oleylamine (OM); (b) 3D sketch of the investigated morphologies with the corresponding TEM magnification on single particles and the relative amount of the three reactants employed in the synthetic routes; (c) GCPL performance of RE, R, and NB electrodes (black, red, and blue curves, respectively) at different C-rates.[18]

localization of functional groups (e.g., OH-, F-, O2-) and intercalated Na atoms on the top site of the central-Ti atoms and C atoms on the $Ti_3C_2T_x$ layers.[25] Thanks to the high electronic conductivity along the 2D-layers, that can be tuned varying the amount of surface functionalities, high power performances, similar to supercapacitor ones, have been achieved.[26,27,28]

4.4 Alloying materials

Differently from insertion and intercalation compounds, where the number of sodium-ions per formula unit is constrained by the stability of their framework, alloying materials can withstand one or multiple alkali metal atoms per single Na-alloying atom. Table 4.1 summarizes the most studied Na-alloying elements and provides some insights of their electrochemical properties.

The significant sodium uptake has dramatic consequences on the crystal structure of the host. Although the reaction pathway is different for the different alloying materials, the remarkable volume variation that occurs during cycling, if not properly addressed, leads to irreversible consequences and fast capacity fading. The electrochemical performances of Sn in SIBs are generally inferior to LIBs. The understanding of the reaction mechanism and the resulting rational design of the material is therefore the most effective strategy to improve the performances of Sn for SIBs. However, the alloying mechanism of Sn still remains elusive, and experimental results are generally

inconsistent with DFT calculations. Ex-situ experimental studies on metallic tin, identified only four different compositions, namely $NaSn_3$, $\alpha - NaSn$, Na_9Sn_4 and crystalline $Na_{15}Sn_4$. Conversely, calculations predicted the alloying to proceed through the $NaSn_5$, $NaSn$, Na_9Sn_4 and $Na_{15}Sn_4$.[31] The authors suggested that the non-correspondence between the calculated and experimental plateaus is only apparent and is related to the intrinsic thermodynamic limits in achieving complex crystalline intermetallic phases, even though stable, at room temperature (Figure 4.4).The low mobility of sodium and morphological specific features could therefore account for the appearing of amorphous phases and the deviation from DFT calculations. To achieve

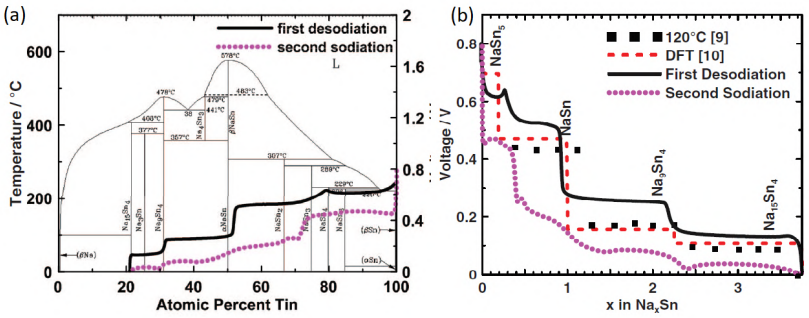

Figure 4.4: (a) Sn charge-discharge profiles superimposed to Na-Sn phase diagram; (b) Experimental RT sodiation-desodiation curves superimposed to DFT calculations and measures taken at 120^oC.[31]

the necessary mechanical stability, carbon composites as often reported in the literature. For example, Li et al. designed of 1D particles encapsulated into carbon spheres and reported 78% capacity retention after 800 cycles at $2A{\cdot}g^{-1}$.

	Sodiated Phase	Theoretical capacity ($mAh \cdot g^{-1}$)	Volume expansion (%)	Average voltage (vs Na/Na^+ V)
Sn	$Na_{3.75}Sn$	847	420	≈ 0.24
Sb	$NaSb$	660	393	≈ 0.64
Pb	$Na_{3.75}Pb$	482	$\approx$400	≈ 0.34
Ge	$NaGe$	576	205	≈ 0.54
P	Na_3P	2596	$\approx$ 490(red)	≈ 0.40
Si	$Na_{0.76}Si$	725	114	≈ 0.23

Table 4.1: Most relevant sodium-alloying materials and their electrochemical properties. The $Na_{0.76}$Si alloy has been shown to occur only for amorphous Si.[29,30]

Because of its high electrical conductivity, resulting in exceptional rate capability,[32] antimony has been extensively studied for SIBs. Sb can provide a capacity of $660 mAh \cdot g^{-1}$ with a working potential of ≈ 0.64. Other than embedding Sb nanoparticles in carbon or carbon nitrogen-doped composites,[33,34] nanoporous Sb can retain the structural integrity, while maintaining high electron transport properties, without hybridizing with any other matrices. Liu et al. prepared coral like and honeycomb-like nanoporous Sb from Al-Sb alloy ribbon via simple chemical de-alloying method.[35] The authors reported a capacity retention of 86,9% after 200 cycles, and capacities of $420 mAh \cdot g^{-1}$ at $3.3 A \cdot g^{-1}$(Figure 4.5).

Among the elements of the Group 14 in the periodic table, Germanium

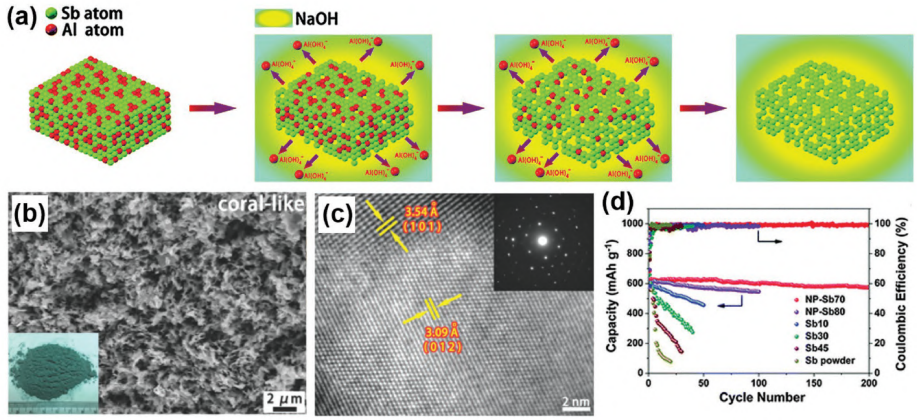

Figure 4.5: (a) Depiction of the synthesis of nanoporous Sb (NP-Sb) via chemical de-alloying; (b-c) SEM and TEM images of the NP-Sb; (d) Cycling stability of the NP-Sb at $0,1 A \cdot g^{-1}$.[35]

recently attracted considerable attention for several reasons.[36] Firstly, Ge shows strong thermodynamic tendency to alloy with sodium (comparable to Sn); secondly, moderate volume expansion could improve the capacity retention of the anode; finally the conductivity of Na^+ in Ge is comparable to the one in tin. It is therefore not surprising that Ge nanoparticles embedded into interconnected hollow carbon boxes via carbothermal reduction, showed capacities of $346 mAh \cdot g^{-1}$, close to thetheoretical value ($369 mAh \cdot g^{-1}$ for NaGe).[37] The low working potential (0.4 V vs Na/Na^+), and its ability to store up to three sodium ions per atom delivering a theoretical specific capacity of $2596 mAh \cdot g^{-1}$, makes of phosphorous one of the most promising anode candidates for SIBs. If phosphorous exists in different allotropes, most of them are either too toxic or expensive to be considered for energy storage applications. White phosphorous, for example is poisonous and undergoes

spontaneous combustion in air. Black phosphorous (BP), with its layered crystal structure that resembles graphite and high electronic conductivity ($\approx 0.300 S/m$) attracted considerable attention. However, when Komaba et al. tried to investigate the full reduction of BP, they found a complete conversion from BP to Red phosphorous. Black phosphorous was not found after the re-oxidation.[38] As a matter of fact, red phosphorous (RP) is both inexpensive, and stable in air up to 260^oC. Worth to be mentioned is the fact that, despite being stable under the anhydrous operating conditions of a battery, the sodiated phases react with water and produce toxic gases. The non negligible volume change (over 490%) during the alloying reaction and the low electronic conductivity ($10^{-14} S\ cm^{-1}$) are the two main disadvantages of RP.[39] These issues have been addressed by reducing the particle size and producing RP-carbon composites.[40,41] The effect of particle-size distribution on the electrochemical performances has been systematically studied by Capone et al.[42] The authors separated into two steps the reduction of particle size and the synthesis of the RP-Carbon composite, and found that non only the mean particle size but also the distribution of the particle sizes significantly affected the electrochemical performances. The breaking of bigger particles (in the range of $2 - 10 \mu m$) was suggested to be critical to mitigate the pulverization and the resulting capacity loss that commonly occurs during cycling.

4.5 Transition Metal Oxides that undergo conversion reaction

As discussed in chapter 3, transition metal oxides that undergo conversion reaction have been identified and proposed in the literature as promising high-energy-density anode candidates for sodium-ion batteries. This class of materials have theoretical capacities ranging from $700 mAh \cdot g^{-1}$ to over $1000 mAh \cdot g^{-1}$. Among the other conversion based materials, oxides are thermodynamically favored owing to the advantageous potential gain in the reaction with sodium if compared to lithium. The major challenge for practical application of conversion materials, is the volume variation (between 150-250%) related to the significant structural change that occurs during cycling. In conversion oxides, besides the full reduction of the metal non conductive Na_2O forms. This introduces additional structural strain connected to the lattice mismatch between the metal and sodium oxide that can lead to a complex reaction mechanism. Co_3O_4 is a well studied conversion material for both sodium-ion and lithium-ion batteries. As for alloying

and other conversion materials, nanostructuring Co_3O_4 has been reported to improve the kinetics and enhance the capacity retention. Longoni et al. analyzed morphology-properties correlations and reported that different hierarchical structures have different electrochemical properties. In particular, three different morphologies of spinel Co_3O_4 were synthesized, and it was demonstrated that needle-like nanoparticles with high aspect-ratio had improved capacity retention (Figure 4.6).[43] Regarding the reaction mechanism,

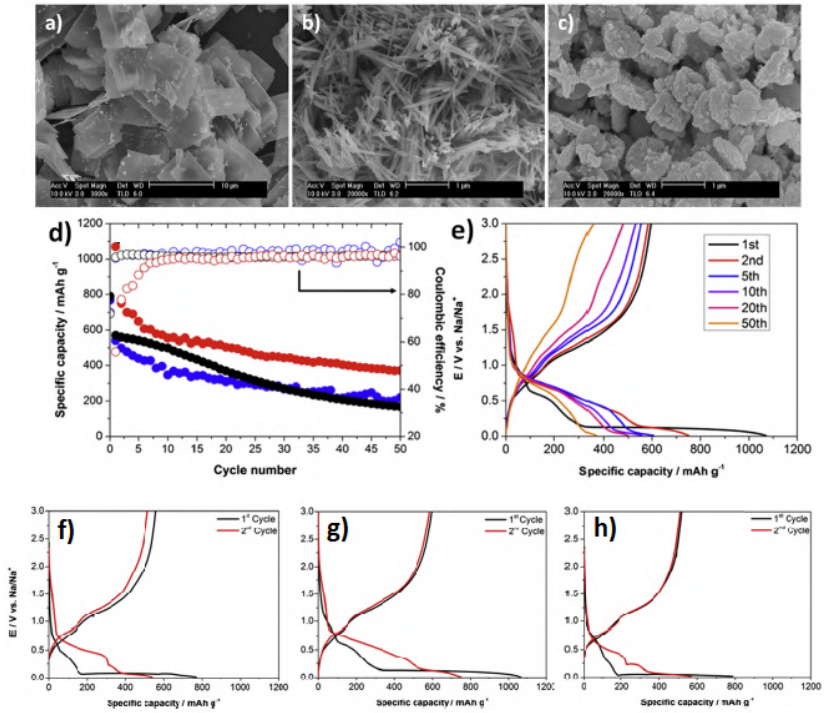

Figure 4.6: SEM images of the (a) slabs (Co_s), (b) needle-like (Co_n), and (c) flake (Co_f) synthesized Co_3O_4 particles, and electrochemical characterization(d-h). Colors refer to: Co_s (blue), Co_n (red), Co_f (black). Al the electrodes have been charged and discharged at C/10.[43]

ex situ XRD revealed the formation of CoO rather than restoring the initial Co_3O_4 phase after the first sodiation-desodiation cycle. From this finding, the authors therefore suggested that the lower capacity registered during the subsequent cycles may arise from the cycling of CoO instead of the Co_3O_4. A different material design has been proposed by Yang et al. A 3D porous structured was obtained by a nanocasting synthesis that utilized nanoporous silica as a templating agent. The nanoporous Co_3O_4 demonstrated surprisingly long cycle life (nearly $500 mAh \cdot g^{-1}$ after 100 cycles). The capacity,

although considerably lower that the theoretical one, was still interesting compared to carbonaceous materials. To improve the electrical conductivity and the stability of the electrode, carbon composites have also been employed. Among others, graphene oxide sheets and carbon nanotubes have also been investigated.[44,45] In the case of carbon composites however, it is hard to distinguish between the capacity arising from carbon and the one effectively coming from the conversion oxides. Iron oxide is a cheaper, eco-friendly, high capacity alternative to cobalt oxides. The electrochemical properties of the several crystalline phases, hematite ($\alpha - Fe_2O_3$), magemite ($\gamma - Fe_2O_3$) and magnetite Fe_3O_4 have all been reported in the literature. Several iron oxide-carbon composites have been reported in the literature to overcome the sluggish kinetic properties (related to low electronic conductivity).[46,47] Among others, hierarchical hollow hybrid Fe_2O_3-MIL-101(Fe)/C composite derived from metal organic framework reported the impressive capacity retention of 93.2% ($662 mAh \cdot g^{-1}$) after 200 cycles.[48] The excellent electrochemical performances were ascribed to the unique hollow structure that lead to enhanced contact area between the active sites and short ionic-electronic diffusion length. The conventional conversion mechanism is generally accepted as the main occurring process for iron oxide, but a detailed description of the phases evolution upon sodiation is still lacking. Other than iron oxides, also tin oxides have been reported as safer anodes for SIBs, compared to Co_3O_4. The reaction of sodium with both SnO and SnO_2 has been reported.[49,50]

Bibliography

[1] L. Chen, M. Fiore, J. E. Wang, R. Ruffo, D.-K. Kim, and G. Longoni, "Readiness Level of Sodium-Ion Battery Technology: A Materials Review," *Adv. Sustain. Syst.*, vol. 1700153, p. 1700153, 2018.

[2] J.-Y. Hwang, S.-T. Myung, and Y.-K. Sun, "Sodium-ion batteries: present and future," *Chem. Soc. Rev.*, vol. 46, no. 12, pp. 3529–3614, 2017.

[3] A. Metrot, D. Guerard, D. Billaud, and A. Herold, "New results about the sodium-graphite system," *Synth. Met.*, vol. 1, no. 4, pp. 363–369, 1980.

[4] N. Adhoum, J. Bouteillon, D. Dumas, and J. C. Poignet, "Electrochemical insertion of sodium into graphite in molten sodium fluoride at 1025 C," *Electrochim. Acta*, vol. 51, no. 25, pp. 5402–5406, 2006.

[5] P. Ge and M. Fouletier, "Electrochemical Intercalation of sodium in graphite," *Solid State Ionics*, vol. 28–30, pp. 1172–1175, 1988.

[6] Y. Okamoto, "Density functional theory calculations of alkali metal (Li, Na, and K) graphite intercalation compounds," *J. Phys. Chem. C*, vol. 118, no. 1, pp. 16–19, 2014.

[7] K. Nobuhara, H. Nakayama, M. Nose, S. Nakanishi, and H. Iba, "First-principles study of alkali metal-graphite intercalation compounds," *J. Power Sources*, vol. 243, pp. 585–587, 2013.

[8] H. Moriwake, A. Kuwabara, C. A. J. Fisher, and Y. Ikuhara, "Why is sodium-intercalated graphite unstable?," *RSC Adv.*, vol. 7, no. 58, pp. 36550–36554, 2017.

[9] Y. Wen *et al.*, "Expanded graphite as superior anode for sodium-ion batteries.," *Nat. Commun.*, vol. 5, no. May, p. 4033, 2014.

[10] B. Jache and P. Adelhelm, "Use of graphite as a highly reversible electrode with superior cycle life for sodium-ion batteries by making use of co-intercalation phenomena," *Angew. Chemie - Int. Ed.*, vol. 53, no. 38, pp. 10169–10173, 2014.

[11] W. A. Henderson, "Glyme-lithium salt phase behavior," *J. Phys. Chem. B*, vol. 110, no. 26, pp. 13177–13183, 2006.

[12] H. Hou, X. Qiu, W. Wei, Y. Zhang, and X. Ji, "Carbon Anode Materials for Advanced Sodium-Ion Batteries," *Adv. Energy Mater.*, pp. 1–30, 2017.

[13] A. Gomez-martin, J. Martinez-fernandez, M. Ruttert, M. Winter, T. Placke, and J. Ramirez-rico, "Correlation of Structure and Performance of Hard Carbons as Anodes for Sodium Ion Batteries," *Chem. Mater.*, 2019.

[14] D. a. Stevens and J. R. Dahn, "High Capacity Anode Materials for Rechargeable Sodium-Ion Batteries," *J. Electrochem. Soc.*, vol. 147, no. 4, p. 1271, 2000.

[15] S. Komaba *et al.*, "Electrochemical Na insertion and solid electrolyte interphase for hard-carbon electrodes and application to Na-ion batteries," *Adv. Funct. Mater.*, vol. 21, no. 20, pp. 3859–3867, Oct. 2011.

[16] K. Gotoh *et al.*, "NMR study for electrochemically inserted Na in hard carbon electrode of sodium ion battery," *J. Power Sources*, vol. 225, pp. 137–140, 2013.

[17] C. Matei Ghimbeu, J. Górka, V. Simone, L. Simonin, S. Martinet, and C. Vix-Guterl,

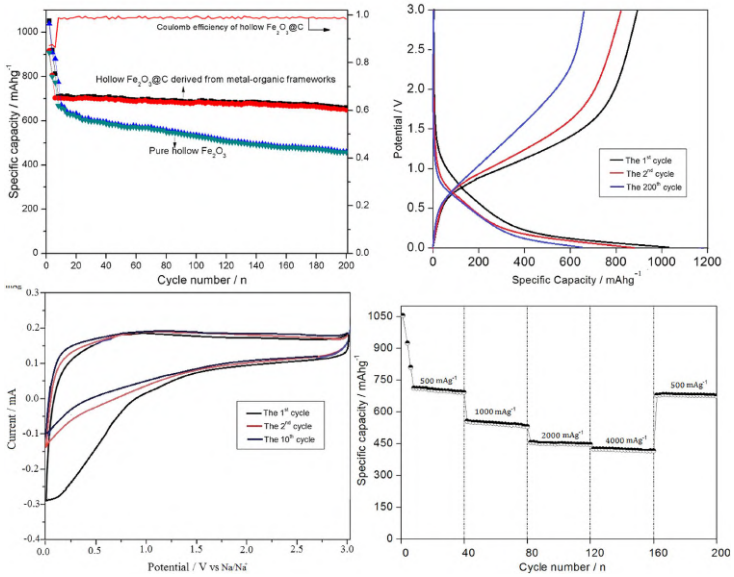

Figure 4.7: Electrochemical performance of the hierarchical hollow Fe_2O_3MIL-101(Fe)/C electrodes: (a) cycling performance of bare Fe_2O_3 and Fe_2O_3-MIL-101(Fe)/C measured at $200mA \cdot g^{-1}$ and (b) relative charge/ discharge profiles of Fe_2O_3MIL-101(Fe)/C electrode for the 1st, 2nd, and 200th cycle; (c) cyclic voltammetry results of the Fe_2O_3-MIL-101(Fe)/C electrode at the scan rate of $0.05mV \cdot s^{-1}$. (d) Rate capability of the Fe_2O_3-MIL-101(Fe)/C electrode from $500mA \cdot g^{-1}$ to $4A \cdot g^{-1}$. Electrode potential range of 0.05–3.0 V vs. Na+/Na.[48]

Chapter 5

Electroactive Materials for Potassium Ion Batteries

5.1 Introduction

Potassium-ion batteries are emerging as a potential alternative to LIBs with similar benefits of sodium-ion batteries, but have the additional advantage that graphite can be used as negative electrode. The price of potassium salts needed for the the electrode fabrication (K_2CO_3) is similar to that of Na_2CO_3, which is significantly cheaper compared to Li_2CO_3. In addition, aluminum does not form alloys with potassium, and it can therefore be used as current current collector for the negative side, instead of copper; this not only reduces the price but also decreases the weight of the current collector and can address the over-discharge problems.[1] Besides having the largest atomic radius compared to lithium and sodium (see Chapter 3.8.1), potassium ions have the smallest Stokes' radius in organic electrolytes, indicating higher ion mobility.[1] Based on molecular dynamic simulations, Pham et al. proved that the differences between solvation shell in ethylene carbonate significantly influence the ion dynamics, and lead to a K^+ diffusion coefficient three times larger than that of Li^+.[2] The mentioned advantages suggest that replacing lithium with potassium would enable to increase the rate capability and/or realize high mass loading electrodes without sacrificing the capacity.[3] Nevertheless, the diffusion of potassium in solid and the overall reaction kinetics should be also considered. The standard reduction potential of the K/K^+ redox couple is 0.22 V lower than Na/Na^+ (-2,93V and -2,71V vs. SHE, respectively) and comparable with Li/Li^+.[4] This ultimately means that comparable or eventually higher energy densities might be achieved by KIBs compared to LIBs and NIBs. In the next chapter the most important

active materials for KIBs are reviewed.

5.2 Negative active materials for KIBs

Potassium metal cannot be practically used on the negative side in KIBs, because of its high reactivity, poor cycling efficiency and severe safety concerns.[5] The research has been focused on three main categories: intrecalation, conversion, and alloying compounds.

5.2.1 Insertion anode materials

Despite the first demonstration of a potassiated graphite dates back to the 1950s,[6] graphite's failure in SIBs discouraged the study of carbonaceous materials for KIBs. Only recently a series of publications reported reversible electrochemical potassium intercalation into graphitic materials that leads to the KC_8 GIC (theoretical specific capacity $279 mAh \cdot g^{-1}$),[7,8,9] Liu et al reported the structural evolution of graphitic electrodes, by *in situ* XRD diffraction. The mechanism of potassium intercalation into graphite in carbonate electrolytes was proved to proceed through multiple stages, denoted as stage-n GICs. The stage index n is the number of graphitic layers between intercalation planes. n is determined from the diffraction angles Θ_l corresponding to the different $(00l)$ planes, using Bragg's law:[10]

$$l\lambda = 2I_c sin\Theta_l \tag{5.1}$$

As the distance between graphite layers is essentially unaffected by intercalation, the stage index n is calculated from:

$$I_c = (n-1)c_0 + d_s \tag{5.2}$$

where c_0 is the distance between adjacent graphene layers, and d_s is the distance separating two layers between which an intercalated layer is sandwiched. The reversible staging of K^+ ion insertion follows the sequence: C-KC_{36}-KC_{24}-KC_8(Figure 5.1).[10] Besides these intermediates, Fan et al. reported also the formation of stage 4 (KC_{48}) and suggested the appearing of stage 5 (KC_{60}).[11] Despite the large volume expansion ($\approx 60\%$) during cycling, graphite can reversibly intercalate K. To improve the first cycle coulombic efficiency and long term capability, Komaba et al reported the importance of binder selection. Compared to polyvinylidene fluoride (PVDF) and sodium carboxymethyl cellulose, K/graphite half cell displayed higher coulombic efficiency, and almost no capacity fading after 50 cycles, when

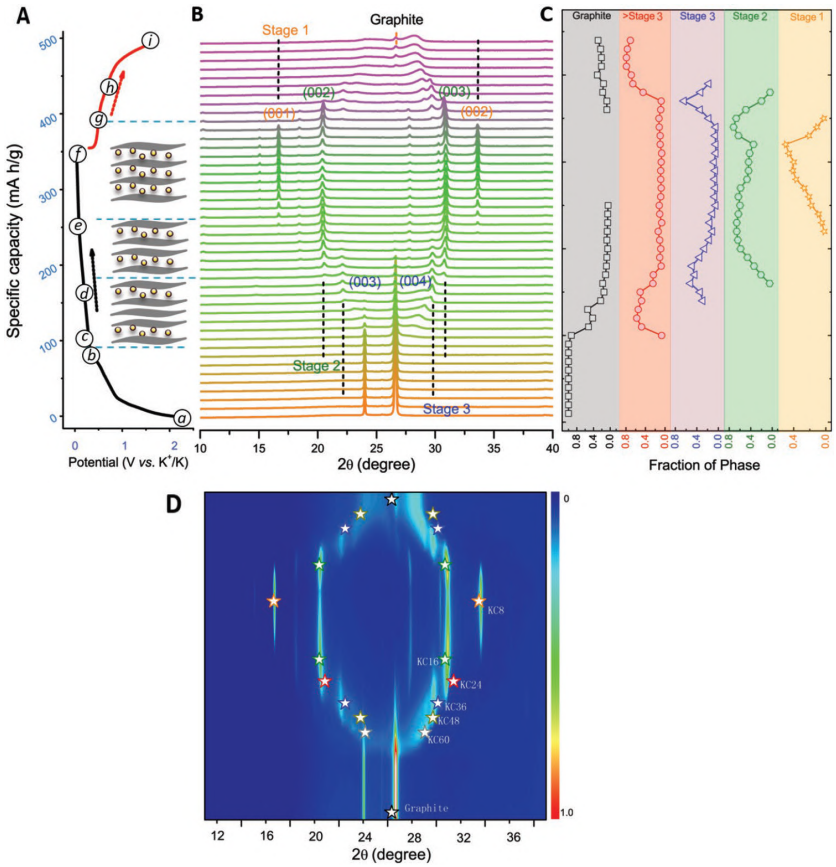

Figure 5.1: Structure evolution upon K^+ ions insertion and deinstertion. A) 1^{st} galvanostatic charging/discharging profile, B) recorded during in situ XRD measurement at C/20. Inset schematically illustrates the stage 3, stage 2, and stage 1. *In situ* X-ray diffraction patterns consisting of 44 spectra. C) Variation in the phase fractions of stages 1, 2, and 3, high-order stages, and unintercalated graphite during the same discharge/charge process. The relative fractions are quantified by integrating the Bragg-peak intensity corresponding to each stage. D) Simulated the two strongest XRD peaks (stars with the same color for each pair) for each KCx models.[10]

sodium polyacrilate was employed as a binder.[8] The effect of different potassium salts in the electrolyte, was investigated by Fan and co-workers. The authors found that in 0.8M KPF_6 in EC:EMC the capacity decayed after 80 cycles, whereas in highly concentrated $KN(SO_2F)_2$ (KFSI) based electrolytes, stable capacity was maintained for over 2000 cycles. The superior stability in KFSI-containing electrolyte was ascribed to the formation of a robust inorganic-rich passivation layer on the graphite anode.[11] Apart from

graphitic carbons, hard carbons, soft carbons and graphene oxide have also been reported as potassium intercalating anode materials.[12,13,14] Their capacity can exceed the theoretical capacity of graphite, however, the low tap density, higher average working potential compared to graphite, and large irreversible capacity in the first cycle are bottlenecks that need to be resolved to achieve practical battery applications.

5.2.2 Alloying materials

As for LIBs and SIBs, elements that form an alloy with potassium can be used as active materials for KIBs. These materials can generally accommodate a larger number of alkali metals, compared to intercalation materials. Kim et al. analyzed the energetics and the structural changes associated to sodium or potassium alloying with Sb, Si, Sn, P, Ge and Pb. Three general trends were observed (Figure 5.2):[15]

- the amount of potassium that can be alloyed is less than or equal to that of sodium, meaning that K-alloying anode capacities are expected to be smaller or equal that of their Na counterparts
- the average voltage for K-alloying, except for partial intermediates involved with P and Sb, is generally higher than that for Na
- the volume expansion for K-alloying anodes is larger than that for Na-alloys

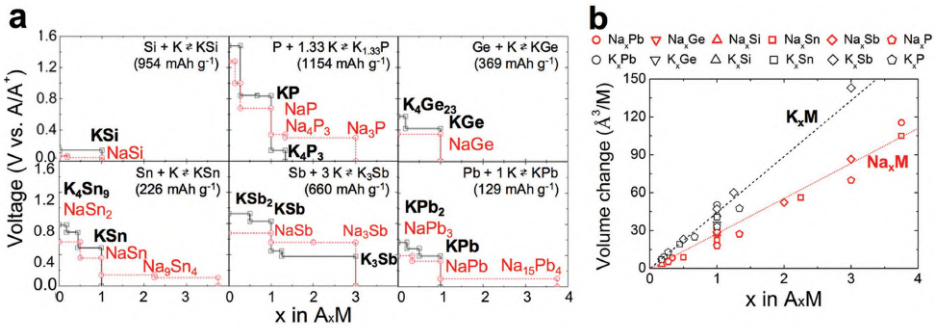

Figure 5.2: (a) Voltage–composition curves calculated for alkali alloying with different metals. (b) Volume expansion upon alloying alkali metals with different metals as a function of x in A_xM.[15]

Therefore, not only higher mechanical stress is expected to occur in potassium alloying reactions, i.e. lower cyclability is awaited, but also the energy

density is generally lower than that of sodium counterparts. As reported for sodium alloying materials, carbon conductive composites and material engineering have been utilized to buffer the volume variation during cycling and to increase the overall electronic conductivity. K alloying reactions have been observed experimentally for Sb, Sn, P, and Si. Sultana and coworkers, prepared a Sn-graphite nanocomposite as which sustained up to $170 mAh{\cdot}g^{-1}$ for 10-15 cycles, and reported bulk Sb to be electrochemically non active.[16] Recently, Zhang et al. reported phosphorus-based Sn_4P_3-C composites with first discharge capacity of $588.7 mAh{\cdot}g^{-1}$ at $50 mA{\cdot}g^{-1}$, with better capacity retention than P/C and Sn/C composites (Figure 5.3a,b).[17] The authors proposed a reaction mechanism and provided evidence for the enhanced cycling performance of the SnP3/C electrode by ex situ XRD experiments (Figure 5.3).

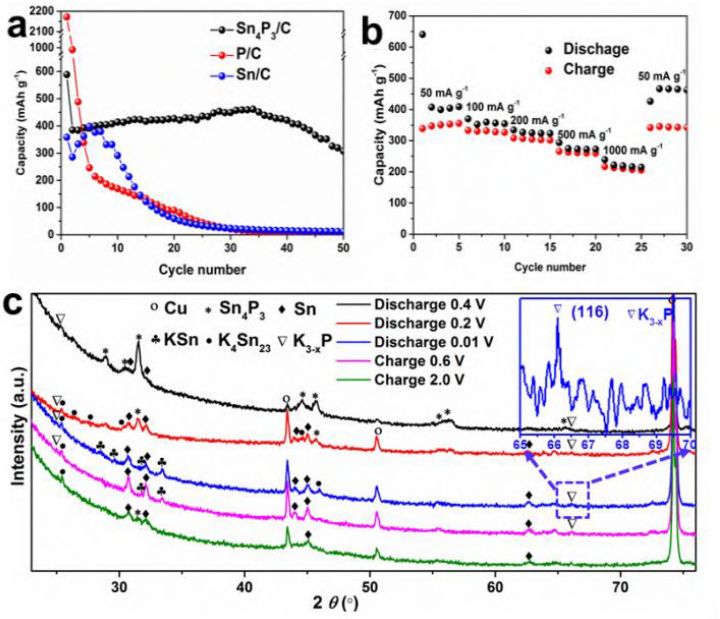

Figure 5.3: (a) Cycling performance of the Sn_4P_3/C, Sn/C, and P/C electrodes at $50 mA{\cdot}g^{-1}$; (b) Rate performance of Sn_4P_3/C electrode; (c) *ex-situ* XRD patterns of cycled Sn_4P_3/C.[17]

5.2.3 Conversion materials

Compared to SIBs, fewer conversion materials have been reported for KIBs. Sultana et al. proposed hybrid Co_3O_4-Fe_2O_3 carbon composite prepared

by a molten salt method combined with ball milling process as anode material for both sodium and potassium-ion batteries.[18] In the latter case, a reversible capacity of $220 mAh \cdot g^{-1}$ at $50 mA \cdot g^{-1}$ was retained for 50 cycles. MoS_2 was was cycled in 0.8M KPF_6 and 0.8M KFSI in EC:DEC by Deng et al.[19] Discharge capacities of $227 mAh \cdot g^{-1}$ in the second cycle which decreased to $151.5 mAh \cdot g^{-1}$ after 200 cycles, were obtained in the KFSI based electrolyte, whereas the capacity rapidly decreased to less that $100 mAh \cdot g^{-1}$ after 60 cycles in the KPF_6 one (Figure 5.4). The XPS analysis of the MoS_2 surface after cycling revealed that the different capacity retention, linked to different coulombic efficiencies, may arise from the different SEI formed. A stable KF-rich SEI was found in KFSI-containing electrolyte, while an KF-deficient and organic species-rich, resulting from the decomposition of the electrolyte, SEI formed in KPF_6 containing electrolyte.

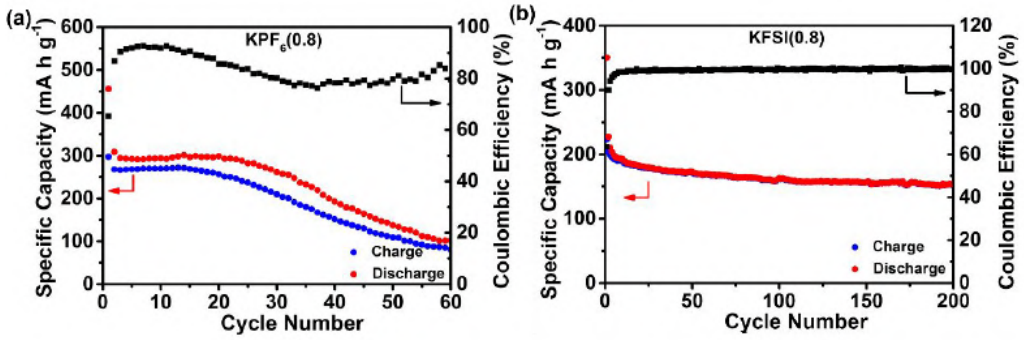

Figure 5.4: Cycling performance of the MoS_2 electrode tested at $100 mA \cdot g^{-1}$ in the (a) 0.8 M KPF_6 EC:DEC and (b) 0.8M KFSI EC:DEC electrolytes.[19]

In summary the most meaningful results on negative materials for KIBs have been the ones reported for graphite. Provided that an appropriate binder and electrolyte are selected, promising rate capability and capacity retention have been proved. Although other carbons have been shown to be electrochemically active with potassium, they are unlikely to rival graphite in terms of specific energy. Finally, untill now, most of the alloying and conversion materials have shown unsatisfactory electrochemical performances. These need to be improved if they are to be considered for practical applications.

5.3 Positive active Materials for KIBs

Most of the studied cathodes for KIBs can accommodate potassium ions by insertion reaction. The larger ionic radius of K^+ compared to Li^+ and

Na^+, makes finding a suitable positive active material a challenging task. Indeed positive materials with large enough channels, sufficient K^+ ionic and electronic conductivity, stable structure, high average working potential, and high capacity are needed. To date, it has been reported that potassium can be stored in a variety of structures: transition metal oxides, polyanionic compounds, hexacyanometallates.

5.3.1 Transition-Metal Oxides

Layered transition metal oxides can be conveniently categorized according to what Delmas et al proposed.[20] In this notation, O and P letters refer to how the alkali-metal is accommodated between layers, occupying central positions in the edge-sharing octahedral (O) or face-sharing prismatic (P) site. A number refers to the periodicity of the slab stacking along the c axis (Figure 5.5). For example, if the octahedral alkali metal and the octahedral transition metal slabs repeat in a period of three (ABCABC stacking) the layered structure is O3-type. Worth to be mentioned, a peculiar characteristic of these type of structures, is the possible interconversion among different layered geometries depending on the stoichiometry of the compound.

Layered A_xCoO_2 (A: Li, Na) are known to be used in secondary batteries. $LiCO_2$ for example, is a widely used cathode in portable electronic devices. Despite K_xCoO_2 with different K^+ contents were known from the 1975.[21], only in 2017 Komaba et al. reported reversible and topotactic intercalation of K^+ into a P2-type $K_{0.41}CO_2$ and P3-type $K_{2/3}CoO_2$ (Figure 5.6a-b). Both the compounds were found to be air-sensitive and showed similar profiles and specific capacities $\approx 60mAh \cdot g^{-1}$ (potential range 2-3.9V vs K/K^+). $K_{0.6}CoO_2$ with higher potassium content was later proposed by Ceder and co-workers.[22] However, the resulting capacity was similar to that of P2-type $K_{0.41}CO_2$. The structural changes occurring during the potassium de/intercalation were analyzed by *in situ* XRD(Figure 5.6c). The diffraction peaks corresponding to the $00l$ and $h01$ peaks shifted monotonically towards low (in discharge) and high (in charge) angles. The authors thereby confirmed the reversibility of the reaction. A full P2-$K_{0.6}CoO_2$/graphite cell was also reported (Figure 5.6d).

Manganese-based electroactive materials have also been proposed for KIBs. Vaalma et al. reported the electrochemical activity of a P2-type orthorhombic $K_{0.3}MnO_2$ ($Cmcm$ space group).[23] In the range 1.5-4V the oxide delivers a capacity around $130mAh{\cdot}g^{-1}$ with multiple phase transitions (Figure 5.7a). The capacity rapidly decreased when the electrode was tested up to 4V, but lowering the upper voltage cutoff to 3.5V (resulting capacity $\approx 80mAh{\cdot}g^{-1}$) led to a capacity retention of 68% after 700 cycles. The feasibility of lay-

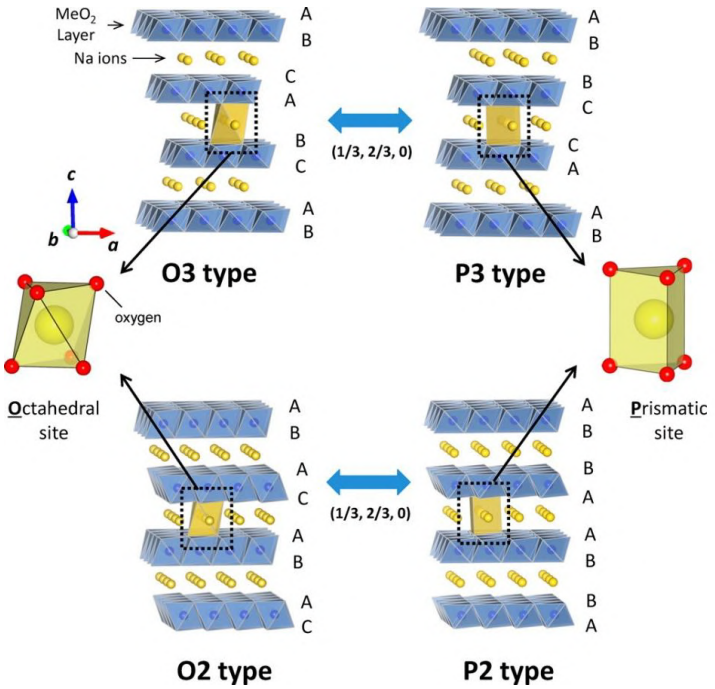

Figure 5.5: Sheets of edge-sharing MO_6 octahedral accommodate the alkali ion in between the TM-slabs. Depending on the geometry of the alkali environment, O and P structures can be distinguished.[20]

ered P3-type $K_{0.5}MnO_2$ was examined by Kim and co-workers. As it was reported for P2-type $K_{0.3}MnO_2$ narrowing the electrochemical window (1.5-3.9V) resulted in better capacity retention but lower capacity (Figure 5.7b). $K_{0.67}[Ni_{0.17}Co_{0.17}Mn_{0.66}]O_2$ was synthesized via co-precipitation reaction.[24] The compound crystallized into a P3-type layered structure with $R-3m$ space group. Differently from $K_{0.5}MnO_2$ the $c-axis$ elongated (20.628$\mathring{A}$ vs 19.085$\mathring{A}$). Such increase along the c direction might improve the ionic diffusivity of potassium ions between the oxide layers. The material synthesized by Kim et al. delivered a capacity of $\approx 80mAh{\cdot}g^{-1}$ at $20mA{\cdot}g^{-1}$ between 2.0 and 4.3 V (vs K/K^+). Worth to be mentioned the several phase transitions occuring during the K^+ de/insertion were not discernible, and a smooth variation of the charge/discharge profile was obtained (Figure 5.7c).

5.3.2 Transition-Metal Polyanions

A severe bottleneck of TM-oxides is their low operating working potential that lies between 2-3 V vs K/K^+. On the other hand, a similar trend to

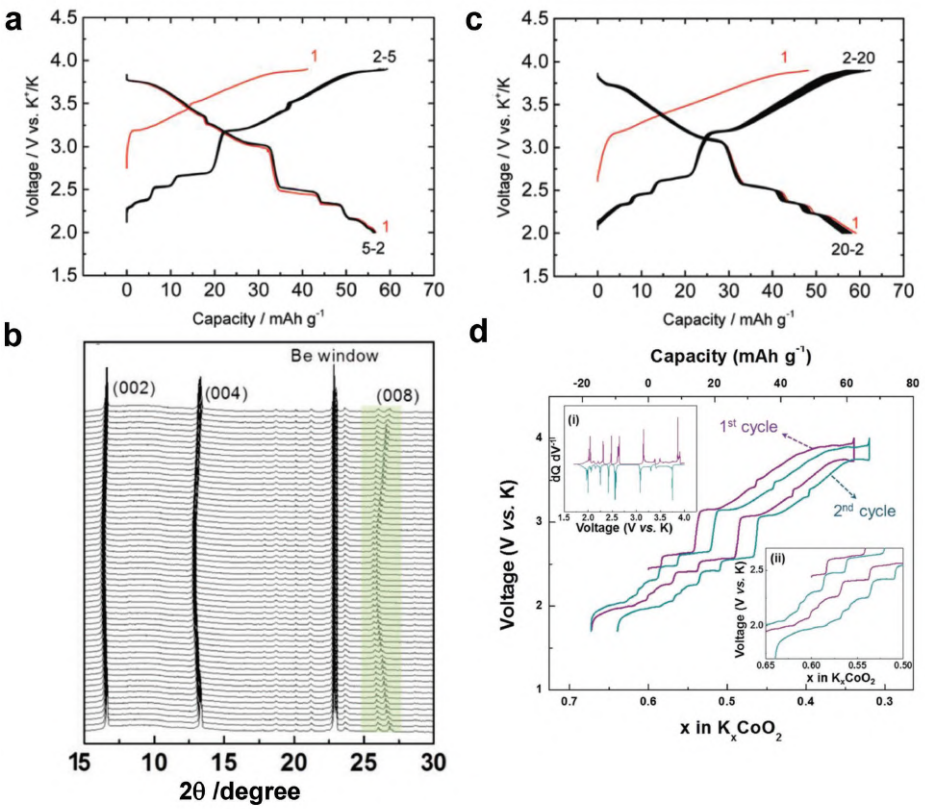

Figure 5.6: Charge and discharge curves over several initial cycles for (a) P2-$K_{0.41}CoO_2$ and (b) P3-$K_{2/3}CoO_2$.[21] (c) In situ XRD patterns of P2-$K_{0.6}CoO_2$ during charging and discharging recorded at $2mA{\cdot}g^{-1}$. (d) Charge–discharge curves for the P2-$K_{0.6}CoO_2$/graphite full cell at a current density of $2mA{\cdot}g^{-1}$.[22]

the one observed in lithium iron phosphate,[25] where the operating voltage can be tuned by the inductive effect, applies to potassium polyanions.[26] $KMSO_4F$ (M: Fe, Ni and Co) were investigated by Recham et al.[26] The interstitial space was reported to be sufficiently large to reversibly accommodate K^+ ions into the crystal structure. Indeed, K_xFeSO_4F was reported to reversibly insert potassium, leading to $K_0.8FeSO_4F$. However, compared to to Li^+, the K^+ uptake was accompanied with large polarization during the alkali-ion insertion (Figure 5.8a,b).[26] As predicted by DFT calculations in the Li^+ and Na^+ case, the kinetics might be improved by selecting the appropriate transition metal.

Following the succes of sodium-vanadium polyanion compounds, Chihara et al. synthesized $KVPO_4$ and $KVPO_4F$, and tested their electrochemical

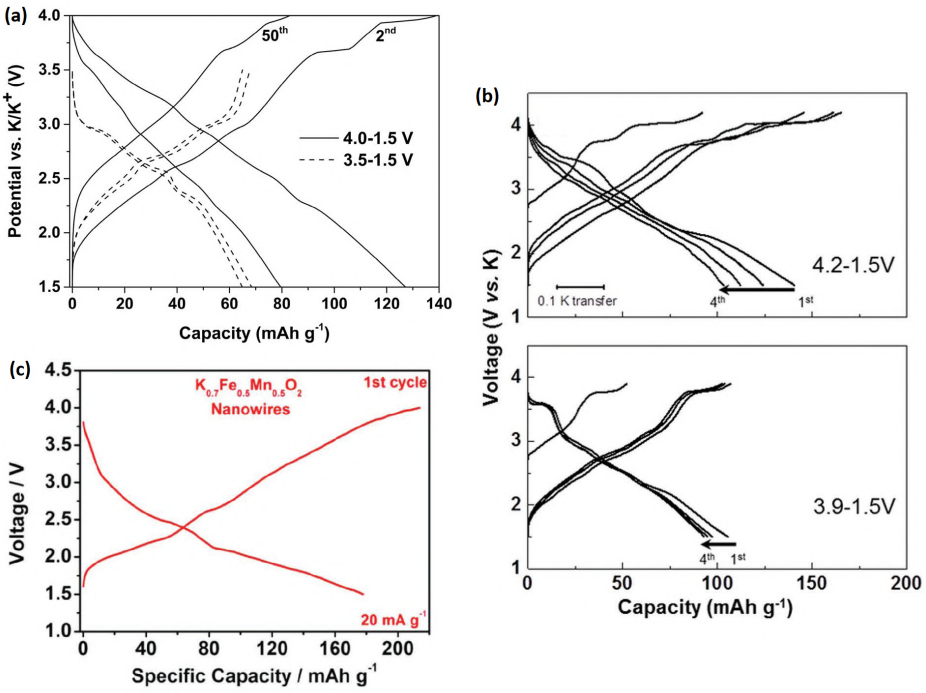

Figure 5.7: (a) 2^{nd} and 50^{th} charge/discharge profiles of P2 type $K_{0.3}MnO_2$ at 0.1C in the voltage ranges 3.5–1.5 V and 4.0–1.5 V; (b) galvanostatic voltage–capacity profiles of P3-type $K_{0.5}MnO_2$ with two different voltage cutoffs; (c) first charge and discharge curves for P3-type$K_{0.7}[Fe_{0.5}Mn_{0.5}]O_2$ nanowires recorded at $20mA{\cdot}g^{-1}$.[24]

properties in K half-cells (Figure 5.8c-f).[27] $KVPO_4$ and $KVPO_4F$ delivered $80mAh{\cdot}g^{-1}$ and $\approx 90mAh{\cdot}g^{-1}$ respectively, with high average working voltage (4.02 V for the fluorinated-polyanion and 3.95 V vs K/K^+ for the non-fluorinated one). Negligible capacity decay was registered for both the electrodes after 30 cycles, but the discharge/charge coulombic efficiency was quite low.

5.3.3 Prussian Blue Analogs

Prussian blue analogues (PBAs), are a group of metal cyanoferrates with general formula $A_xP^J[R^K(CN)_6]_{1-y}{\cdot}wH_2O$, where A is the inserted alkali-metal ion and P and R are transition-metals octahedrally coordinated to six cyanide ligands via the Nitrogen or the Carbon atom, respectively (Figure 5.9). Here y is the fraction of hexacyanoferrate complex vacancies (primary lattice defects). Water (w) can be present in the structure both as zeolitic or

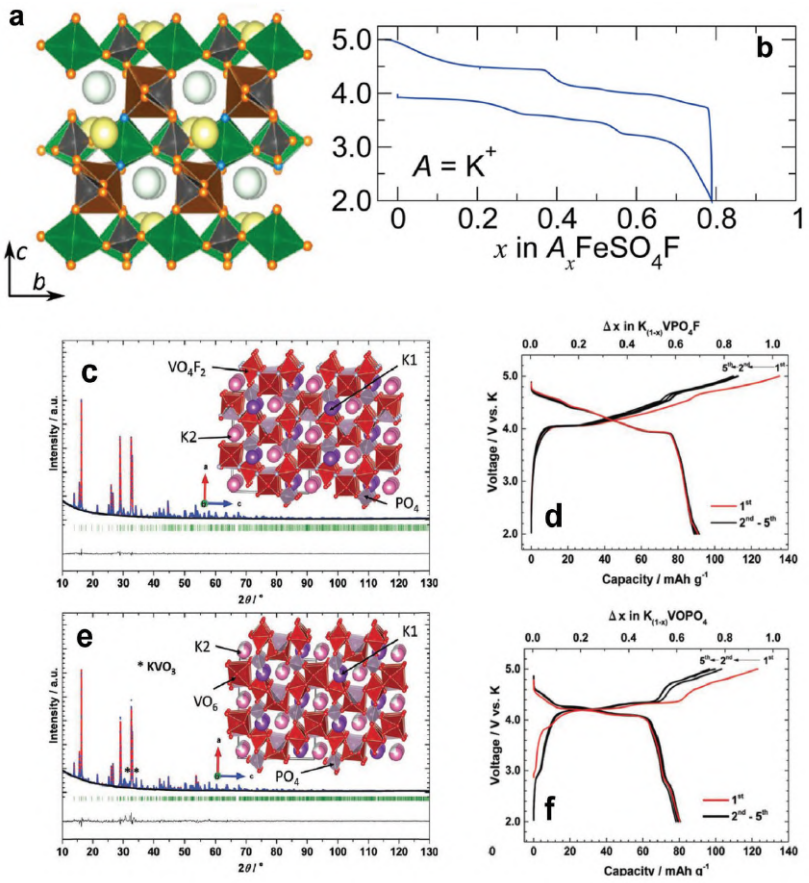

Figure 5.8: (a) Depiction of the $KFeSO_4F$ crystal structure and (b) its potassium storage ability at 0.05 C;[26] (c) XRD pattern of KVPO4F and (d) its electrode performance in the voltage range of 2–5 V range. (e) XRD pattern of KVOPO4 and f) its electrode performance in the voltage range of 2–5 V range.[27]

can be coordinated to metal ions in the vacancies site. This class of materials recently triggered renewed interest because of their unique properties: [28]

- if both the R and the P transition metals are electrochemically active (i.e. can change oxidation state in the analysed potential window), they can deliver high specific capacities when inserting alkali-metal ions;
- their geometry and unique nanoporous, openframework structure can ensure rapid ion conduction, i.e. can guarantee high rate capability;

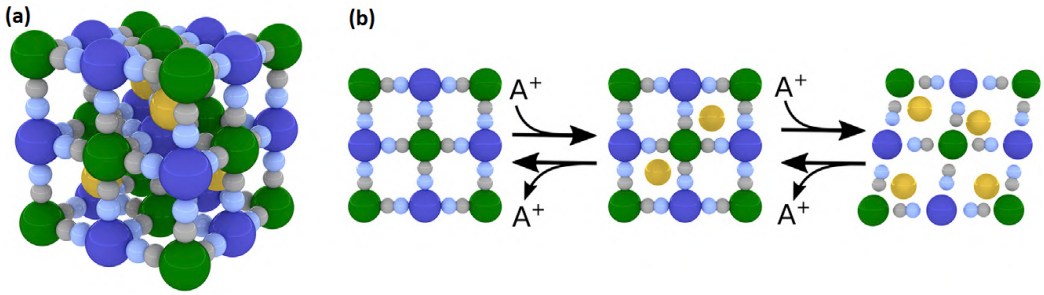

Figure 5.9: (a) Many Sodium, Lithium, and Potassium PBAs have face-centered cubic geometry, and open-framework lattice. Here the green and dark-blue atoms are transition-metal ions at the R site and P site, respectively. The yellow atoms are inserting ions. Gray atoms are carbon and light-blue atoms are nitrogen. (b) Alkali-metal ions insert into the subcubes of the lattice as the transition-metal ions change oxidation state. At high concentrations of lithium, sodium or potassium, the structure can distort to a less symmetric rhombohedral geometry.[28]

- they generally experience minimal structural changes during alkali metal ion de/insertion;
- they can be synthesized by simple co-precipitation in aqueous solution.

The major drawback of PBAs for energy storage applications is their low crystal density ($1.96 g{\cdot}cm^{-3}$ for defect-free sodium iron hexacyanoferrate), which is less than half of that of high-performing lithium-ion cathodes. The general electrochemical de/insertion of an alkali metal into a PBA is:

$$A_x P^J[R^K(CN)_6]_{y-1} w H_2O + A^+ + e^- \rightleftharpoons A_{x+1} P^J[R^{K-1}(CN)_6]_{1-y} w H_2O \tag{5.3}$$

The choice of the R transition metal, which typically is the center for the redox activity, determines the reaction potential. In addition, the R transition metal influences the R-C bond length, and it can strongly affect the lattice parameter and channel size, which in turn determines the ionic conductivity.[28] Nonetheless, the great majority of research on PBAs for secondary batteries focuses on hexacyanoferrates as positive electrodes because of the low cost and easy synthesis, as well as the high reaction potential ($\approx 1V$ vs SHE). On the other hand, the P site has enjoyed a much larger variety of element substitution in the pursuit of practical PBA active materials. The potential of the R site is greatly influenced by the P-site TM, with higher ionic potentials (ratio between the charge and the ionic radius) leading to higher insertion potentials. This effect can be understood by considering the greater polarization of the σ bond in the cyanide ligand, more significant π backbonding,

and lower t_{2g} orbitals of the R-site TM.[29] If the P site is red-ox active in the explored potential window, the full capacity of the PBA can be accessed, and two plateaus are observed.[30] However, these cathodes generally have lower cycle life, and if Manganese is utilized, it must be considered that Mn^{3+} is Jahn-Teller distorted. This effect may lead to deleterious geometric changes, which can significantly impact the cycle life.

Alkali, alkali-earth, and transition metals including lithium, sodium, potassium , rubidium, cesium, calcium, magnesium aluminum and zinc are known to insert into PBAs.[28] The alkali metals are the most commonly investigated inserting ions and they occupy the A site at the center of the lattice's subcube. It has been proved that the interting ion's radius determines the free energy of the insertion reaction and therefore influences the inserting potential. In copper hexacyanoferrate for example, the insertion potential follows the trend: $K^+ > Na^+ > Li^+$ (0.93, 0.80 and ≈0.7 vs SHE).[31]

Vacancies of the hexacyano metallate complex are the primary structural defects in prussian blue analogs (Figure 5.10). They have two main beneficial effects on the electrode performances. First, the vacancy mediated transport through the bulk can increase the ionic conductivity. Second, they have a stabilizing effect on the crystal structure; the Jahn-Teller distortion indeed occurs only below a minimum vacancy content.[32] The flip of the coin, is that vacancies reduce the available specific capacity of the material as they are positive defects and compete with potassium to ensure charge neutrality within the material. They also provide stable bonding environments for water within the structure. Water that cannot be removed from the material prior to operation severely impacts the electrochemical performance in non-aqueous electrolytes. The first report of K^+ insertion into PBAs in organic electrolyte, dates back to 2004, when Eftekhari reported the reversible insertion of potassium into a $K_2Fe[Fe(CN)_6]$ (KFeHCFe) thin film.[33] Ten years later the research on PBAs for KIBs underwent a renaissance and nowadays several PBAs candidates have been proposed.[34,35,36] Among them, the monoclinic potassium manganese hexacyanoferrate $K_2Mn[Fe(CN)_6$ (KMnHCFe) was reported to deliver high capacities (theoretical capacity $155 mAh{\cdot}g^{-1}$) with an average potential around 4 V vs K^+/K, and therefore represents the most promising cathodic material for KIBs (Figure 5.11a,b).[36,37] Bie et al. investigated the reaction mechanism occurring during the K^+ de/insertion and found reversible phase transitions (Figure 5.11c-d). During the first charge, the KMnHCFe undergoes two phase transitions from monoclinic to cubic and from cubic to tetragonal; during the following discharge the process reverts and the initial monoclinic geometry is restored via the cubic phase. Despite the reversible K^+ de/insertion, insufficient coulomic efficiencies (η_c) were reported. Only the use of fluoroethylene carbonate improved satisfacto-

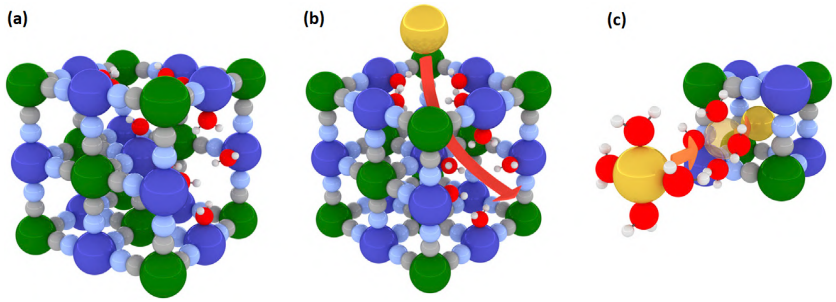

Figure 5.10: Defects and Water Affecting the Ion-Insertion Reaction: (a) two vacancies of the hexacyanometallate complex, including the R-site ion and its six cyanide ligands, are shown: one on the top face and one on the right-front face; (b) connected vacancies offer an alternative route for the conduction of ions through the structure; (c) an inserting ion sheds its hydration shell before entering the lattice.[28]

rily the η_c value.[36] This electrolyte additive is however not compatible with graphite, and therefore cannot be used for full cell applications.[37] As an alternative, Hosaka et al. reported the use of highly concentrated electrolyte solutions with improved performances, i.e. improved coulombic efficiency and sufficient capacity retention. Nonetheless, the η_c was still below 97%, and the the possibility of practical application for this class of electrolytes is still far from being proved.[38]

Bibliography

[1] C. Vaalma, D. Buchholz, M. Weil, and S. Passerini, "A cost and resource analysis of sodium-ion batteries," *Nat. Rev. Mater.*, vol. 3, p. 18013, 2018.

[2] T. A. Pham, K. E. Kweon, A. Samanta, V. Lordi, and J. E. Pask, "Solvation and Dynamics of Sodium and Potassium in Ethylene Carbonate from ab Initio Molecular Dynamics Simulations," *J. Phys. Chem. C*, vol. 121, no. 40, pp. 21913–21920, 2017.

[3] L. Zhang *et al.*, "Constructing the best symmetric full K-ion battery with the NASICON-type $K_3V_2(PO_4)_3$," *Nano Energy*, vol. 60, no. February, pp. 432–439, 2019.

[4] Y. Marcus, "Thermodynamic Functions of Transfer of Single Ions from Water to Nonaqueous and Mixed Solvents. PART 3: STANDARD POTENTIALS OF SELECTED ELECTRODES," *Pure Appl. Chem.*, vol. 57, no. 8, pp. 1129–1132, 1985.

[5] J. Y. Hwang, S. T. Myung, and Y. K. Sun, "Recent Progress in Rechargeable Potassium Batteries," *Adv. Funct. Mater.*, vol. 28, no. 43, pp. 1–45, 2018.

[6] A. Hérold, R. Setton, and N. Platzer, "Composés d'Insertion du Graphite, in Les Carbones," *A. Pacault Ed. Masson*, vol. 2, pp. 458–683, 1964.

[7] Z. Jian, W. Luo, and X. Ji, "Carbon Electrodes for K-Ion Batteries," *J. Am. Chem. Soc.*, vol. 137, no. 36, pp. 11566–11569, 2015.

[8] S. Komaba, T. Hasegawa, M. Dahbi, and K. Kubota, "Potassium intercalation into graphite to realize high-voltage/high-power potassium-ion batteries and potassium-ion capacitors," *Electrochem. commun.*, vol. 60, pp. 172–175, 2015.

[9] W. Luo *et al.*, "Potassium Ion Batteries with Graphitic Materials," *Nano Lett.*, vol. 15, no. 11, pp. 7671–7677, 2015.

[10] J. Liu *et al.*, "Unraveling the Potassium Storage Mechanism in Graphite Foam," *Adv. Energy Mater.*, vol. 1900579, pp. 1–11, 2019.

[11] L. Fan, R. Ma, Q. Zhang, X. Jia, and B. Lu, "Graphite Anode for a Potassium-Ion Battery with Unprecedented Performance," *Angew. Chemie - Int. Ed.*, vol. 410082, pp. 10500–10505, 2019.

[12] Z. Jian, Z. Xing, C. Bommier, Z. Li, and X. Ji, "Hard Carbon Microspheres: Potassium-Ion Anode Versus Sodium-Ion Anode," *Adv. Energy Mater.*, vol. 6, no. 3, pp. 1–5, 2016.

[13] G. Ma, K. Huang, J. S. Ma, Z. Ju, Z. Xing, and Q. C. Zhuang, "Phosphorus and oxygen dual-doped graphene as superior anode material for room-temperature potassium-ion batteries," *J. Mater. Chem. A*, vol. 5, no. 17, pp. 7854–7861, 2017.

[14] K. Share, A. P. Cohn, R. Carter, B. Rogers, and C. L. Pint, "Role of Nitrogen-Doped Graphene for Improved High-Capacity Potassium Ion Battery Anodes," *ACS Nano*, vol. 10, no. 10, pp. 9738–9744, 2016.

[15] H. Kim, J. C. Kim, M. Bianchini, D.-H. Seo, J. Rodriguez-Garcia, and G. Ceder, "Recent Progress and Perspective in Electrode Materials for K-Ion Batteries," *Adv. Energy Mater.*, vol. 1702384, p. 1702384, 2017.

[16] I. Sultana, T. Ramireddy, M. M. Rahman, Y. Chen, and A. M. Glushenkov, "Tin-based composite anodes for potassium-ion batteries," *Chem. Commun.*, vol. 52, no. 59,

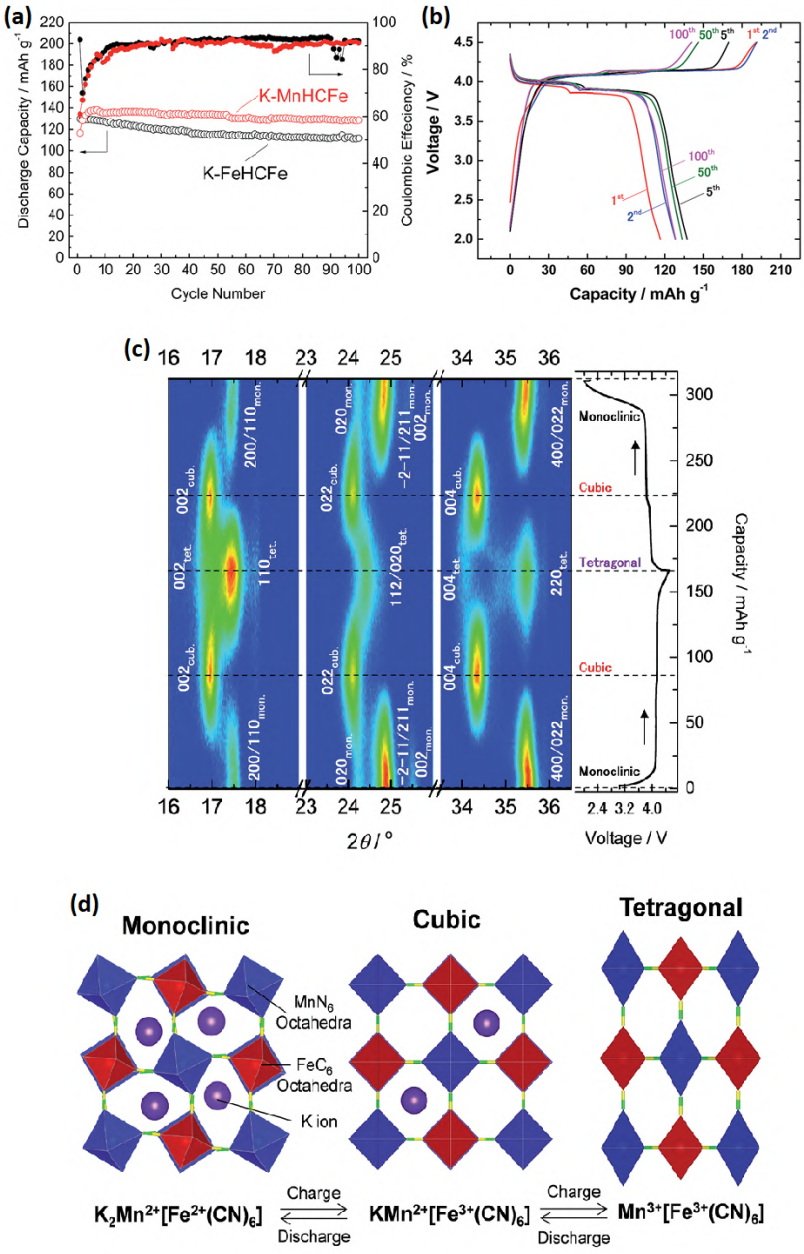

Figure 5.11: (a) KMnHCFe charge/discharge profiles and (b) Cycle performance of KMnHCFe and KFeHCFe in a K half-cell of at $30mA{\cdot}g^{-1}$ in the voltage range of 2.0–4.5 V. (c-d) Structural evolution of K-MnHCFe: (c) contour maps of operando XRD of K-MnHCFe during the first cycle showing major diffraction peaks which were indexed using monoclinic ($P2_1/n$), cubic ($Fm\bar{3}m$), and tetragonal ($I\bar{4}m2$) phases and (d) depiction of the crystal structures and phase transition observed by electrochemical potassium extraction and insertion.[37]

Chapter 6

Investigation of the conversion reaction on electro-spun Co_3O_4 as anode for Sodium-ion batteries

6.1 Introduction

Transition metals which undergo conversion reaction recently attracted increasing interest as negative active materials for sodium-ion secondary batteries. As described in chapters III and IV their electrochemical performances, and in particular the kinetics and reversibility of the reaction, can be strongly related to morphological aspects. In this study, cobalt oxide fibers were synthesized via electro-spinning followed by calcination in air at 600 ^{o}C. Texture, morphology and surface composition of the fibers, as well as the phase of the synthesized oxide were investigated by means of a combination of characterization techniques. The electrochemical performance of the electro-spun Co_3O_4 was evaluated as anode material in Na-ion rechargeable batteries, and the conversion reaction mechanism was investigated by means of ex-situ analyses on the cycled electrodes. The formation of the CoO after the first sodiation/desodiation cycle was reported, which may account for the cathodic specific capacity lowering from 983 down to $580 mAh \cdot g^{-1}$. The high aspect ratio morphology of the fibers is reported to be beneficial for high capacity and slow capacity fading (after 30 cycles, a de-sodiation capacity of $407 mAh \cdot g^{-1}$ is retained).

6.2 Background

A short summary of the technological background of SIBs, and in particular of conversion oxide anodes is here proposed. For a more exhaustive analysis the reader should refer to the Chapters III and Chapter IV.
First commercialized in 1990, lithium-ion batteries (LIBs) are widely applied in portable electronic devices and are presently considered as the most promising candidate to power next generation electric vehicles (EVs), hybrid electric vehicles (HEVs), plug-in hybrid electric vehicles (PHEVs), and stationary energy storage (SSI). The consequent growing consumption of lithium and its limited availability, restricted to few countries, represents a serious concern for the predicted market and manufacturing expansion of LIBs. Since sodium exhibits similar physical-chemical properties to lithium and its resources are better distributed, sodium-ion batteries can represent a sustainable, less expensive and environmentally-friendly alternative to LIBs. The development of the SIB technology however, requires the investigation of new electrode materials with reversible Na^+ uptake. Although graphite can reversibly intercalate lithium ions and is the material of choice for LIBs, the formation of sodium-intercalated compounds has been shown to be thermodynamically unstable.[1] On the other hand, hard carbons, are electrochemically active with sodium, but typically exhibit low first cycle coulombic efficiency. Moreover, their sodium uptake mechanism, still not fully understood, including the storage of sodium ions into confined micropores and structural defects and raised safety concerns related to the possible formation of sodium metal.[2] Different metal oxides with intercalation or conversion chemistry have been evaluated as anodes for rechargeable SIBs.[3,4]Conversion based transition metal oxides exhibit high reversible capacities. Among them, the spinel cobalt oxide (Co_3O_4) is attracting great attention thanks to its high theoretical specific capacity ($890 mAh \cdot g^{-1}$) and its relevant results for LIBs.[4,6,7] Unfortunately, as most of the conversion based anodes, Co_3O_4 suffers from low cycle life because of the large volume variation that occurs during the sodiation/desodiation process.[8] In recent years, various strategies have been reported to mitigate the problems arising from the electrode pulverization, which include decreasing the size of the oxide particles to the nanoscale and confining them in a carbonaceous matrix.[9] Recently, we demonstrated the great impact of the active material morphology on its electrochemical performance, showing that active material's high aspect ratio can facilitate the electrochemical processes resulting in enhanced electrode stability and capacity.[5] The crucial role of the material's porosity and morphology has been emphasised also by Yang et al.[10] In the present work Co_3O_4 fibers were synthesized via Electro-spinning (ES),

characterized by means of a combination of complementary techniques, and tested as anode material in SIBs. ES is a very simple, highly scalable and inexpensive technique for the growth of highly porous one-dimensional (1D) nanostructures.[11] The electrochemical behaviour of the fibers, as well as the reaction mechanism were here investigated.

6.3 Methods

6.3.1 Materials synthesis

Cobalt acetate ($CoAc_2$, $(CH_3COO)_2Co{\cdot}4H_2O$, purity: 99.99% trace metal basis, Sigma-Aldrich) was the cobalt oxide precursor. Polyacrylonitrile (PAN, $(C_3H_3N)_n$, purity: 99.9%, average molecular weight: 150,000 g/mol, Sigma Aldrich) and N,N-dimethylformamide (DMF, purity: 99.8%, Sigma-Aldrich) acted as polymer and solvent, respectively. All reactants were used as received. The spinnable solution was prepared by dissolving PAN (6.5 wt%) in DMF and stirred until a clear solution was obtained. Then, $CoAc_2$ (38.5 wt% relative to the polymer) was added, and the solution was kept under magnetic stirring for 4 hours. The as-prepared homogeneous solution was then electrospun using a CH-01 Electro-spinner 2.0 (Linari Engineering s.r.l.). The setup (Figure 7.1a) consists of a syringe equipped with a stainless steel needle, a grounded aluminum collector, and a high voltage power supply. During the spinning process the collector is continuously translated along the direction perpendicular to the syringe axis. The spinnable solution, fed at a constant rate by means of a pump that moves the syringe piston, is ejected under the high voltage applied between the syringe nozzle and the collector. In the present case, a 20 mL syringe, was equipped with a 40 mm long 0.8 mm gauge stainless steel needle. The solution was fed at a rate of $1.41 mL{\cdot}h^{-1}$. Applied voltage and distance between the tip of the syringe needle and the grounded aluminum collector were 15 kV and 11 cm, respectively. The spinning process was carried out in air environment (relative air humidity: 40%) at $20(\pm1)^oC$. DMF rapidly evaporates during the ES, owing to the strong jet elongation. After drying overnight at room temperature (RT), the nonwoven fibrous PAN/$CoAc_2$ membrane was peeled from the collector (Figure 6.1) and calcined in air for 2 hours at 600^oC to completely remove the PAN and produce the cobalt oxide from its precursor.

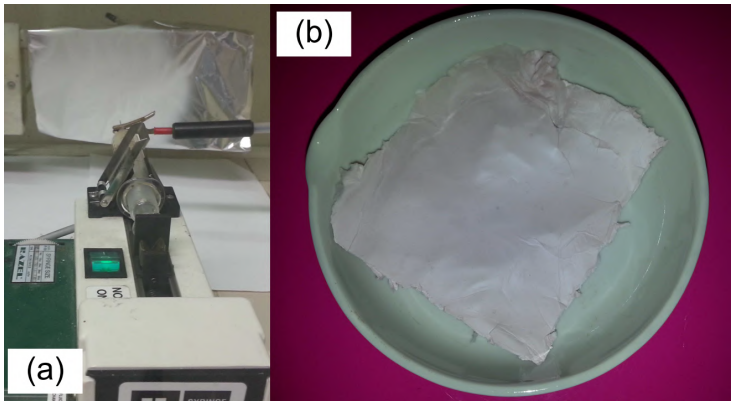

Figure 6.1: (a) Electrospinning setup; (b) As spoon membrane.

6.3.2 Sample characterization

The sample was analyzed by means of a combination of complementary techniques. Its texture and morphology were investigated by scanning electron microscopy (SEM) and high-resolution transmission electron microscopy (HRTEM). A Phenom Pro-X scanning electron microscope equipped with an energy-dispersive X-ray (EDX) spectrometer was employed for the SEM analysis. A fibermetric software allowed for automated accurate fiber diameter measurements from their SEM images. HRTEM micro-graphs were collected by a ZEISS LIBRA 200FE microscope operating at 200 KeV. The crystalline phase of the oxide was identified by means of X-ray diffraction (XRD) and micro-Raman spectroscopy (MRS). XRD patterns were recorded with a Bruker D2 Phaser diffractometer equipped with a Ni β-filtered Cu-Ka radiation ($\lambda = 0.1541$ nm). The JCPDS database of reference compounds was used for the diffraction-peak identification. Raman scattering was measured in air at RT using a confocal set-up and a NT-MDT NTEGRA-Spectra SPM spectrometer. The system was equipped with MS3504i 350 mm monochromator and ANDOR Idus CCD. A solid-state laser operating at 2.33 eV provided excitation. A Mitutoyo high numerical aperture 100x objective collected the scattered light from the sample. The use of a very low laser power (250 μWat the sample surface) prevented local heating of the samples and annealing effects. Surface composition of the sample and chemical environment of the component species were investigated by X-ray photoelectron spectroscopy (XPS). The spectra were acquired using a Surface Sciences Instruments M-Probe, equipped with a monochromatic Al-Kα source (1486.6 eV). The elemental concentrations were estimated from the areas under the photoelectron peaks weighed by the relative sensitivity factors. Identification and quantification of the surface species were carried out by decomposing the

high-resolution photoelectron spectra of core levels.

6.3.3 Electrochemical Tests

Electrodes for electrochemical measurements were prepared by mixing the as-prepared active material (electro-spun Co_3O_4) with a carbon matrix (Super P) and binder in a weight ratio of 75:17:8. Polyacrylic acid (average molecular weight: $\tilde{4}$50,000, SigmaAldrich) was used as a binder, and 1-methyl-2-pyrrolidinone (99%, ACS reagent, Aldrich) acted as dispersing solvent. The obtained slurry was film-casted onto a copper foil and dried in a vacuum oven at 80 ^{o}C until complete evaporation of the solvent. The film was thus roll-pressed, and 10 mm diameter disks to be used as electrodes in half-cells were punched out. The loading of active material ranged between 0.5 and $1 mg{\cdot}cm^{-2}$. Performances of the samples were evaluated in half-cell tests 2032 coin cells with sodium metal (99.9%, trace metal basis, Sigma-Aldrich) acting as a counter and reference electrode. Coin cells were assembled in a high-purity argon-filled glove box (Mbraun, [O_2] <1 ppm). A 1M $NaClO_4$ (>98%, ACS reagent, Sigma-Aldrich) in propylene carbonate (>99.9%, Merck) solution with 2 wt% fluoro-ethylene carbonate (FEC, 99%, Sigma Aldrich) was used as the electrolyte. A glass fiber disk was employed as the separator.

6.4 Results and Discussion

6.4.1 Properties of the electro-spun fibres

Figure 6.2 shows the results of the textural and morphological analysis on the as-spun and calcined fibers. The scanning electron microscopy reveals that the fibers, very long before calcination (Figure 6.2a), remarkably shortened after the thermal treatment (Figure 6.2b). The fibers became considerably thinner as an effect of the polymer removal, in agreement with what is reported in the literature and their length reduced to 2–4 μm..[12] Their average diameter decreased from 450 nm in the as-spun fibers (inset of Figure 6.2a) to 350 nm in the calcined ones (inset of Figure 6.2b). The heat treatment also induced textural changes, as the smooth surface of the fibers before calcination became rough after the thermal treatment. The surface roughness of the fibers is strictly correlated to their substructure and to the average size of the fiber-forming oxide nanoparticles.[12] TEM and HRTEM analyses reveal that the calcined fibers consist of dense crystalline agglomerates of ovoid and smoothed grains (Figure 6.2b-c), which fully accounts for the fiber roughness previously observed. The estimated crystallite size (dG) ranges

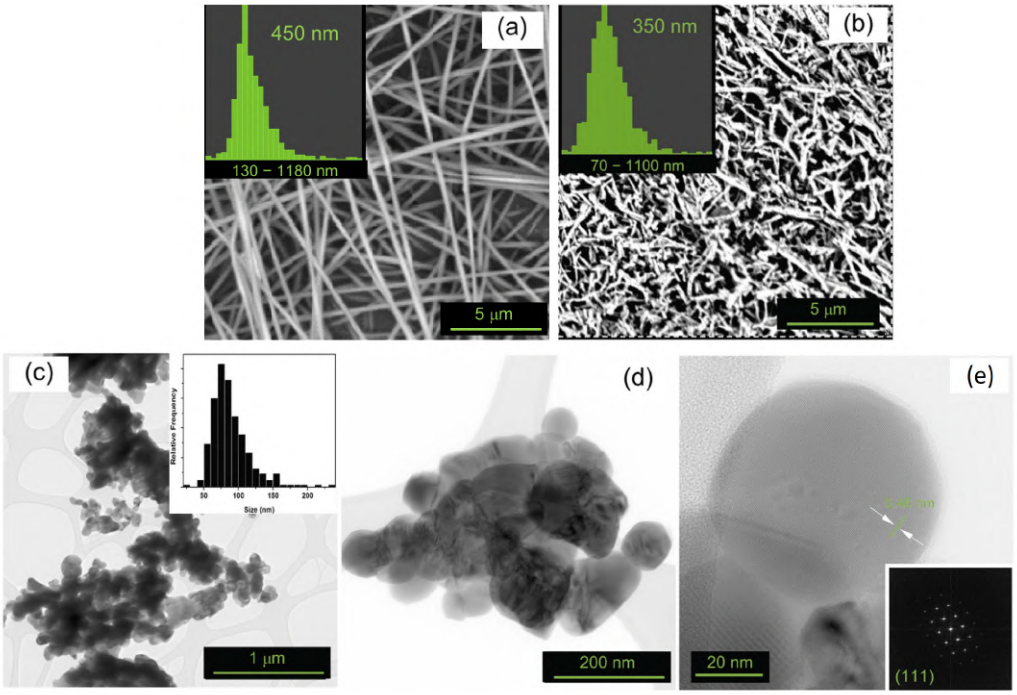

Figure 6.2: Morphology of the fibers as resulting from (a-b) SEM and (c–e) TEM and HRTEM analyses. (a) as spoon fiber and (b-e) calcined fiber. In image (d) the interspacing distance between (111) planes is indicated. Inset of image (a-b): fibre diameter distribution with peak value and diameter range. Inset of image (c): grain size distribution. Inset of image (e): FFT analysis indexed as the (111) plane of the Co_3O_4 spinel phase of the oxide.

between 30 and 230 nm and shows a tailed distribution centered around 83 nm (inset of Figure 6.2b,c). HRTEM (Figure 6.2d) and selected area electron diffraction (SAED) evidence the crystalline structure of the oxide. The inset of Figure 6.2e shows the reflections from the (111) lattice planes of Co_3O_4.

Figure 6.3a displays the XRD pattern of the sample, which reveals diffraction peaks at 18.9^o, 31.3^o, 36.9^o, 44.8^o, 59.4^o, 65.2^o, 38.5^o and 55.7^o associated with the reflections from (111), (220), (311), (222), (400), (422), (511), and (440) crystallographic planes of the face-centered cubic Co_3O_4 spinel phase (JCPDS card No. 431003), with Co^{2+} and Co^{3+} in the tetrahedral and octahedral sites, respectively. The absence of signals originating from other cobalt oxide phases or impurities demonstrates the high purity of the material synthesized. The average size of the oxide crystallites (dC), as estimated from the most prominent peak of the XRD pattern via the Scherrer's equation, is 35 nm. This value (<dG) is indicative of the polycrystalline nature of the

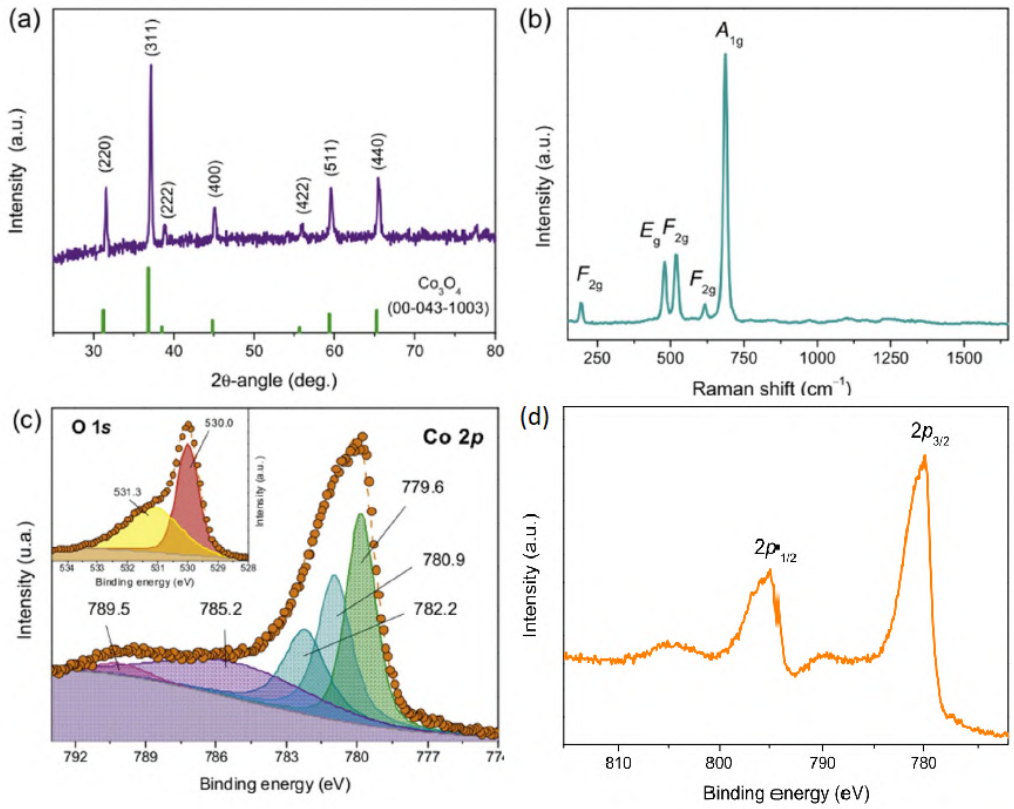

Figure 6.3: (a) XRD pattern, (b) Raman spectra, and (c) Decomposition of high-resolution photoelectron spectra of the Co 2p core level, and the O 1s core level (inset).

fiber forming oxide grains. The cubic phase of Co_3O_4 spinel belongs to the crystal space group O_h^7 ($Fd3m$). Normal modes predicted by the factor group analysis include five Raman-active vibrations ($A_{1g} + E_g + 3F2_g$).[13] Consistently, five peaks at 194, 480, 522, 617 and 687cm^{-1} are detected in the Raman spectrum of the sample (Figure 6.3b). The cobalt species present on the sample surface is investigated by high-resolution X-ray photoelectron spectroscopy (HRXPS). Cobalt oxides and hydroxides can be identified thanks to the different spectral profiles of their core level photoelectron spectra. Figure 6.3d shows the HRXPS spectrum of the Co 2p core level. The measured spectral profile is featured by two spin-orbit components (Co $2p_{3/2}$ at 779.9 eV, and Co $2p_1/2$ at 795.0 eV) with a spin-energy separation of 15.1 eV and no prominent shake-up satellite peak, as typical of the mixed-valence Co_3O_4 spinel phase of the oxide.[13] Since both the spin-orbit components qualitatively contain the same chemical information, only the higher-intensity Co

$2p_3/2$ peak is here considered. Following the references,[14] the peak is decomposed to three contributions located at 779.6, 780.9 and 782.2 eV (Figure 6.3c), whereas the shake-up satellite is decomposed to two contributions, at 785.2 and 789.5 eV, associated to the cobalt ions with 2+ and 3+ oxidation state, respectively. The high-resolution photoelectron spectrum of the O 1s core level (inset of Figure 6.3c) is featured by a sharp peak at 530.0 eV and a shoulder at higher binding energy. The former is associated to lattice oxide O_2–ions, while the latter (at 531.3 eV) originates from low-coordinated oxygen defects or vacancies.[15]

6.4.2 Electrochemical investigation

Figure 6.4a shows the galvanostatic charge/discharge profiles at 90 mA/g of the cobalt oxide fiber in half cells, in the potential range of 0.01–3.00 V ($vsNa+/Na$).

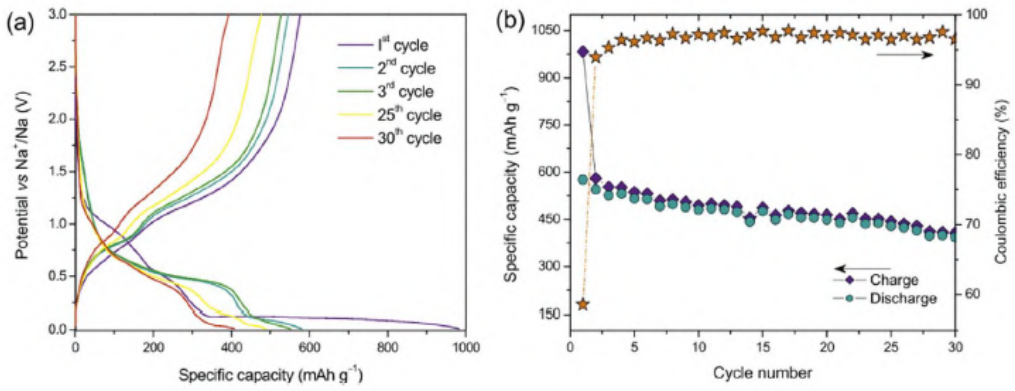

Figure 6.4: (a) Galvanostatic discharge/charge profiles at a current density of 90 mA/g, and (b) Effect of cycling on the specific capacity and related Coulombic efficiency.

The capacities are normalized over the mass of the active material alone. The initial sodiation and de-sodiation capacities are 983 and $576 mAh{\cdot}g^{-1}$, respectively, resulting in a Coulombic efficiency (CE, defined as the ratio of anodic charge and the cathodic charge) of 58.5%. These values are larger than those reported for mesoporous Co_3O_4 nanosheets (686 and $350 mAh{\cdot}g^{-1}$, corresponding to a CE of 51.0%) [23]. Also cobalt oxide slabs and flakes synthesized by hydrothermal route exhibit lower initial cathodic and anodic capacities (770 and $541 mAh{\cdot}g^{-1}$ for the former, and 789 and $561 mAh{\cdot}g^{-1}$ for the latter).[5] On the contrary, higher values of initial cathodic and anodic

capacities (1068 and 751$mAh{\cdot}g^{-1}$, respectively) were observed on cobalt oxide needle-like nanoparticles produced by the same method.[5] In the second and third cycle, the electro-spun fibers exhibit cathodic capacities of 578 and 552$mAh{\cdot}g^{-1}$, and anodic capacities of 544 and 526$mAh{\cdot}g^{-1}$, with improvement of CE (93.9% and 95.3%). During subsequent cycles, capacities values undergo a mild decrease (Figure 6.4b), as reported for other Co_3O_4-based anodes. After 30 cycles, the retained cathodic and anodic capacities are 407 and 393$mAh{\cdot}g^{-1}$, corresponding to a CE of $\tilde{9}7\%$. These capacities values are higher than those reported, after the same number of cycles, for cluster of Co_3O_4 nanoparticles (c.a. 250$mAh{\cdot}g^{-1}$),[16] and cobalt oxide slabs and flakes (below 300$mAh{\cdot}g^{-1}$).[5] However, they are slightly lower than those relative to cobalt oxide needles (c.a.450$mAh{\cdot}g^{-1}$), featured by a similar 1D-nanostructure morphology and higher aspect ratio. This find confirms the great impact of the active material morphology on its electrochemical properties pointed out by Longoni et al.[5] A high aspect ratio results in shorter diffusion lengths and limits deleterious effects of the volume changes related to the conversion mechanism.

6.4.3 Investigation on the mechanism

The initial sodiation is featured by a sloping curve in the 2.0–0.12 V potential range, a long flat plateau at 0.12 V and a short sloping tail below 0.12 V (Figure 6.4a). According to Wen et al. the sloping discharge curve at 2.0–0.12 V might be related to the decomposition of the electrolyte (SEI formation) and the initial formation of a solid solution ($Na_xCo_3O_4$), while the long plateau at 0.12 V mainly corresponds to the further reduction to Co and Na_2O.[3] It is widely recognized that the lithiation/delithiation process of Co_3O_3 occurs through the electrochemical reaction

$$Co_3O_4 + 8Li \rightleftharpoons 3Co + 4Li_2O \tag{6.1}$$

leading to a theoretical reversible specific capacity of 890$mAh{\cdot}g^{-1}$. The analogous electrochemical reaction for sodium is:

$$Co_3O_4 + 8Na \rightleftharpoons 3Co + 4Na_2O \tag{6.2}$$

However, lower reversible capacity values are generally obtained for Co_3O_4 in the case of SIBs. Rahman et al. proposed the occurrence of a partial conversion reaction as the possible reason.[16] Recently, Longoni et al. suggested that the formation of a reduced cobalt species (namely CoO, rather than spinel Co_3O_4) may account for the considerable difference observed between the first and the second sodiation profile and capacity.[5] According to the

authors, a two-step conversion process may take place, involving a first irreversible reaction leading to the formation of CoO as the stable intermediate with a lower theoretical specific capacity ($715 mAh \cdot g^{-1}$):

$$Co_3O_4 + 6Na \rightleftharpoons 3CoO + 2Co + 3Na_2O \tag{6.3}$$

followed by:

$$CoO + 2Na \rightleftharpoons Co + Na_2O \tag{6.4}$$

with the reduction of all cobalt species to metallic cobalt.

In order to shed light on the processes occurring in the cobalt oxide fiber

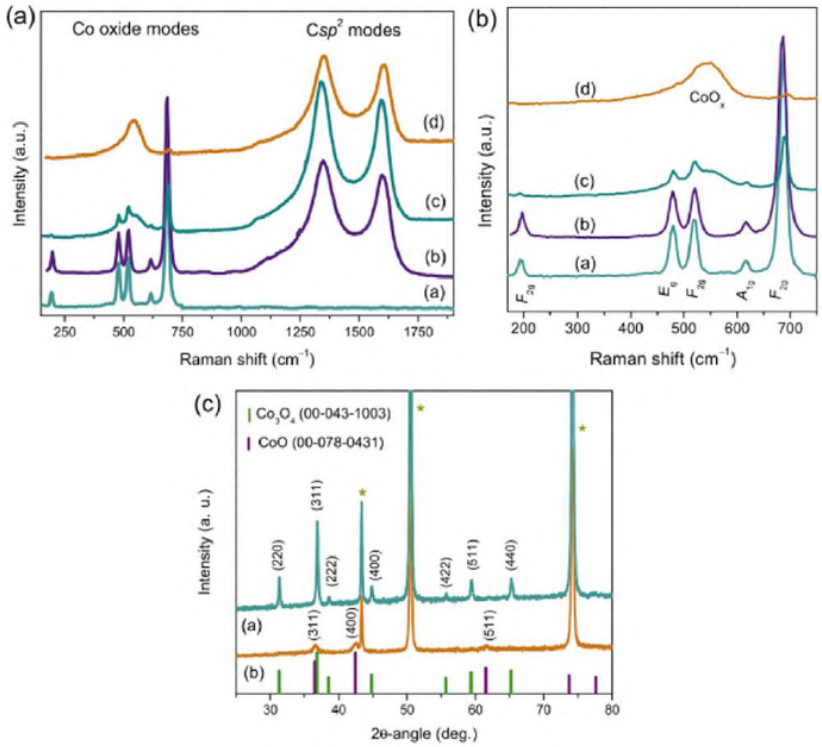

Figure 6.5: (a) Raman spectra of the electro-spun Co_3O_4 based anode before (curve b) and after cycling (curves c and d); the spectrum of the pristine fibers (curve a) is also reported for comparison. (b) Spectral region of the oxide modes. (c) XRD patterns of the electro-spun Co_3O_4 based anode before (diffractogram a) and after cycling (diffractogram b). Stars mark signals arising from the copper current collector

during the very first cycles, ex-situ Raman and XRD analyses were carried out. To evaluate the spatial homogeneity of the sample, Raman scattering was measured in several random positions; the pristine electrode was found to

be spatially homogeneous. Regardless of the region probed by the laser spot, the fingerprint of the Co3O4 oxide was clearly visible in the Raman spectrum of the pristine electrode (curve b in Figure 6.5a and b) together with the broad D- and G- bands originating from the carbon Super P additive.[17] After the first cycle, two important changes occurred in the low-frequency spectral region (Figure 6.5b). The modes of Co_3O_4, dramatically weakened in intensity, were still visible only in a few positions (curve c), but were superimposed to a broad band centered at c.a.$550cm^{-1}$ (curve d). Hence, after a sodiation/desodiation cycle, i) the sample resulted less spatially homogeneous and, more importantly, ii) the appearance of the band at c.a.$550cm^{-1}$ indicated the loss of long-range crystalline order and the formation of lower crystallinity CoO. The formation of the reduced form of cobalt oxide was confirmed by XRD analysis. In the diffraction pattern of the pristine electrode(a, Figure 6.5c) all the peaks could be indexed to the Co_3O_4 spinel phase of the oxide (JCPDS card No. 431003). After a full sodiation/desodiation cycle, the diffraction pattern changes substantially, and the new, broad and low intensity peaks were assigned to the CoO phase of the oxide (JCPDS card No. 78-0431). The apparent discrepancy between the results of ex-situ Raman and XRD analyses can be understood as follows. At the end of the first cycle, the conversion reaction from Co_3O_4 to CoO may not be complete; the very small residual amounts of oxide are detected thanks to the higher sensitivity of Raman spectroscopy. These findings demonstrate that Co_3O_4 is not fully restored after the first reduction/oxidation cycle. The formation of the lower valence state oxide may account for the difference in the galvanostatic discharge profile at the second cycle (Figure 6.4a) and the lower reversible capacity.

6.4.4 Conclusions

Electro-spun Co_3O_4 fibers were synthesized and their electrochemical performances were evaluated as anode material in Na-ion rechargeable batteries. The nanostructuring of the active material, obtained through a highly scalable technique, was found to be profoundly beneficial to the electrochemical performances, in full agreement with previous studies. High porosity and high aspect ratio of the fibers facilitate the electrochemical processes resulting in enhanced electrode stability with respect to the same oxide with different morphology. The formation of the CoO after the first sodiation/desodiation cycle, evidenced by ex-situ analyses on the cycled electrode, was suggested to account for the considerable difference observed between the first and the subsequent sodiation profiles.

Bibliography

[1] K. Nobuhara, H. Nakayama, M. Nose, S. Nakanishi, and H. Iba, "First-principles study of alkali metal-graphite intercalation compounds," *J. Power Sources*, vol. 243, pp. 585–587, 2013.

[2] B. Xiao, T. Rojo, and X. Li, "Hard Carbon as Sodium-Ion Battery Anodes: Progress and Challenges," *ChemSusChem*, vol. 12, no. 1, pp. 133–144, 2019.

[3] J. W. Wen *et al.*, "Li and Na storage behavior of bowl-like hollow Co_3O_4 microspheres as anode material for lithium-ion and sodium-ion batteries," *Electrochim. Acta*, vol. 132, pp. 193–199, 2014.

[4] K. C. Klavetter *et al.*, "Li- and Na-reduction products of meso-Co_3O_4 for high rate, stability cycling battery anode materias," *J. Mater. Chem. A*, vol. 2, pp. 14209–14221, 2014.

[5] G. Longoni, M. Fiore, J.H. Kim, D.K. Kim, C.M. Mari, R. Ruffo, "Co_3O_4 negative electrode material for rechargeable sodium ion batteries: An investigation of conversion reaction mechanism and morphology-performances correlations," *J. Power Sources*, vol. 332, pp. 42–50, 2016.

[6] P. Zhang, Z. P. Guo, Y. Huang, D. Jia, and H. K. Liu, "Synthesis of Co_3O_4 /Carbon composite nanowires and their electrochemical properties," *J. Power Sources*, vol. 196, no. 16, pp. 6987–6991, 2011.

[7] Y. Wang *et al.*, "Onion-like carbon matrix supported Co_3O_4 nanocomposites: A highly reversible anode material for lithium ion batteries with excellent cycling stability," *J. Mater. Chem. A*, vol. 1, no. 17, pp. 5212–5216, 2013.

[8] F. Klein, B. Jache, A. Bhide, and P. Adelhelm, "Conversion reactions for sodium-ion batteries," *Phys. Chem. Chem. Phys.*, vol. 15, no. 38, p. 15876, 2013.

[9] Y. Wang, C. Wang, Y. Wang, H. Liu, and Z. Huang, "Superior sodium-ion storage performance of Co_3O_4@nitrogen-doped carbon: Derived from a metal-organic framework," *J. Mater. Chem. A*, vol. 4, no. 15, pp. 5428–5435, 2016.

[10] J. Yang *et al.*, "Highly ordered dual porosity mesoporous cobalt oxide for sodium-ion batteries," *Adv. Mater. Interfaces*, vol. 3, pp. 1500464–1500470, 2016.

[11] W. E. Teo and S. Ramakrishna, "A review on electrospinning design and nanofibre assemblies," *Nanotechnology*, vol. 17, no. 14, 2006.

[12] S. Santangelo *et al.*, "Effect of calcium- and/or aluminum-incorporation on morphological, structural and photoluminescence properties of electro-spun zinc oxide fibers," *Mater. Res. Bull.*, vol. 92, pp. 9–18, 2017.

[13] V. Hadjiev, M. Iliev, and I. Vergilov, "The Raman spectra of Co_3O_4," *J. Phys. Chem. C*, vol. 21, pp. L199–L201, 1988.

[14] L. Tian, J. L. Zhu, L. Chen, B. An, Q. Q. Liu, and K. L. Huang, "Synthesis and characterization of α-cobalt hydroxide nanobelts," *J. Nanoparticle Res.*, vol. 13, no. 8, pp. 3483–3488, 2011.

[15] L. Zhang, W. He, X. Xiang, Y. Li, and F. Li, "Roughening of windmill-shaped spinel Co_3O_4 microcrystals grown on a flexible metal substrate by a facile surface treatment to enhance their performance in the oxidation of water," *RSC Adv.*, vol.

Chapter 7

Electrochemical characterization of highly abundant, low cost iron (III) oxide as anode material for sodium-ion rechargeable batteries

7.1 Introduction

The development of sodium ion batteries depends on the design of electrodes based on cheap and high abundant elements. Thanks to their high theoretical specific capacity, iron oxides are potentially good candidates for negative electrodes. However, they suffer from poor electronic transport properties and large volume change during sodiation/desodiation. Stable performance in hematite or magnetite based electrodes generally requires the use of Fe/C composites made by expensive carbon precursors such as graphene oxides or carbon nanotubes. The limits of iron (III) oxide can also be tackled using a different approach by combining the advantages of nanostructuring and doping with an aliovalent element. It is here presented the use of *Si-doped* Fe_2O_3 nanofibres obtained with an highly scalable process based on electrospinning. The silicon not only improves the transport properties, but also induces changes in the structure and morphology. The electrochemical results show that the as synthesized fibres deliver an anodic capacity of $350 mAh \cdot g^{-1}$ at the average potential of 1.5 V vs. Na^+/Na after 70 cycles, a result never

achieved for an iron oxide based electrode standard formulation.

7.2 Background

As extensively described in the literature, the research on SIBs produced many interesting results in terms of stability and capacity retention on electroactive materials to be used in the cathode.[3,4] A broad range of possible candidates were studied, which have been categorized into layered oxides, polyanion frameworks (including phosphates, pyrophospates, fluorosulfates, oxychlorides and sodium super-ionic-conductors), and organic compouds.[5] In particular, Na_xTMO_2 layered oxides ($0<x \leq 1$; TM: Fe,Cr,Co,Mn,Ni,V,Cu and their mixtures) whose interest has recently regained enthusiasm, represent interesting cathode materials for SIB thanks to their high capacities, appropriate operating potentials, as well as their simple and scalable synthesis.[6] Conversely, anode materials still represent a challenge because of their low specific capacity and poor capacity retention.[7] Switching from lithium towards sodium intrinsically introduces the disadvantage of the lower standard reduction potential of Na^+/Na redox couple..[8–12] Therefore, efforts have been made in extending the reversible capacity in order to reach comparable energy densities. Transition metal oxides, which undergo conversion reaction (such as Co_3O_4, Fe_2O_3, Fe_3O_4, SnO, SnO_2, MoS_2, CuO, MoO_2, NiO), can deliver high theoretical specific capacity (around 800-900$mAh{\cdot}g^{-1}$) and represent promising anode candidates in SIB.[14] Concerning their energy storage mechanism, the following reaction is generally accepted:

$$M_aO_b + 2bNa^+ + 2be^- \rightleftharpoons bNa^0 + aM^0 \tag{7.1}$$

During the reduction process, a volume variation between 150-250% relative to the initial state is expected, due to the formation of metallic M^0 species.[13] Worth to be noted, this value is much lower than the one registered for alloying materials. Therefore, compared to alloying materials, a rational design of conversion based electrode-active materials can be surpassingly advantageous in targeting volume changes. In the case of Co_3O_4 for example, reversible capacity retention improvements were reached decreasing the particle size and increasing their aspect-ratio.[15] Among conversion based materials, iron oxide, in its different crystalline phases, represents one of the most interesting candidate thanks to its simple and cost-effective synthesis, low toxicity, environmental benignity and high abundance of its precursors. When screening potential candidates for energy storage, these characteristics are critical aspects that need to be considered. Both hematite (α-Fe_2O_3) and magnetite (Fe_3O_4), theoretical specific capacity of 1007 and 926$mAh{\cdot}g^{-1}$ respectively,

have been investigated in literature. Komaba et al. first reported the insertion of sodium into nanocrystalline $\alpha - Fe_2O_3$ and Fe_3O_4 with a sodiation cut-off voltage relatively high ($\sim$ 1.5 V).[16] Later on, the conversion reaction of Fe_3O_4 with sodium was investigated lowering the cut-off down to 0.04 V, revealing a high specific capacity of $645 mAh \cdot g^{-1}$ at 0.06 C for the first discharge, but insufficient capacity retention.[17] The effect of material's porosity and nanostructuring on $\alpha - Fe_2O_3$ was then investigated by Rao et al.[18] Small nanoparticles (in the range of 20-30 nm), were synthesized via microwave assisted hydrothermal method and revealed a stable specific capacity of $300 mAh \cdot g^{-1}$ after 100 cycles at 0.1C. In order to tackle the large volume variation that occurs during cycling and results in electrode pulverization and poor electrical contact, one of the most successful approaches is to design and develop hybrid electrode materials with carbon.[19] The $\alpha - Fe_2O_3@C$ nanocomposite proposed by Zhang et al. revealed, for example, high sodium storage capability and impressive cyclability, retaining $740 mAh \cdot g^{-1}$ after 200 cycles at $200 mA \cdot g^{-1}$.[20] In another recent work, hierarchical hollow $Fe_2O_3@C$ hybrid nanostructure derived from a metal organic framework precursor reached a reversible capacity of $662 mAh \cdot g^{-1}$ after 200 cycles with 93.2% capacity retention.[21] Despite such improved performance, the synthesis of these materials often require expensive carbon precursors such as graphene oxide or carbon nanotubes and are hardly up-scalable, owing to not trivial multistep nature of the synthesis method. Easily up-scalable synthesis procedures for nanostructured iron oxides are required. Since oxides suffer from poor conductivity, the introduction of a sufficient amount of alio-valent impurities, acting as electronic substitutional dopants in their lattice, represents a viable route to increase of their conductive properties.[22] Herein, we present the synthesis and characterization of coral-like $\alpha - Fe_2O_3$ and silicon doped Fe_2O_3 mesoporous one-dimensional (1D) nanostructures, obtained via electrospinning (ES), a very simple and scalable preparation technique.[23] The as synthesized fibers are fully characterized to understand how the presence of the dopant influences the morphology, the crystalline phase and the electrochemical activity of the resulting oxide. The results show that silicon doping significantly modified the properties of iron oxide enhancing its electrochemical properties. Finally, the mechanism of the conversion reaction is analyzed in detail, and the importance of a sodium rich intermediate is pointed out.

7.3 Methods

7.3.1 Materials synthesis

Polyacrylonitrile (PAN, (C3H3N)n, purity: 99.9%, average molecular weight: 450000 g/mol1) and N,N-dimethylformamide (DMF, $HCON(CH_3)_2$, purity: 99.8%) were used as polymer and solvent, respectively. Iron(II) acetate ($FeAc_2$, $Fe(C_2H_3O_2)_2$, purity: 95%) and tetraethyl orthosilicate (TEOS, $Si(OC_2H_5)_4$, purity: 98%) act as the iron oxide precursor and the silicon source, respectively. All the reactants, supplied by Sigma Aldrich, were utilized as received, without any further purification. The spinnable solution was prepared by sol-gel method with the composition reported in Table7.3. PAN is dissolved in DMF and the mixture was stirred until a clear solution was obtained. $FeAc_2$ and TEOS were thus added, and the solution kept under magnetic stirring for 4 hours. The as-obtained homogeneous solution was then electrospun using a CH-01 Electro-spinner 2.0 (Linari Engineering s.r.l.). The apparatus, described in detail in the previous chapter, consists of a 20ml syringe equipped with a 40mm long 0.8 gauge stainless-steel needle, a grounded aluminium collector, and a high voltage (HV) power supply. The spinnable solution, fed at the constant rate $1.41mLh^{-}1$ by means of a pump, was ejected applying 15 kV over a collection distance of 11 cm. At the end of the process, non-woven membranes were obtained. The spinning process was carried out at $20(1)^oC$ (relative air humidity: 40%). During the spinning process, most of DMF rapidly evaporated owing to strong jet elongation. The residual solvent was removed by drying the as-spun membrane over night at room temperature. The membranes were finally peeled-off from the collector and calcined in air at 600^oC for 2 hours to eliminate the organic constituents of the fibres and to obtain solely the iron oxide from its precursor.

7.3.2 Structure and morphology characterization

The obtained fibers were analyzed by means of a combination of complementary techniques. A Phenom Pro-X scanning electron microscope was utilized for the SEM analysis. Fiber-metric software allowed for automated accurate fibre diameter measurements from their SEM images. In addition, dark field scanning transmission electron microscopy (STEM) was performed using Philips CM200 LaB6 microscope operating at 200 kV, equipped with an apparatus for elemental mapping. X-ray powder diffraction (XRPD) patterns were recorded with a Bruker D2 Phaser diffractometer equipped with a Ni β-filtered Cu- Kα radiation. The JCPDS database of reference compounds was used for diffraction-peak identification. Raman scattering was excited by

a thermo-cooled, solid-state laser operating at 532 nm (2.33 eV). The use of a very low laser power ($250\mu W$ the sample surface) prevented local heating of the samples and annealing effects. The spectra were recorded in air at room temperature using a NTEGRA-Spectra SPM from NT-MDT spectrometer, consisting of a 350 mm monochromator (MS3504i) and an ANDOR Idus CCD cooled at -60^oC. The scattered light from the sample was collected by means of a 100X (0.75 NA) Mitutoyo objective. Spectra acquired from different random positions on each specimen were averaged to have a reliable picture of the sample bulk.

7.3.3 Electrochemical Tests

Galvanostatic cycling with potential limitation (GCPL) and potentiostatic cycling with galvanostatic acceleration (PCGA) were carried out with the BioLogic VSP-300 multi-channel potentiostat-galvanostat on two-electrode coin cells CR2032 assembled in an argon filled glove box (MBraun), with sodium acting both as counter and reference electrode. Electrochemical impedance spectroscopy (EIS) analysis was conducted on a three electrode Swagelok configuration. The working electrodes for galvanostatic cycling were prepared mixing the as-prepared active material, the carbon matrix (Super P, MM Carbon) and the polymer binder (polyacrylic acid, PAA Mw $\sim$ 450000, Sigma Aldrich) in the weight ratio 6:3:1, respectively. Such high carbon content was employed according to the low conductivity of hematite reported in literature.[24] The carbon used in the preparation of the electrode was pre-treated at 800^oC in argon atmosphere in order to remove the adsorbed water and impurities, reducing the typical irreversibility that occurs during the first charge and discharge in such systems (Figure 7.1). The slurry obtained suspending the solid in N-Methyl-2-pyrrolidone (ACS Reagent, 99%) solvent, was casted onto a copper foil using doctor blade technique and subsequently dried until complete evaporation of the solvent at 80^oC under vacuum overnight. The working electrode was then roll-pressed and 16mm diameter disks were punched out. The load of active material was $1mg/cm^2$. Electrodes for EIS and PCGA were prepared following the same procedure but without the use of the carbon additive. The electrolyte was a solution of 1M $NaClO_4$ (ACS Aldrich) with 2% in weight of fluoroethylene carbonate additive (98%) in anhydrous propylene carbonate (>99.9%, Sigma). GCPL and PCGA were performed between 0.01 V and 3.00 V vs Na/Na^+. For the latter technique, it was used a voltage step of 5mV and 15 μA as low limiting current (C/100). EIS spectra were obtained at equilibrium condition using an AC potential signal of 10 mV in the frequency range from $50{\cdot}10^{-3}$ to $50{\cdot}10^3$ Hz.

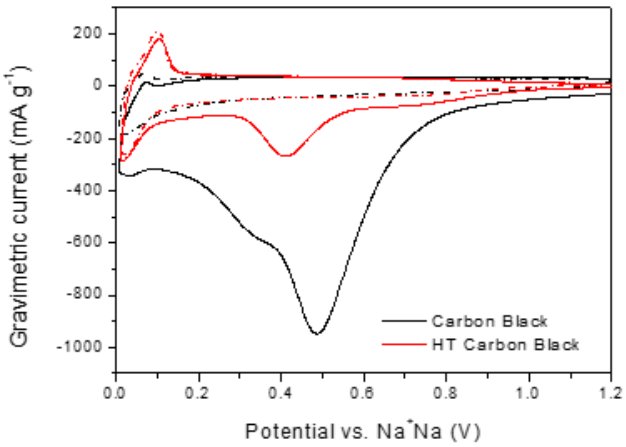

Figure 7.1: Cyclic voltammetry of the pristine and heat-treated (HT) carbon black between at a scan rate 0.1mV/s. The dashed lines represent the second cycle.

7.4 Results and Discussion

7.4.1 Synthesis and characterization of the fibers

The simple procedure for the synthesis of the fibers is schematically summarized in Figure 7.2. Briefly, the spinnable solution is prepared by dispersing the precursor of iron oxide ($FeAc_2$) and the silicon salt (TEOS) in a mixture of PAN and DMF. The homogeneous solution is then electrospun applying a high voltage between the needle and the aluminum foil. Finally, the as obtained fibrous film is heat-treated to remove the organic constituents and to generate the iron oxide from its precursor. Pure iron oxide fibers were synthesized for comparison, following the same procedure without the addition of the silicon salt. Details about the synthetic procedure are reported in Table 7.3.

Figure 7.4 shows the morphology of the pure-oxide fibers after calcination. The SEM analysis (Figure 7.4a) reveals fibers $3-5\mu m$ long with a diameter centered at 230 nm. The surface of the fibers, very smooth before calcination, becomes rough and highly porous after the thermal treatment. As reported in literature, the surface roughness of the fibers is strictly correlated to their substructure and to the average size of the fiber-forming oxide nanoparticles.[22] STEM images (Figure 7.4b), similarly to what reported in literature using the same synthesis technique, highlight a hollow structure of the fiber which consist of interconnected smooth nanograins with an average

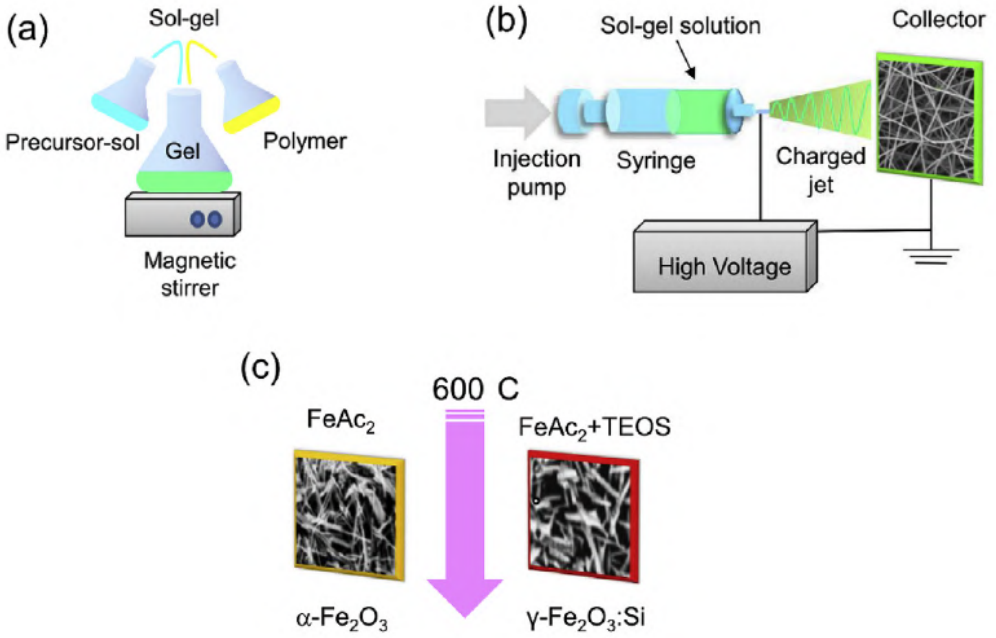

Figure 7.2: Schematic description of the experimental three-step procedure followed to synthesize the fibres: (a) preparation of the spinnable solution by sol-gel method, (b) electrospinning, (c) calcination of the as-spun non-woven fibrous film after peeling from the collector

size (dG) of 65 nm. It has been suggested that the strong interaction established between polymer chains and metal oxide precursor is responsible for this architecture,[25] which gives the fibers a coral-like aspect. The crystalline phase of the oxide was identified via XRPD and micro-Raman spectroscopy (Figure 7.4c, and d). All reflections of the diffraction pattern can be indexed to the rhombohedral $\alpha - Fe_2O_3$ phase (JCPDS card No. 33-0664) and no other iron oxide phases, such as FeO or Fe_3O_4, were detected. The average size of hematite crystallites, as estimated from the most prominent peak of the XRPD pattern via the Scherrer's equation, is 20 nm. This value is indicative of the polycrystalline nature of the fibre-forming oxide grains. The micro-Raman further confirmed the presence of only hematite, which belongs D^3_{d6} to space group, and revealed the expected seven Raman-active vibrations ($2A_{1g} + 5E_g$). Besides the typical phonon modes (below $620cm^{-1}$), a very intense asymmetric feature peaking at $1315cm^{-1}$ as well as a weak feature at $660cm^{-1}$ are detected. The former band is ascribed to two-phonon scattering or two-magnon scattering,[26] while the latter, typical of nanocrystalline hematite, originates from the presence of surface defects and/or reduced grain

Electrode Material	Precursors	Iron to dopant ratio	Composition of the spinnable solution				Collector
			Fe (wt%)	Si (wt%)	PAN (wt%)	DMF (wt%)	
α-Fe_2O_3	$FeAc_2$	-	2,5	-	6,5	91	Al foil
Si doped Fe_2O_3	$FeAc_2$ +TEOS	9	2,25	0,25	6,5	91	Al foil

Figure 7.3: Composition of the Spinnable Solution utilized for the synthesis of the fibers

size which, relaxing selection rules, renders Raman active the IR-active E_u mode.[27] The addition of the silicon salt to the spinnable solution results in a different phase and morphology of the fiber as shown in Figure 7.5. Smoother, thicker and shorter fibers are obtained as highlighted by the SEM spectroscopy.

Their diameter varies in the range $70 - 1230nm$, and their distribution is centered at a larger value compared to the non-doped sample (330 nm vs 230 nm). STEM micrographs (Figure 7.5b and Figure7.6b) show a composite fibrous architecture consisting of elongated nanostructures developing mainly along the longitudinal axis. The elemental mapping via STEM-EDX (Figure 7.6) reveals that Fe, O and Si are homogeneously distributed within the fiber. No segregation in secondary silicon-rich phases is detected. The Si/Fe ratio, as estimated from the semi-quantitative EDX measurements, is found to be 1:5. Despite the low signal intensity, the XRPD analysis reveals the formation of maghemite ($\alpha - Fe_2O_3$, JCPDS card No. 39-1346) as dominant phase, with a minor amount of $\alpha - Fe_2O_3$ as secondary phase (Figure 7.5c). Selected area electron diffraction analysis confirms the formation of crystalline maghemite ($\gamma - Fe_2O_3$). The average size of crystallites is 15 nm, smaller than in the hematite fibers. Maghemite is an iron-deficient form of magnetite (Fe_3O_4),[28] with structural formula Fe^{3+}_{3-x}, vO^{-2}_4, where v, represents an iron vacancy in an octahedral site. If the vacancies in the maghemite are randomly distributed, its structure exhibits spinel symmetry, with iron cations occupying both tetrahedral (t) and octahedral (o) sites in the lattice, namely $(Fe^{3+})_t\ [Fe^{3+}_{5/3}, v_{1/3}]_o$.[29] Differently from $\alpha - Fe_2O_3$, the Raman spectrum of $\gamma - Fe_2O_3$ is characterized by broad structures (Figure 7.5d),[29] whose Raman shifts are known to vary with preparation method, the resulting crystallinity degree, and the distribution of vacancies within the $\gamma - Fe_2O_3$ unit cell.[30] In the electrospun Si-doped fibres, three Raman bands corresponding to the T_{1g}, E_g and A_{1g} phonon modes are detected at 360, 510, $705cm^{-1}$ together with three narrower bands, associated with the most intense phonon modes of the secondary $\alpha - Fe_2O_3$ phase. In the

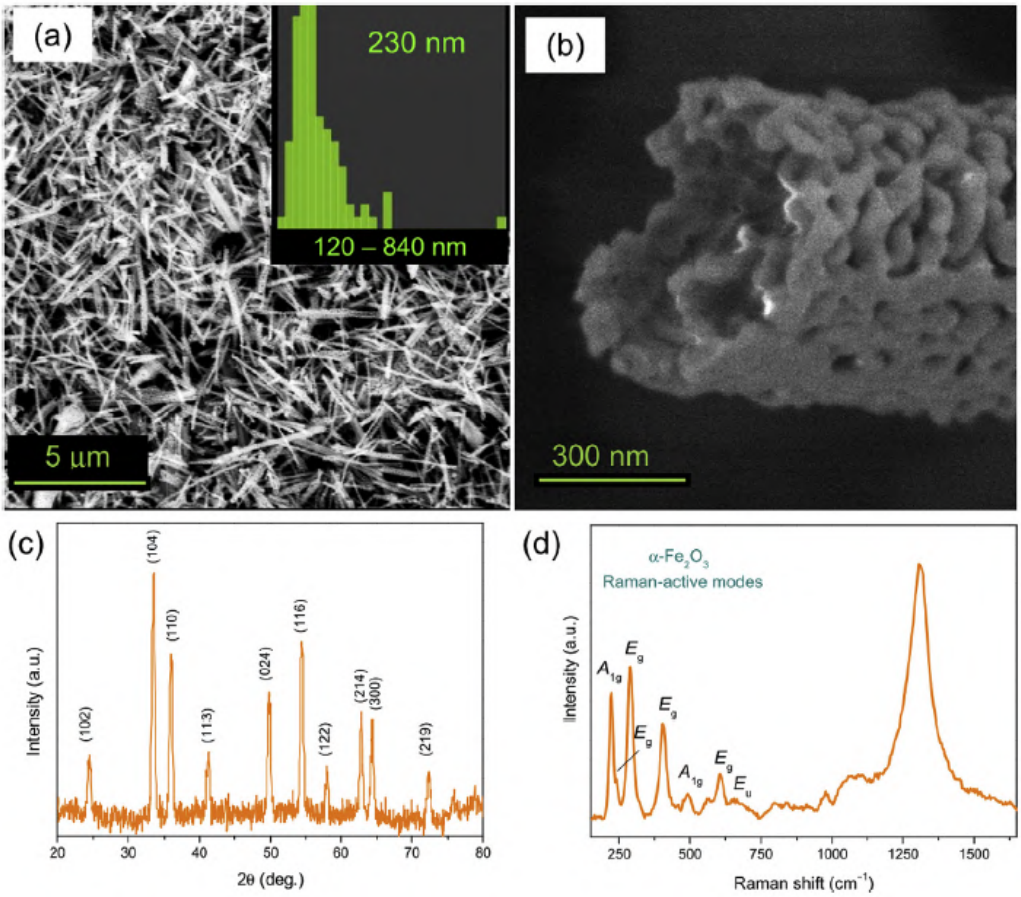

Figure 7.4: (a-b) Morphology of the non-doped fibers; (a) SEM and (b) STEM. Inset (a): Fiber diameter distribution and average diameter, as calculated by the image analysis software. (c) XRPD pattern, and (d) Micro-Raman spectrum of the fibers.

higher frequency region of the spectrum, the very intense asymmetric feature peculiar to hematite at $1315cm^{-1}$ overlaps with the maghemite magnon-modes,[31] observed around 1410 and $1580cm^{-1}$. The considerable width of the bands confirms the rather poor degree of crystallinity of the fiber-forming maghemite nanostructures suggested by the XRPD pattern.

The incorporation of silicon within Fe_2O_3 lattice does not introduce evident changes in the photoelectron spectrum of the Fe 2p core level (Figure7.7), as reported in the case of hematite films doped with alio-valent elements.[32] The Fe $2p_{3/2}$ spin orbit component and its satellite located respectively at 710.6 eV and 718.6 eV both in the un-doped and doped samples, are peculiar of Fe^{3+} cations.[33] The binding energy (BE) position of the Si 2p peak in

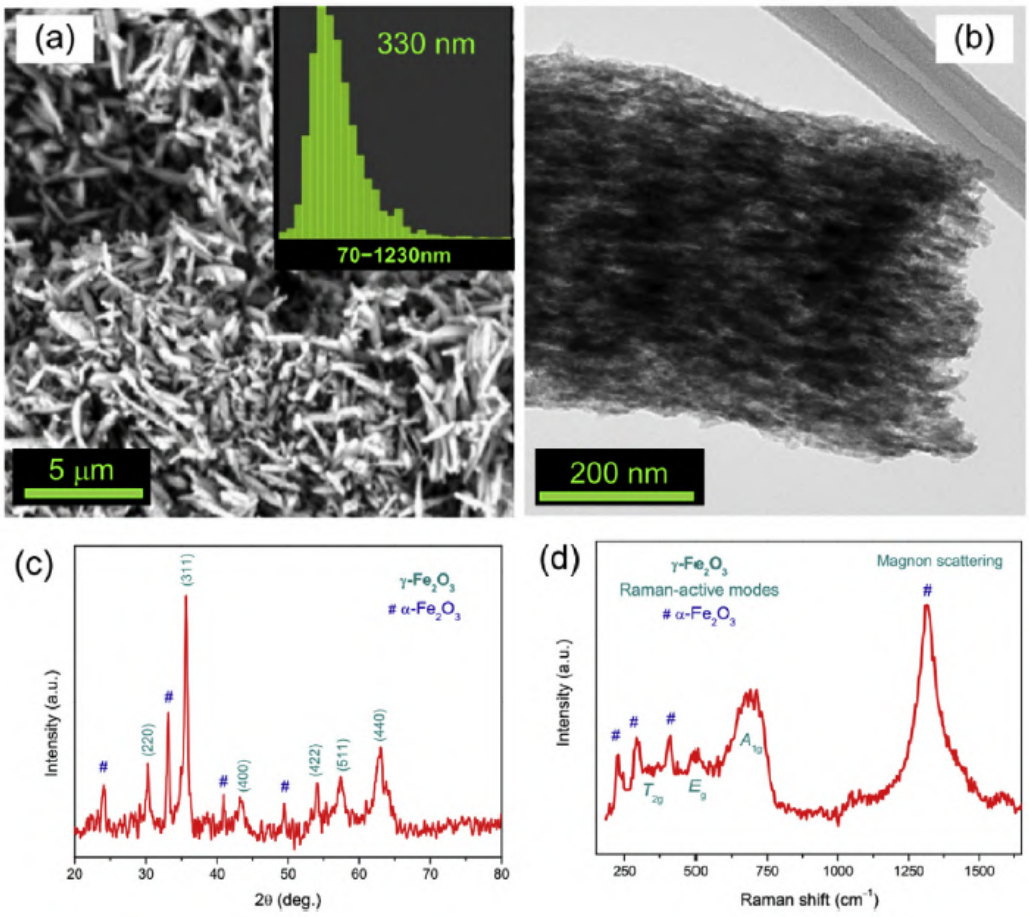

Figure 7.5: (a-b) Morphology of the silicon-doped fibers as resulting from (a) SEM and (b) STEM analyses. Inset in the image (a): Diameter distribution and average, as automatically calculated by the image analysis software. (c) XRPD pattern, and (d) Micro-Raman spectrum of the fibers.

the Si-doped sample allows ruling out the presence of elemental silicon in the iron oxide lattice. Indeed, elemental silicon Si $2p$ peak is located at $99.4eV$, whereas, in silicon with +1, +2, +3 or +4 oxidation states, the peak shifts at higher BE (100.4, 101.4, 102.5, and 103.6 eV, respectively).[34] Zhang et al. reported the substitutional doping of hematite with Ta^{5+} ion.[35] They pointed out that in Ta-doped hematite, the two peaks of the spin-orbit doublet of Ta $4f$ are located at lower BE with respect to Ta_2O_5 oxide. Therefore, in the present case, it can be concluded that Si ions, possibly in +4 oxidation state, are incorporated in the Fe^{3+} site of the oxide lattice. The reason for the formation, in the presence of the dopant, of a different crystallographic phase and smaller crystallites (15 nm against 20 nm in the pure oxide fibers,

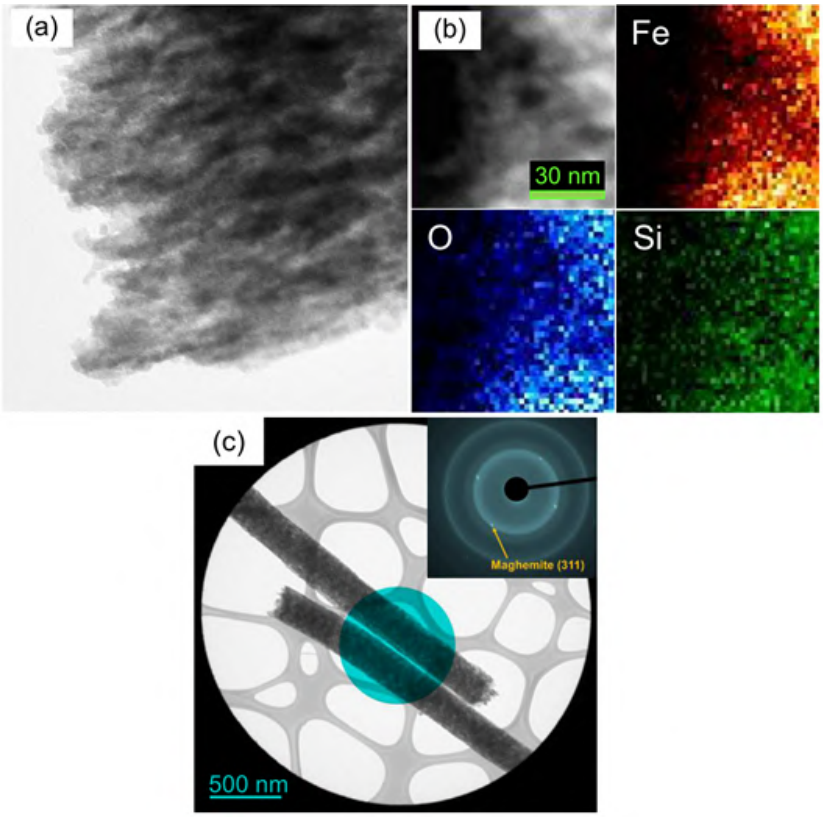

Figure 7.6: Results of (a) TEM, (b) STEM-EDX and (c) SAED analyses on the Si-doped fibers.

as estimated by XRPD) is not completely clear. At room temperature and 1atm conditions, maghemite and magnetite are thermodynamically less stable than hematite.[36] However, it has been found that for smaller nanocrystals the stability of maghemite increases. This can be inferred because its surface energy is lower than that of hematite.[37] Indeed, size-driven phase transition from $\alpha - Fe_2O_3$ to $\gamma - Fe_2O_3$ has been reported to occur upon mechanical grinding,[38] suggesting that the formation of nano-sized oxide crystals might play a role. Crystalline powders of Si-doped hematite have been already reported using 5% of silicon precursor at higher sintering temperature (1350^oC).[39] A progressive amorphisation of hematite with increasing the Si concentration has already been observed in nanostructures produced via reactive DC magnetron sputtering using alloyed sputtering targets. It has been suggested that the Si reduces the mobility of the Fe atoms during growth, which might restrict the formation of large crystallites.[40]On the contrary, by utilising the same precursor (TEOS) as in the present study,

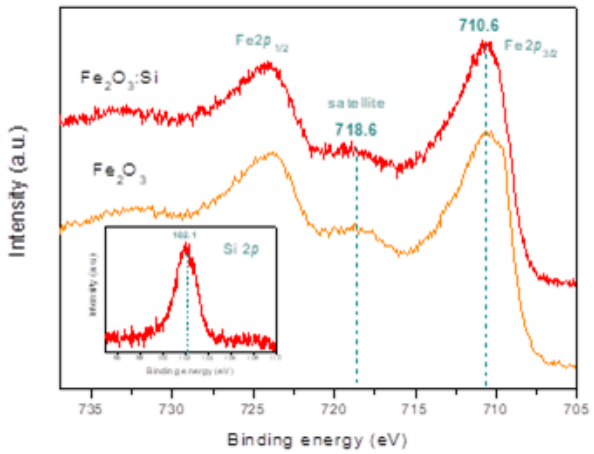

Figure 7.7: Photoelectron spectra of the Fe 2p core level in undoped and doped samples. Inset: photoelectron spectrum of the Si 2p core level.

Si-doped $\alpha - Fe_2O_3$ has been obtained by atmospheric pressure chemical vapor deposition.[41]

7.4.2 Electrochemical results

The results of the $\alpha - Fe_2O_3$ and Si-doped Fe_2O_3 based electrodes, cycled at different rates in sodium half-cell are presented in Figure 7.8. The results show a rather low specific capacity for the former. During the first de-sodiation of the hematite fibre, which corresponds to the first anodic sweep of the half-cell, at C/20, $130 mAh \cdot g^{-1}$ are obtained and a first cycle Coulombic efficiency (CE) of 37% is observed. Such low CE is common for nanostructured-conversion type of materials.[13] The low reversibility in the first cycle generally attributed to the solid electrolyte interface formation (SEI) on both the surface of the hematite and carbon black, which is here present in a non-negligible amount and has in turn a high specific surface area ($62 \pm 5 m^2 g^{-1}$). The results of the cell cycling at increasing higher currents (corresponding to C/10, C/5, C/2, 1C, 2C) highlight the sluggish kinetic of the hematite fibers. When the current is set back to C/20 (61^{st} cycle), the capacity is restored back to $110 mAh \cdot g^{-1}$. The capacity retention measured at this point after 60 cycles is 83%. Worth to be mentioned, in the final cycles registered at C/20, the capacity slightly increases as previously reported for nanosized $\alpha - Fe_2O_3$ in lithium ion batteries.[41] The corresponding charge/discharge profiles are reported in Figure 7.8b. The Si-doped Fe_2O_3

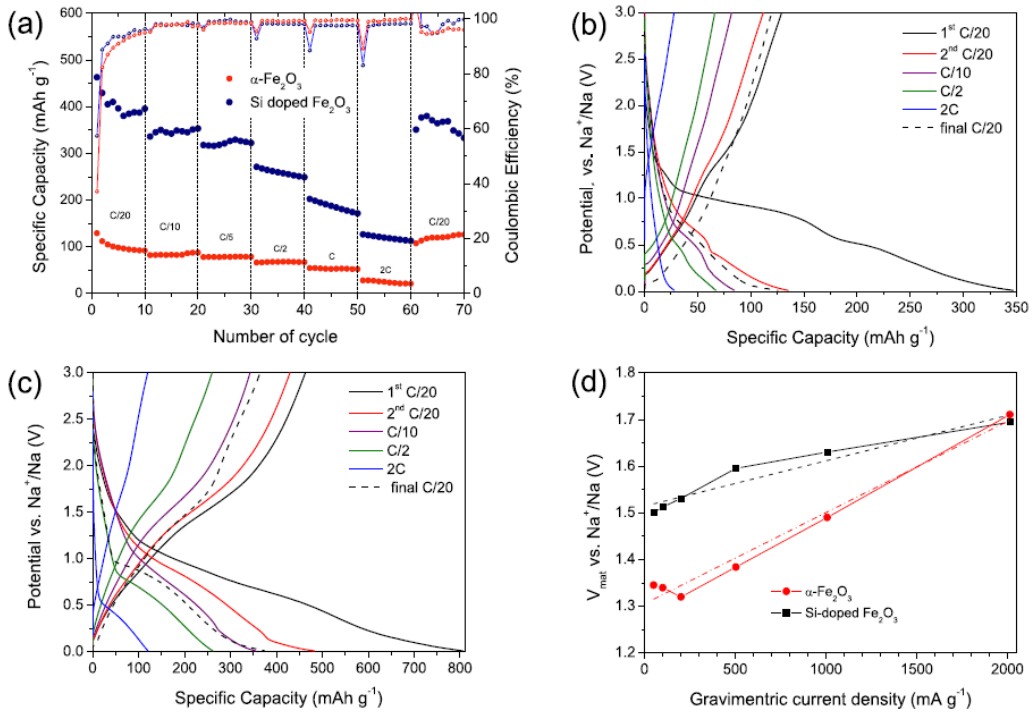

Figure 7.8: Results of the rate capability test for both hematite and Si-doped fibre: (a) Specific capacity versus number of cycles at different rates during the oxidative process; (b) Potential profiles versus specific capacity for the $\alpha - Fe_2O_3$ fibre; (c) Potential profile versus the specific capacity for the Si-doped Fe_2O_3; (d) Material average potential (Vmat) of the anodic scan for both the electrodes calculated versus the gravimetric current.

rate tests set a noticeable increase in the delivered specific capacity. Since the material was designed to work as negative electrode in a full battery, the following discussion will be mainly focused on the anodic (de-sodiation) scans. In the first 10 cycles, the average specific capacity achieved by the doped fiber ($400 mAh \cdot g^{-1}$) is four times higher than the one achieved by the $\alpha - Fe_2O_3$ (c.a. $100 mAh \cdot g^{-1}$). Moreover, at C/2 (corresponding to an applied current density of $500 mAg^{-1}$), it still delivers $265 mAh \cdot g^{-1}$, and even at extremely high rates, such as 2C (c.a. $2 A \cdot g^{-1}$), the system delivers $129 mAh \cdot g^{-1}$ suggesting improved kinetic capabilities in withstanding fast charge transfer and phase modification. After a first cycle with low Coulombic efficiency (57%), the specific capacity achieved cycling at the same current appears to be stable, revealing a good material's stability and process reversibility. After the high rate test, the current is set back to the lowest value (C/20), and the electrode recovers $350 mAh \cdot g^{-1}$ revealing a capacity retention of 87% after 60

cycles. Charge/discharge profiles (Figure 7.8c) show a two-step redox process similar to the one of the bare $\alpha - Fe_2O_3$ electrode.

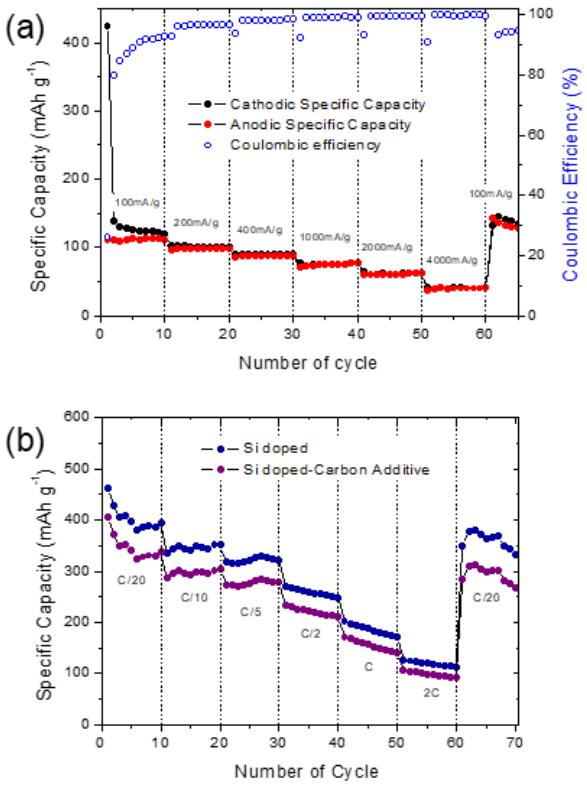

Figure 7.9: (a) Rate capability test of the thermal treated carbon black. (b) Comparison between the capacity obtained for the Si doped Fe2O3 electrode and the capacity obtained subtracting the contribution of the carbon additive.

To avoid misinterpreting the results, the conductive carbon added in the preparation of the electrode (30% wt.), must be considered, as it is non-inert in sodium cells. Excluding any synergistic effect and using the results obtained cycling the carbon additive alone (Figure 7.9a) to subtract the contribution of the carbon additive, the capacity delivered by the Si-doped fibre alone is between 80 and 90% of the total capacity (Figure 7.9b) We can thus conclude that, despite the carbon contribution is non-negligible, the specific capacity registered is mainly ascribable to the iron oxide active material. Since no intimate carbon composite has been used (graphene oxide, carbon nanotubes, etc.) and the only carbon source (low cost Super P) present in the electrode has been mechanically mixed in the slurry formulation, the good

capacity retention and high rate capability can be specifically correlated to the specific morphological features of the synthesized nanofibers. The importance of the electrode average (either anodic and cathodic) potentials is often ignored, although the real energy density that can be extracted during the discharge of a full cell (i.e. using one of the cathodic materials proposed in literature) strongly depends on the average potential values of single materials. In order to avoid any ambiguous definition, we report here the material average potential V_{mat} (it can be either anodic or cathodic) calculated by dividing the energy density measured in the half cell (E_{hc}) by its capacity

$$V_{mat}(V) = E_{hc}(Wh)/C_{hc}(Ah) \tag{7.2}$$

Since the two-electrode half cells are usually assembled using a large amount of sacrificial reference material (sodium or lithium foils), whose overpotential can be considered negligible at moderate current density (in the range of 5-50 mV), the so-defined average potential can be solely attributed to material properties and is a function of the applied current. Focusing the attention on the anodic process, the material average potential is generally higher for the silicon-doped phase 7.8d compared to $\alpha - Fe_2O_3$. This difference is mainly due to the different electronic structure of the considered phases and not to dissimilar reaction mechanism since the de-sodiation profiles are comparable. However, the hematite average potential, and therefore the electrode overpotential, rapidly grows as the current is raised, while for the silicon-doped fibers electrode remains nearly un-changed. This result further points out the better kinetic properties of the Si-doped Fe_2O_3. To have a better understanding the electrochemical processes occurring during the sodiation and de-sodiation process, PCGA analysis and EIS were performed on the electrodes prepared with the active material and binder alone, i.e. without the carbon additive. The presence of this additive, indeed, could interfere with the iron oxide signals in both potential profiles and impedance spectra even if its contribution to the capacity is quite low. PGCA analysis implies cycling the electrode in near-equilibrium conditions, reaching the maximum capacity that the material alone can provide.[42] Each occurring Faradaic process is thus decoupled and visualized through a differential capacity data plot, as previously reported in literature.[43]

Figure 7.10 reports the results of the PCGA analysis for both the undoped and the doped fibres electrode. We can observe a huge increase in the capacity for the pure hematite fibers compared to the results reported in Figure 7.8, and the first reduction potential profile shows a long flat plateau centred at 0.025 V, which suggests a two phase reaction typical of conversion reaction. Besides the first sodiation, the capacity registered for the hematite

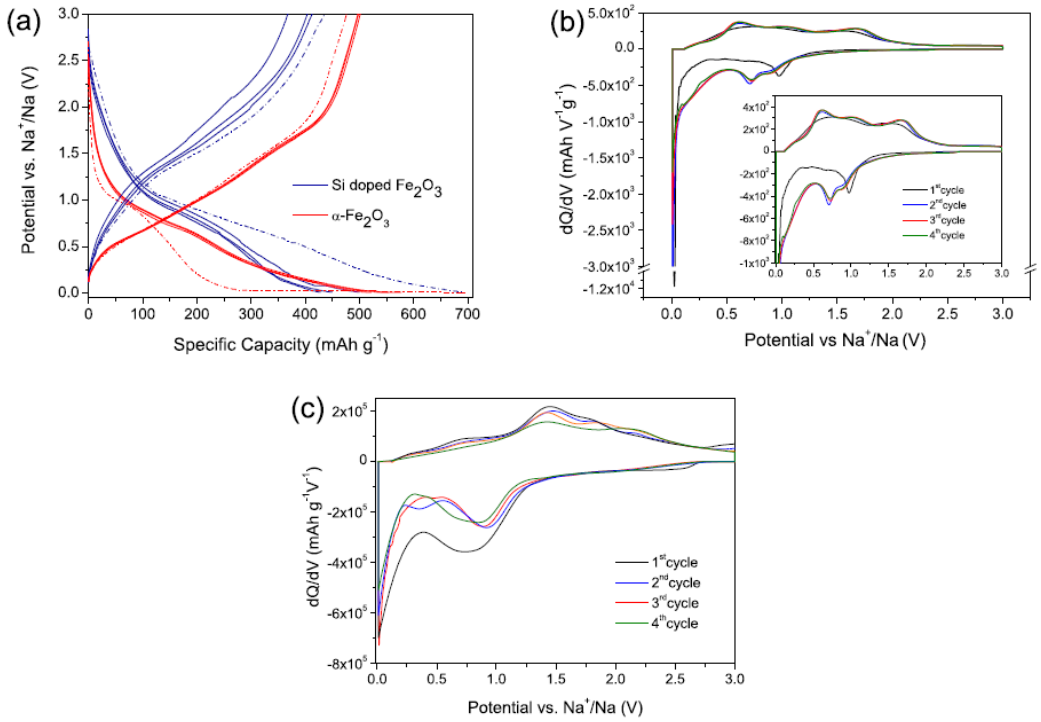

Figure 7.10: (a) Results of the PCGA analysis for the hematite and the Si-doped fiber; (b) Differential capacity plot calculated for the hematite (c); Differential capacity plot for the Si-doped fiber

fibers is comparable to the one obtained from the silicon doped phase, a contradictory result if compared to the rate capability test. In quasi-equilibrium conditions, indeed, the removal of any kind of kinetic limitation allows the system to attain its maximum capacity; this results firstly suggests that the main reason behind the better performance of the Si-doped fiber is its better kinetic properties, compared to the non-doped fibre, rather than additional specific capacity conveyed by the dopant to the material. The first cycle Coulombic efficiency also increases (from 37% to 72% for hematite) due to the absence of high surface area carbon black additive, which in turns leads to high irreversible capacities connected to SEI formation. In the case of hematite fibers, the relative differential capacity plot presented in Figure 7.10b allows to identify three different processes occurring during the first sodiation, namely: SEI formation, monophasic sodium insertion in hematite, and the conversion reaction at low potential. The first process is highlighted by an irreversible peak at 1.0 V in the differential capacity curve.[18] The sodium insertion can be identified with the sloping section of the potential profile between 100 and $300 mAh \cdot g^{-1}$, and corresponds to the flat curve in

the differential capacity plot. Eventually, the conversion to Fe^0 corresponds to the long plateau at 0.025 V in Figure 7.10a and the spike-like peak in Figure 7.10b. The low voltage plateau is registered during the first cathodic cycle only: the corresponding anodic scan shows two belly-like peaks of single phase domains in the differential capacity curve related to the extraction of sodium from the iron oxide with transitions from sodium-rich to sodium-poor phases. In the subsequent cycles, a set of two cathodic processes centred at 0.75 V appears, while the corresponding anodic peaks are at 1.20 V and 1.74 V vs. Na^+/Na. The cathodic process at 0.75 V, due to the Gibbs phase rule, unequivocally evidences the presence of an intermediate formation as a deviation from the monophasic profile occurs. The Si-containing fiber and Fe_2O_3 undergoes a different first sodiation process (Figure 7.10c): the differential capacity curve, indeed, does not show the low potential plateau, and the hematite spike-like peak becomes a belly-shaped peak, revealing that the hematite plateau should be related to a co-presence of a crystalline sodium-poor and an amorphous sodium-rich phase. In the subsequent anodic scan and the other cycles, the behavior of Si-doped $\alpha - Fe_2O_3$ becomes very similar to the hematite with a two-step red-ox processes maintained for several cycles, with the intermediate phase formation still evidenced. To summarize, in both cases we can identify an intermediate step during the conversion reaction ($x \leq 6$) that is:

$$Fe_2O_3 + xNa^+ + xe^- \rightleftharpoons Na_xFe_2O_3 \tag{7.3}$$

This sodium-rich intermediate can eventually further proceed towards the full reduction mechanism leading to Fe^0:

$$Na_xFe_2O_3 + (6-x)e^- + (6-x)Na^+ \rightleftharpoons 2Fe^0 + 3Na_2O \tag{7.4}$$

Intermediate transitions have been reported for the lithiation in the case of hematite,[41] but have been only hypothesized in the case of sodium.[44]

In order to ascertain the reversibility of the sodiation/de-sodiation process, Raman scattering of the $\alpha - Fe_2O_3$ based anode was measured before and after cycling, as reported in Figure 7.11a. Besides hematite phonon modes in the lower-frequency region of the spectra, the C sp^2 vibration modes (namely, D-, G- and G′-bands at 1350, 1580 and 2700 cm^{-1}) associated to the carbonaceous additive are detected, with the broad disorder-band superimposed to the most intense hematite spectral feature at $\tilde{1}315$ cm^{-1}. In the as-prepared electrode, contributions originating from binder (marked with stars) are also visible. These contributions are no longer present in the spectrum of the cycled anode, suggesting a deterioration of this component during Na^+ ion insertion/extraction process. On the contrary, the

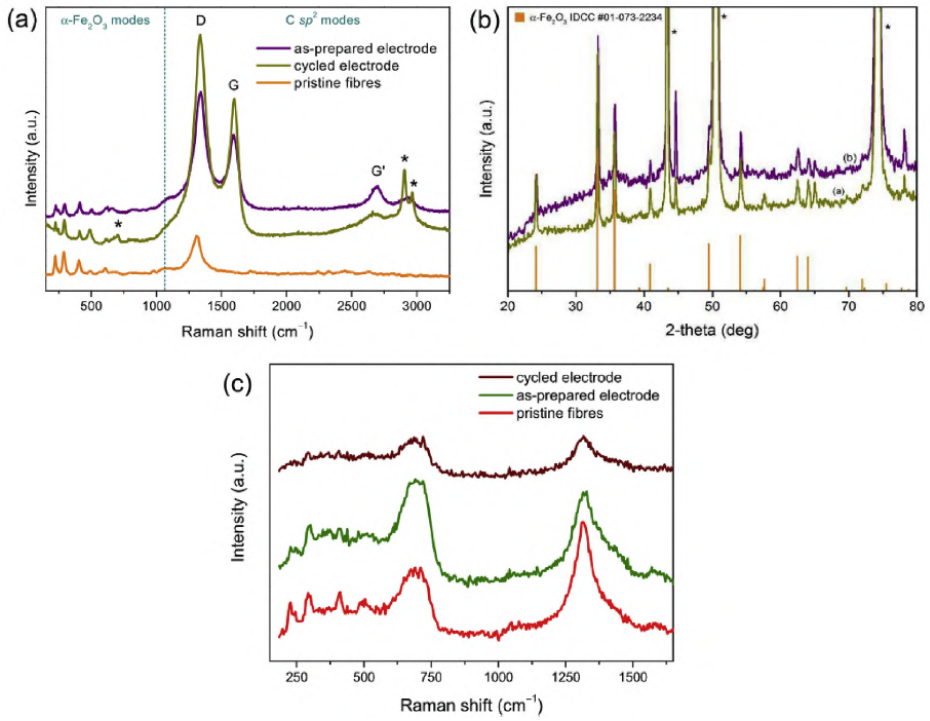

Figure 7.11: (a) Micro-Raman spectra and (b) XRPD diffractogram of the $\alpha - Fe_2O_3$ based anode. In both pictures, curves purple and green refer to electrode before and after cycling, respectively. The stars mark the spectral features arising from polyacrylate-based binder in the Raman spectra and the peaks of copper used as current collector in the XRPD pattern, respectively. (c) Results of Raman scattering measurements on the Si-doped Fe_2O_3 based anode.

hematite peaks in the spectrum of the cycled anode do not show changes in the positions with respect to the spectra of the pristine electrode and of the pure oxide fiber sample. The absence of peak shifts demonstrates that the sodiation/de-sodiation process is fully reversible, i.e. it occurs without causing permanent structural changes in the host $\alpha - Fe_2O_3$ lattice. The results of XRPD analysis (Figure 7.11b) fully agrees with these findings. Similar analyses have been performed on the Si-doped Fe_2O_3 based anode (without carbon additive) to evaluate the structural changes brought by the sodiation/de-sodiation process. However, no signal was detected on pristine electrodes in XRPD pattern of the pristine electrode, due to the lower intensity of the crystalline peaks. On the contrary, both maghemite and hematite phonon modes are detected in the Raman spectrum of pristine electrode (Figure 7.11c). After five charge/discharge cycles, the spectral fingerprint of

$\gamma - Fe_2O_3$ and $\alpha - Fe_2O_3$ are still visible, although considerably weakened in intensity. The insertion/extraction of Na^+ ions does not change the active material nanostructure, and it is likely to induce only an amorphisation of the fibres. This nanostructural change might be responsible for the observed spectral intensity lowering.

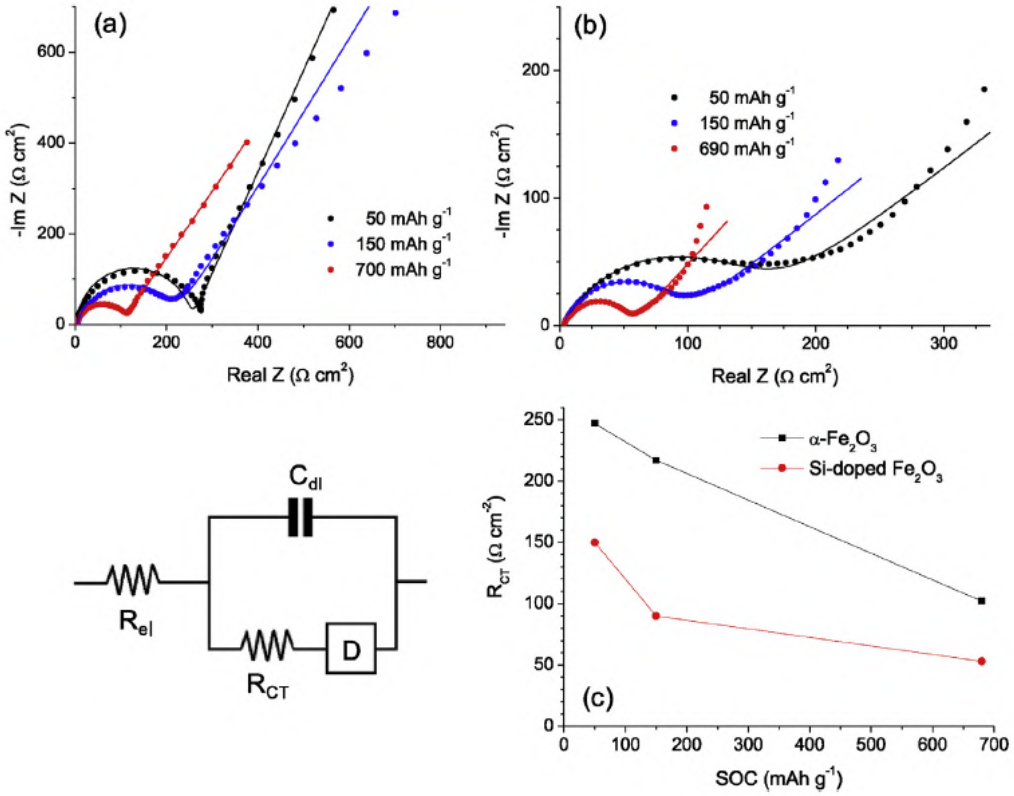

Figure 7.12: Nyquist plot at different SOC for (a) hematite and (b) the Si-doped fibres. (c) Charge transfer resistance values as function of the SOC.

Impedance spectroscopy analysis was carried out in a three-electrode cell in order to measure the Fe_2O_3/electrolyte impedance excluding contributes of the Na^+/Na interface (Figure 7.12). A preliminary set of measurements (not reported), was performed to verify the applicability of the Kirchhoff's law to the cell using the procedure already described elsewhere.[45] The Nyquist plots obtained from spectra on the as assembled cells (Figure 7.13) show very large impedance values at low frequencies. Cells were then charged in PCGA mode using a C/100 current threshold at three different states of charge (SOC): $50 mAh \cdot g^{-1}$, $150 mAh \cdot g^{-1}$, and full reduced

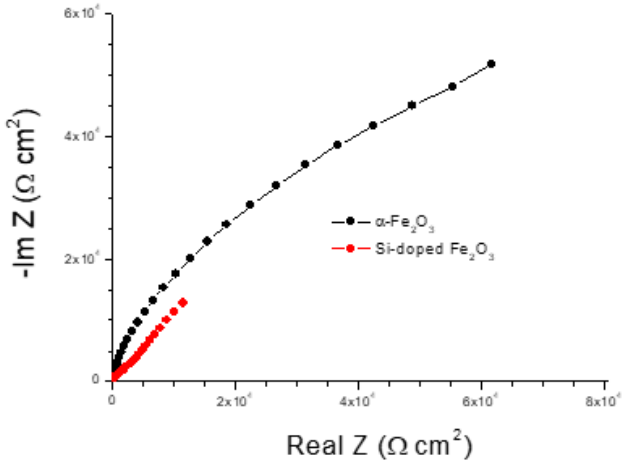

Figure 7.13: Nyquist plots of the pristine Fe2O3/interfaces in Swagelok cells at OCV after cell assembling

state (10mV cut off), where both electrodes show around $690 mAh{\cdot}g^{-1}$, in agreement with the capacities observed in coin cells. At the end of each charging step, the cells were allowed to attain the equilibrium for several hours and then the impedance spectra were taken. After the first reduction ($50 mAh{\cdot}g^{-1}$), at low SOC, the impedance undergoes a sudden decrease in both cells (black points in Figure 7.12a and b), showing the characteristic Randles type behavior of an electrochemical system (circuit reported in Figure 7.12): a portion of straight line at low frequencies, dominated by the diffusion element D, and a semi-circle due to the parallel combination of the charge transfer resistance of the electrochemical process (R_{CT}) and the double layer capacitance (C_{dl}) of the electrode. At very high frequency, the (R_C) arc cuts the real impedance axis at a value which corresponds to the electrolyte resistance (R_{el}). This very simple Randles model fits satisfactorily the spectra when a constant phase element (CPE) is used as the diffusion element. Model results are reported in the impedance spectra (Figure 7.12a and b) as continuous lines. More complex circuits, built using a larger number of discrete elements would give better fits at lower frequencies, but the physical interpretation could be more difficult due to the presence, at the electrode, of different phases. The main aim of the EIS analysis is to highlight and compare the charge transfer resistances of the two systems, which strongly depend on the transport properties of the active materials. Results are reported in Figure 7.12c. It is evident in both cases that the R_{CT} decreases with the state of charge, an effect that can be attributed

to the n-doping characteristic of the reduction process (low SOC) and the formation of a quasi-metallic, highly reduced phase at very high SOC. All the electrochemical characterizations converge in demonstrating that (i) the intrinsic mesoporosity of the fibres, their 1D nanostructure and the high surface area lead to increased rate performance and buffer the volume change during cycling improving the cyclability; (ii) doping with silicon enhances the kinetic of the resulting active materials towards the reaction with the sodium ions. The improved performance of the doped fibers cannot just be attributed to the reduced particle size because the Si-doping induces also a change of the electrochemical properties, as observed in the PCGA measurements. Thus, the reason for the different behavior should be related to structural and morphological properties of the new phase (maghemite) formed during the preparation. Hematite has been extensively investigated in electrochemistry as photoanode for water splitting. Preliminary works on bulk material showed that the Si-doping of hematite truly increases the photocurrent thanks the injection of electrons in the conduction band (n-doping).[22] Moreover, the presence on the nanosized domains of maghemite-type structure is also beneficial due to the lower and tunable band gap of $\gamma - Fe_2O_3$ (2.0 eV),[46] compared to $\alpha - Fe_2O_3$ (2.2 eV), which leads to an intrinsically more conductive phase. Similar behavior is here observed in the impedance features of pristine electrodes (Figure 7.13), where it is evident that the electrode made by the Si-doped phase is intrinsically less resistive compared to $\alpha - Fe_2O_3$. The early stage of the reduction process (low SOC, to $150 mAh \cdot g^{-1}$) does not provoke a drastic structural change, as shown by the potential profiles of PCGA measurements, but it leads to an improvement in the transport properties of the semiconductor due to the injection of a large number of electrons in the conduction band, as demonstrated by the abrupt decrease in the electrode impedance. Thus, both the Si-doping and the reduction process have similar effect in increasing the charge carriers amount. However, the comparison between the R_{CT} values (Figure 7.12c) in the whole SOC range reveals that the doped system has always better electron transport properties. A second important advantage of the Si-doping strategy is the remarkable increase of the electron mobility and the reduction of the transport activation energy, as clearly demonstrated in electrode films, which show structural (suppression of large crystalline domains) and morphological (nanosized elongated particles) analogies with our fibers. Finally, it might be surprising that the lower crystallinity does not lower the electron conductivity of the doped materials. However, the Si-doped fibers lack of grain boundaries, as observed by the direct comparison between Figure 2b and 3b. Finally, the morphological stability of the doped fibers can be observed in SEM images of the electrode after 70 cycles (Figure 7.14).

In the micrography of the cycled electrode, indeed, the fibers are still visible, together with flower-like structures which are formed by the evolution/ degradation of the organic binder as pointed out by EDX.

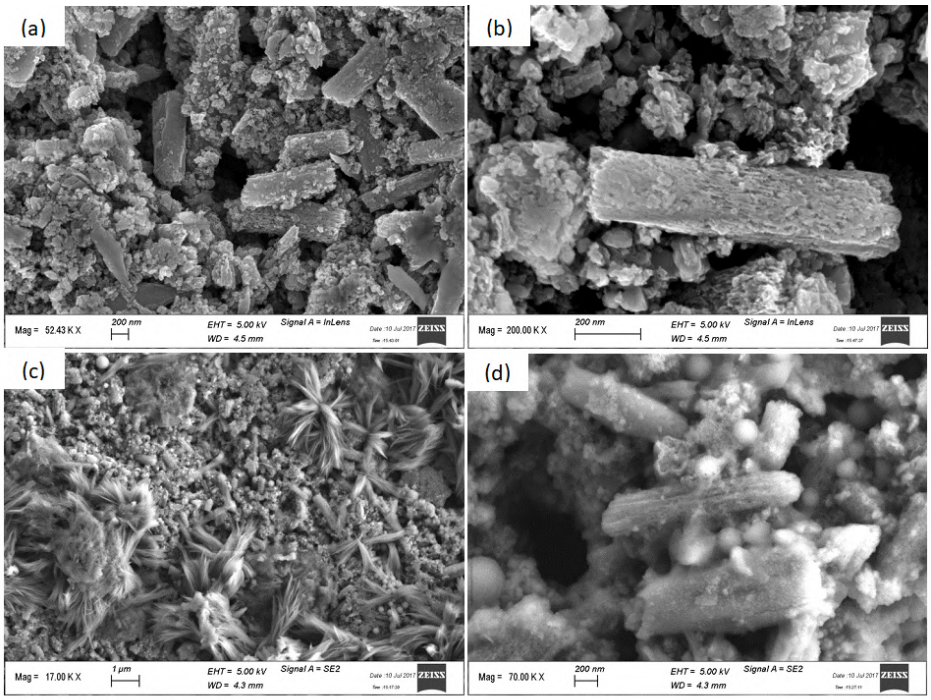

Figure 7.14: Low and high magnification SEM images of the electrode before (a,b) and after 70 cycles (c,d).

7.4.3 Conclusions

1D nanofibers iron (III) oxide were produced by cheap and easy scalable electrospinning method. Since the preparation proceeds through two well distinct steps (namely, fibrous film deposition and subsequent thermal treatment), there is the possibility of continuously producing electro-spun fibrous electrode materials that will be thermally treated separately, with no need of production interruption. This feature, together with the scalability of the process, makes this technique suitable for the manufacturing of SIB electrodes on industrial scale. The fibers show a peculiar morphology, which mitigates the pulverization of the electrode due to the conversion reaction. In the proposed method, doped phases (e.g. with silicon) can be obtained by simply adding the precursor to the sol-gel starting solution. The doping strategy improved transport properties in the phase and impact. The results

show that iron oxide 1D nanofibers doped with silicon exhibits a different phase with specific capacity nearly four times higher ($400 mAh \cdot g^{-1}$ at C/20) compared to the hematite phase. After 70 cycles, when the current imposed was set back to its original value of $50 mA \cdot g^{-1}$, the system still delivered 85% of the initial capacity showing an interesting capacity retention. Finally, thanks to the use of a carbon-free electrode and quasi-equilibrium electrochemical measurements, a sodium-rich intermediate was formed during the reduction of the oxide ($Na_x Fe_2 O_3$).

Bibliography

[1] M. C. Lott and S.-I. Kim, *Technology Roadmap, Energy Storage*. 2014.

[2] IRENA, "Renewables and Electricity Storage A technology roadmap for REmap 2030," no. June, 2015.

[3] D. Kundu, E. Talaie, V. Duffort, and L. F. Nazar, "The emerging chemistry of sodium ion batteries for electrochemical energy storage," *Angew. Chemie - Int. Ed.*, vol. 54, no. 11, pp. 3432–3448, 2015.

[4] J.-Y. Hwang, S.-T. Myung, and Y.-K. Sun, "Sodium-ion batteries: present and future," *Chem. Soc. Rev.*, vol. 46, no. 12, pp. 3529–3614, 2017.

[5] L. Chen, M. Fiore, J. E. Wang, R. Ruffo, D.-K. Kim, and G. Longoni, "Readiness Level of Sodium-Ion Battery Technology: A Materials Review," *Adv. Sustain. Syst.*, vol. 1700153, p. 1700153, 2018.

[6] P.-F. Wang, Y. You, Y.-X. Yin, and Y.-G. Guo, "Layered Oxide Cathodes for Sodium-Ion Batteries: Phase Transition, Air Stability, and Performance," *Adv. Energy Mater.*, vol. 1701912, p. 1701912, 2017.

[7] J. Cui, S. Yao, and J. K. Kim, "Recent progress in rational design of anode materials for high-performance Na-ion batteries," *Energy Storage Mater.*, vol. 7, no. December 2016, pp. 64–114, 2017.

[8] E. Irisarri, A. Ponrouch, and M. R. Palacin, "Review—Hard Carbon Negative Electrode Materials for Sodium-Ion Batteries," *J. Electrochem. Soc.*, vol. 162, no. 14, pp. A2476–A2482, 2015.

[9] Y. Cao *et al.*, "Sodium ion insertion in hollow carbon nanowires for battery applications," *Nano Lett.*, vol. 12, no. 7, pp. 3783–3787, 2012.

[10] K. Tang *et al.*, "Hollow carbon nanospheres with superior rate capability for sodium-based batteries," *Adv. Energy Mater.*, vol. 2, no. 7, pp. 873–877, Jul. 2012.

[11] V. L. Chevrier and G. Ceder, "Challenges for Na-ion Negative Electrodes," *J. Electrochem. Soc.*, vol. 158, no. 9, p. A1011, 2011.

[12] J. H. Kim, Y. H. Jung, J. H. Yun, P. Ragupathy, and D. K. Kim, "Enhancing the Sequential Conversion-Alloying Reaction of Mixed Sn–S Hybrid Anode for Efficient Sodium Storage by a Carbon Healed Graphene Oxide," *Small*, vol. 14, no. 4, pp. 1–11, 2018.

[13] F. Klein, B. Jache, A. Bhide, and P. Adelhelm, "Conversion reactions for sodium-ion batteries," *Phys. Chem. Chem. Phys.*, vol. 15, no. 38, p. 15876, 2013.

[14] P. R. Kumar, Y. H. Jung, K. K. Bharathi, C. H. Lim, and D. K. Kim, "High capacity and low cost spinel Fe_3O_4 for the Na-ion battery negative electrode materials," *Electrochim. Acta*, vol. 146, pp. 503–510, 2014.

[15] G. Longoni *et al.*, "Co_3O_4 negative electrode material for rechargeable sodium ion batteries: An investigation of conversion reaction mechanism and morphology-performances correlations," *J. Power Sources*, vol. 332, pp. 42–50, 2016.

[16] S. Komaba, T. Mikumo, N. Yabuuchi, A. Ogata, H. Yoshida, and Y. Yamada, "Electrochemical Insertion of Li and Na Ions into Nanocrystalline Fe_3O_4 and α-Fe_2O_3

Chapter 8

Paving the way towards highly efficient, high energy potassium-ion batteries with ionic-liquid electrolytes

Potassium-ion batteries are emerging as a potential alternative to LIBs with similar advantages of sodium-ion batteries but additional advantage that graphite can serve as negative electrode. Potassium manganese hexacyanoferrate, a Prussian blue analogue, is one of the most promising K-ion cathode materials with high discharge voltage and theoretical capacity, but challenges such as oxidative stability, poor cyclability and low efficiency remain. Here we report a systematic study of KMnHCFe as a K-ion cathode material using high-throughput synthesis and characterisation tools. Operating in a KFSI-containing ionic-liquid electrolyte KMnHCFe delivered good performance which was significantly influenced by particle size. The coulombic efficiency stabilising above 99.3% marks a significant improvement over the current state of the art. Crucially, in the same electrolyte graphite showed excellent performances (235 mAh/g, 99% capacity retention after 400 cycles, CE $\geq$ 99.9%) and exhibit the similar intercalation mechanism to the one in carbonate-based electrolytes. The work here presented reports a realistic and viable potassium-ion cell chemistry.

8.1 Background

Lithium-ion batteries (LIBs) currently dominate the market of power sources for portable devices thanks to their superior energy and power density. Econ-

omy of scale and engineering optimizations have driven the cost of LIBs below 200 $/KWh at the pack level, catalyzing the market penetration of electric vehicles and making them a viable candidate for stationary energy storage. The rapid market expansion of LIBs, however, has raised growing concerns about the sustainability of this technology in the future. In particular lithium and cobalt supplies are considered vulnerable, primarily because of the geopolitical implications of their concentration in only a few countries.[1]
Sodium-ion batteries (NIBs) have attracted considerable attention thanks to the higher abundance and wider distribution of sodium on the earth's crust when compared to lithium, meaning that a SIB manufacturing facility could be established virtually anywhere.[2] Moreover, since sodium does not alloy with aluminum, the latter can be used as the anode current collector in place of the more dense and costly copper.[3] Finally NIBs can be stored and transported in the fully discharged state, which improves safety and considerably reduces storage and transportation costs. Despite the extensive research, anode materials for SIBs still represent the Achilles heel to a full commercial exploitation of this technology.[2] Potassium ion batteries (KIBs) exhibit all the benefits of SIBs, with the additional advantage that graphite, the commercial standard anode material in LIBs, can reversibly accommodate K-ions, with a theoretical capacity of $279 mAh \cdot g^{-1}$ and a low operating potential of 0.3V vs K/K^+.[4,5,6] Although the research on cathode materials for KIBs is at its early stages, several potential active materials have already been proposed.[7] Among insertion-based transition metal oxides, cobalt and manganese oxides show a multi-step K-ion storage capability with capacities of $60 mAh \cdot g^{-1}$ and just over $100 mAh \cdot g^{-1}$, respectively.[8,9] Transition metal polyanions have also been investigated, for example Chihara et al. reported that $KVPO_4F$ and $KVOPO_4$ deliver high working voltage (above 3.95 and 4.02 V vs K/K^+ respectively) and discharge capacities around $70 mAh \cdot g^{-1}$.[10] The most promising class of cathodes for KIBs are Prussian Blue analogs (PBAs) with general formula $A_xP[R(CN)_6]xH_2O$, where A is the insertion cation, and P and R are transition metals (TM).[11] If both TM are red-ox active, the number of alkali ions per formula unit (x) can vary between 0 and 2, depending on the oxidation state of the TM and number of vacancies of the R site complex (primary lattice defect), which in turn depends on the synthesis conditions.[11,12] Thanks to the tunability of the transition metal in the P and R site, several different PBA based cathodes have been proposed in literature.[14,15,16] Among them, potassium manganese hexacyanoferrate ($K_2Mn[Fe(CN)]_6$, KMnHCFe) was reported to deliver high capacities (theoretical capacity of $155 mAh \cdot g^{-1}$) with an average potential around 4 V vs K/K^+.[16,17] The flip side of high voltage is electrolyte stability and corrosion of the aluminum current collec-

tor, as proved by the low coulombic efficiencies reported in the literature (ηC).[17] Fluoroethylene-carbonate (FEC) has been shown to improve ηC, however it is not compatible with the graphite anode.[17] High ηC and long term cycling of graphite electrodes, has been recently achieved in potassium bis(fluorosulfonil)imide (KFSI) based electrolytes, however severe aluminium corrosion accurs in the same electrolyte on the positive side. KPF_6 salts have been shown to suppress corrosion of the aluminum current collector,[18] but unfortunately they cause poor cycling performance at the graphite negative electrode.[19] Highly concentrated electrolyte of KFSI in ether solvents (i.e. 7M KFSI in DME) seem to suppress Al corrosion, however, although significantly improved, the coulombic efficiency (around 97%) is still too low for practical applications.[18,20] Therefore the biggest challenge for a full-cell KIB is the lack of a stable electrolyte compatible with both the positive (KMnHCFe) and negative (grafite) electrodes. The challenge of the electrolyte stability could also be addressed using ionic liquid (IL) electrolytes. The work on ILs for KIBs remains in its early stage, indeed only Beltrop et. al have so far reported potassium intercalation into graphite. The authors used a 0.3 M potassium bis(trifluoromethanesulfonyl)imide) (KTFSI) N-butyl-N-methyl bis(trifluoro-methanesulfonyl)imide ($Pyr_{1,3}TFSI$) ionic liquid, however a 2 wt% of ethylene sulfite had to be used as an SEI forming additive to prevent the TFSI anion co-intercalation into the graphite, that would result in disruption of the layered structure of the carbonaceous material.[21] In the present research activity, it is proposed for the first time the use of KFSI in pyrrolidinium1,3-FSI ionic liquid for KIBs, compatible with both the anode and the cathode active materials. An impressive long term stability of the graphite anode is proved (99% capacity retention after 400 cycles) and a K-ion intercalation mechanism analogous to carbonate based electrolytes is found. On the other hand, a high-throughput optimization of the KMnHCFe cathode is reported. Different concentration of precursors, chelating agent (K-citrate) and potassium chloride are used to tune the crystal nucleation and growth of the PBA. Four selected candidates are then fully characterized and their electrochemical properties investigated. We observe a strong correlation between the particle size on the cycling stability and ηC. In particular the optimized material exhibits the highest ever reported coulombic efficiency for KMnHCFe, over 99.3%. This find, for the first time opens up the possibility for highly efficient, high energy potassium ion batteries.

8.2 Methods

High throughput synthesis : The KMnHCFe particles were synthesized through a simple co-precipitation reaction by the automated pipetting robot Microlab NIMBUS (Hamilton). 24 different samples were synthesized with different concentrations of reactans, different Mn:citrate ratios, and with or without potassium chloride. In short an aqueous 25mM,75mM or 125mM solution of $MnCl_2{\cdot}4H_2O$ and Potassium citrate, was slowly dropped into a 25mM, 75mM or 125mM aqueous solution of $K_4Fe[CN]_6{\cdot}3H_2O$, with or without potassium chloride (1.5M). After mixing for 1 hour at 70^oC the white precipitate was centrifuged, washed 3 times with distilled water, and dried overnight at 70^oC.
Materials characterization : Elemental composition and thermal analysis coupled with mass spectrometry were performed by inductively coupled plasma optical emission spectrometry (Perkin Elmer Optima 8000) and thermogravimetric analysis mass spectrometry (NETZSCH STA 449 F3 Jupiter coupled to a QMS 403 Aolos). Scanning electron microscopy was carried out on a FE-SEM (Zeiss Merlin). Synchrotron X-ray diffraction was performed at beamline I11 at Diamond Light Source on the position sensitive detector (PSD). Fourier transform infrared spectroscopy (Thermo Scientific Nicolet 6700) was performed in attenuated reflectance (ATR) mode in a nitrogen filled glove box.
Electrochemical Tests: The graphite (SFG6, TIMCAL) was firstly ball milled for 3hours at 200 rpm (Restch PM100) to improve its rate capability and capacity retention.[22] The carbon based working electrode was then prepared mixing the graphite with poly(acrylic acid) (Mw$\approx$ 450000 Da, Sigma-Aldrich) in the weight ratio of 9:1 respectively. This mixture was dispersed in 1-methyl-2-pyrrolidone (NMP) to prepare the slurry and finally casted on aluminum foil using a doctor blade. The casting was dried under vacuum at 80^oC overnight and then roll-pressed. The KMnHCFe working electrodes were prepared in a similar way, but the active material was mixed with SuperP carbon (TIMCAL Carbon Black Super P) and poly(vinylidene fluoride) (MTI corp, MW 600,000) in the weight ratio of 7:2:1. The slurry was casted on carbon coated aluminum. Disks of 10 mm diameter were punched out, the active material loading was between $1,5$ and $2mg{\cdot}cm^{-2}$. The electrolyte used was a $1mol{\cdot}kg^{-1}$ solution of potassium bis(fluorosulfonyl)imide (KFSI, 99,9% Solvionic) in N-Propyl-N-methylpyrrolidinium bis(fluorosulfonyl)imide ($Pyr_{1,3}FSI$, 99,9%, Solvionic). The ionic liquid was dried under vacuum overnight; the water content as measured by Karl Fischer Titration (C30S KF, Mettler Toledo) was below 15 ppm.

Except where otherwise specified, the electrochemical tests were performed in three electrode cells with potassium metal acting as counter (CE) and reference electrodes (RE). Before assembling the cells, the surface of the potassium metal was mechanically cleaned to remove oxides and other possible contaminants, and successively it was immersed for 15 hours into the electrolyte. This step was necessary because of the high reactivity of the potassium metal. Indeed, when the ionic liquid electrolyte was used, the impedance spectra of a symmetrical alkali metal cell appears to stabilize after 15 hours. This result suggests at least a partial stabilization of the alkali metal after 15 hours. On the other hand, the impedance spectra did not stabilize with the 1M KFSI or a 0,7M KPF_6 in EC:DEC (1/1 vol) electrolytes (Figure 8.1). Two-electrode measurements were performed in 2032 coin cell,

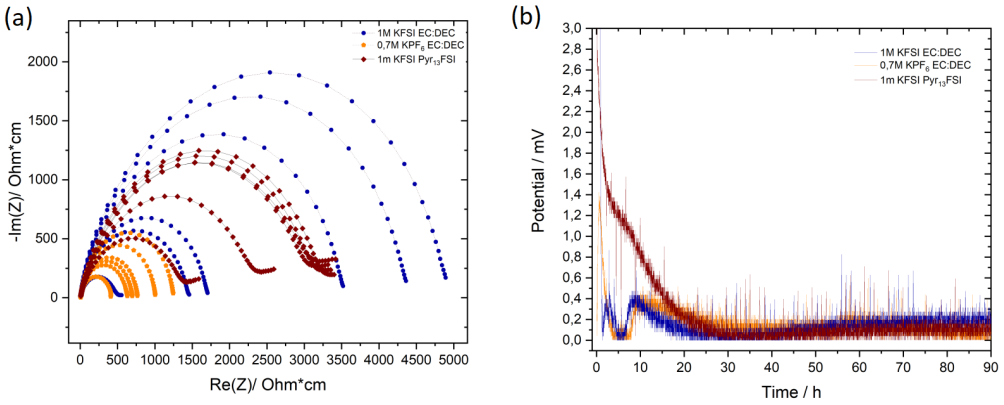

Figure 8.1: Potassium metal symmetrical cells were maintained at the Open circuit potential (OCV) for 90 hours. (a) Selected Nyquist plots in the frequency range 10kHz-100mZ taken every hour, the ones taken after of 1h,5h,15h,30h,60h and 90h after the cell was assembled are shown. (b) Relative variation of the OCV during time.

with potassium metal acting both as CE and RE. In this configuration the polarization of the reference electrode was calculated to be below 60 mV and 15 mV for the cycle life tests of the graphite and the KMnHCFe electrodes respectively. In any case, the explored electrochemical window was sufficiently wide to fully charge and discharge the electrodes, as demonstrated by the consistency of the results between two and three-electrode configuration.

8.3 Results and discussion

8.3.1 High-throughput optimization and detailed characterization

The PBA cathode material was optimized via high-throughput synthesis and characterization. Three synthesis parameters that have been shown to influence PBA morphology in previous studies were explored simultaneously for the first time in this work. Those parameters are the concentration of the precursors manganese(II) chloride and potassium hexacyanoferrate ($[MnCl_2] = [Mn] = [K_4[Fe(CN)_6]_2$: 25, 75, 125 mM), the ratio of potassium citrate to manganese chloride ([citrate]/[Mn] : 1, 2.5, 5, 10), and the presence of potassium chloride ($[KCl]$: 0, 1.5 M). The upper limits of the ranges were chosen as a compromise between the solubility limits of potassium citrate, potassium hexacyanoferrate, and potassium chloride. The search space of synthesis conditions is mapped in Figure 8.2a. The effect of these parameters on three physical properties, crystal structure, particle size, and vacancy content, was measured. The crystal structures of all 24 materials were measured via X-ray diffraction (XRD). Diffractograms of the materials on the 8 corners of the search space are plotted in Figure 8.2b. All 24 materials have monoclinic geometries and are members of the $P2_1/c$ space group. Peak broadening was more significant for samples at higher reactant concentrations, lower citrate concentrations, and in the presence of potassium chloride. We attribute this peak broadening to decreasing particle size, which is matched by the particle sizes calculated in the refinement. This conclusion is further supported by particle size analysis of SEM images, Figure 8.2d (SEM images in Figures 8.3,8.4,8.5). Most samples had particle sizes below 100nm, and only four samples had particle sizes above 1000nm. Finally, the vacancy content of the samples were determined via inductively coupled plasma optical emission spectroscopy (ICP-OES). The vacancy contents are plotted in Figure 8.2e. The samples with the highest fraction of [Fe(CN)6] octahedra (and therefore the lowest vacancy content) were those synthesized in the highest citrate concentration. At a citrate-to-manganese ratio of 10, all samples had a vacancy content below 5%. Based on these high-throughput results, four materials with monoclinic geometry, intermediate particle size, and low vacancy were selected for further study.

The four materials were synthesized in larger batches under the conditions listed in Table 8.1 which presents also the results of their characterisation including particle size 'd', composition values 'x' '1-y' 'w' which represent the potassium, vacancy and water content respectively.

SEM micrographs of these 4 materials are shown in Figure 8.6a-d. Accord-

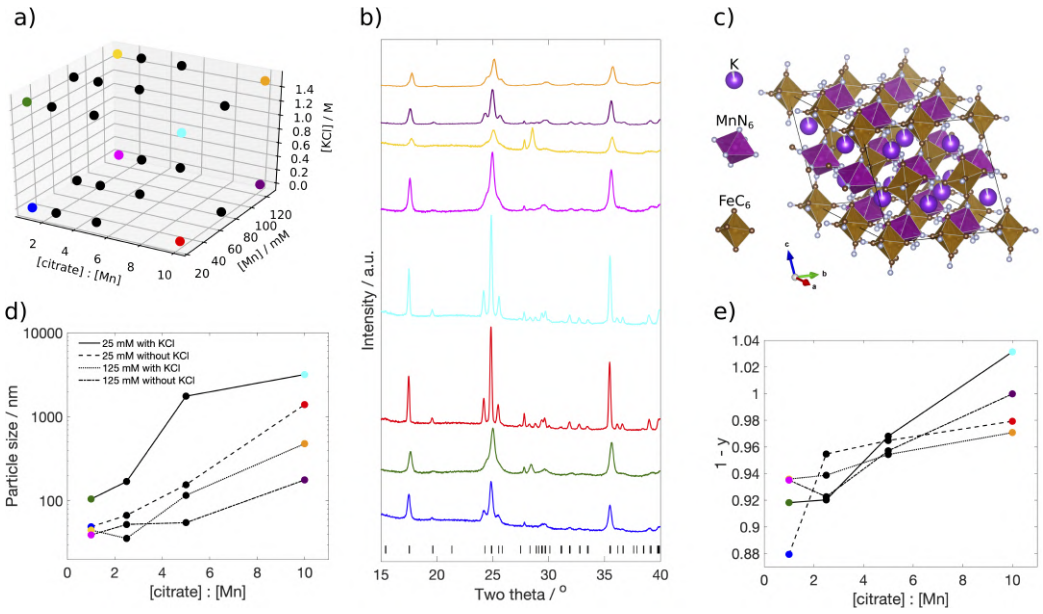

Figure 8.2: High-throughput synthesis and characterization of KMF. (a) The search space for the synthesis parameters. (b) The diffractograms of the materials at the 8 corners of the search space. (c) A schematic of the crystal structure. (d) The effect of the ratio of citrate to manganese on the materials particle size, as determined by analysis of the electron micrographs. (e) The effect of the ratio of citrate to manganese on vacancy content, as determined by ICP-OES.

ing to their size, the materials are designated KMF_{39}, KMF_{55}, KMF_{177}, and KMF_{297}. They are approximately cubic in shape and the smallest particles experience significant agglomeration. All the materials were highly potassiated as synthesized, with at least 1.85 potassium atoms per formula unit. This indicates both low vacancy, confirmed by the ratio [Fe]:[Mn] = 1 - y which is at least 94% for all samples, as well as a low oxidation state, which is predominantly +2 for both iron and manganese. Thermogravimetric analysis (TGA) of the 4 samples show mass losses of between about 5% and 2% from about 100^oC up to a decomposition temperature of between about 350 and 400^oC (Figure 8.6f).

This corresponds to a loss of surface-absorbed water, zeolitic water (present in the interstices), and water coordinated to manganese at vacancies of the hexacyanoferrate octahedra. The water contents per formula unit are presented alongside the ICP-OES data in Table 8.1. Water content increases from 0.28 to 0.78, with decreasing particle size. The relationship is due in part to the fact that smaller particles have larger surface-area-to-volume

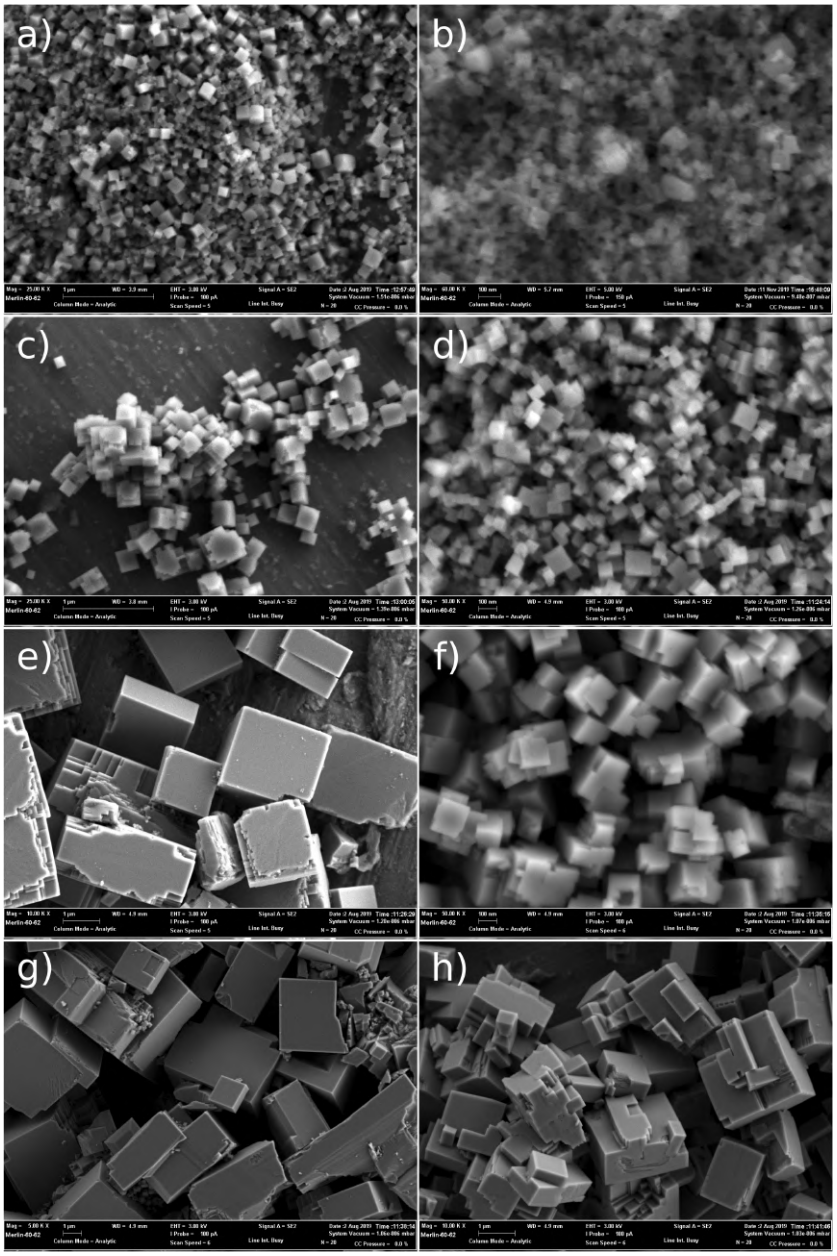

Figure 8.3: SEM micrographs of sample prepared with [Mn] = 25mM. The [citrate]:[Mn] of (a) and (b), (c) and (d), (e) and (f), and (g) and (h) are 1, 2.5, 5, and 10 respectively. The [KCl] of (a), (c), (e), and (g) is 0M and the [KCl] of (b), (d), (f), and (h) is 1:5M.

ratios, and because smaller particles have higher vacancy contents. This convolution of causes is well known in the literature and more careful study to

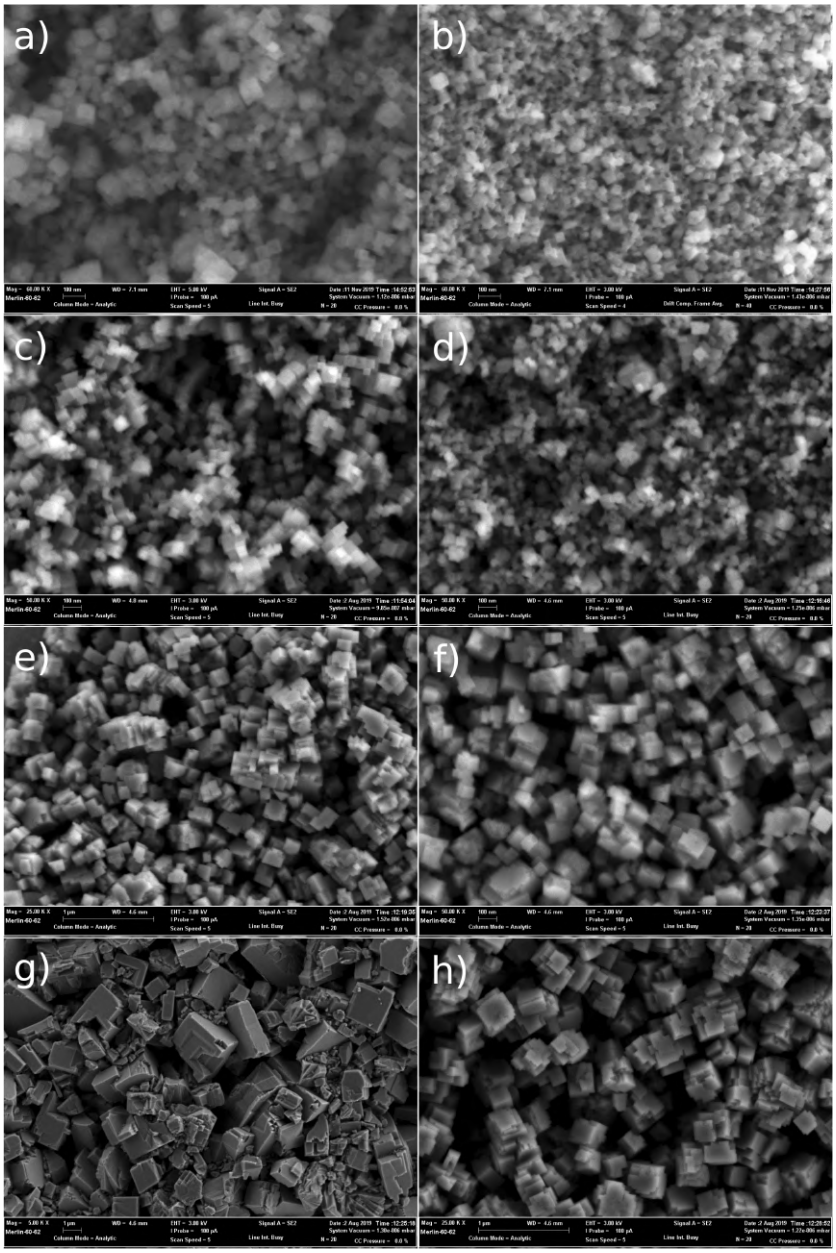

Figure 8.4: SEM micrographs of sample prepared with [Mn] = 75mM. The [citrate]:[Mn] of (a) and (b), (c) and (d), (e) and (f), and (g) and (h) are 1, 2.5, 5, and 10 respectively. The [KCl] of (a), (c), (e), and (g) is 0M and the [KCl] of (b), (d), (f), and (h) is 1:5M.

understand the separate effects is warranted.
Fourier-transform infrared spectroscopy (FTIR) data agree with the size-to-

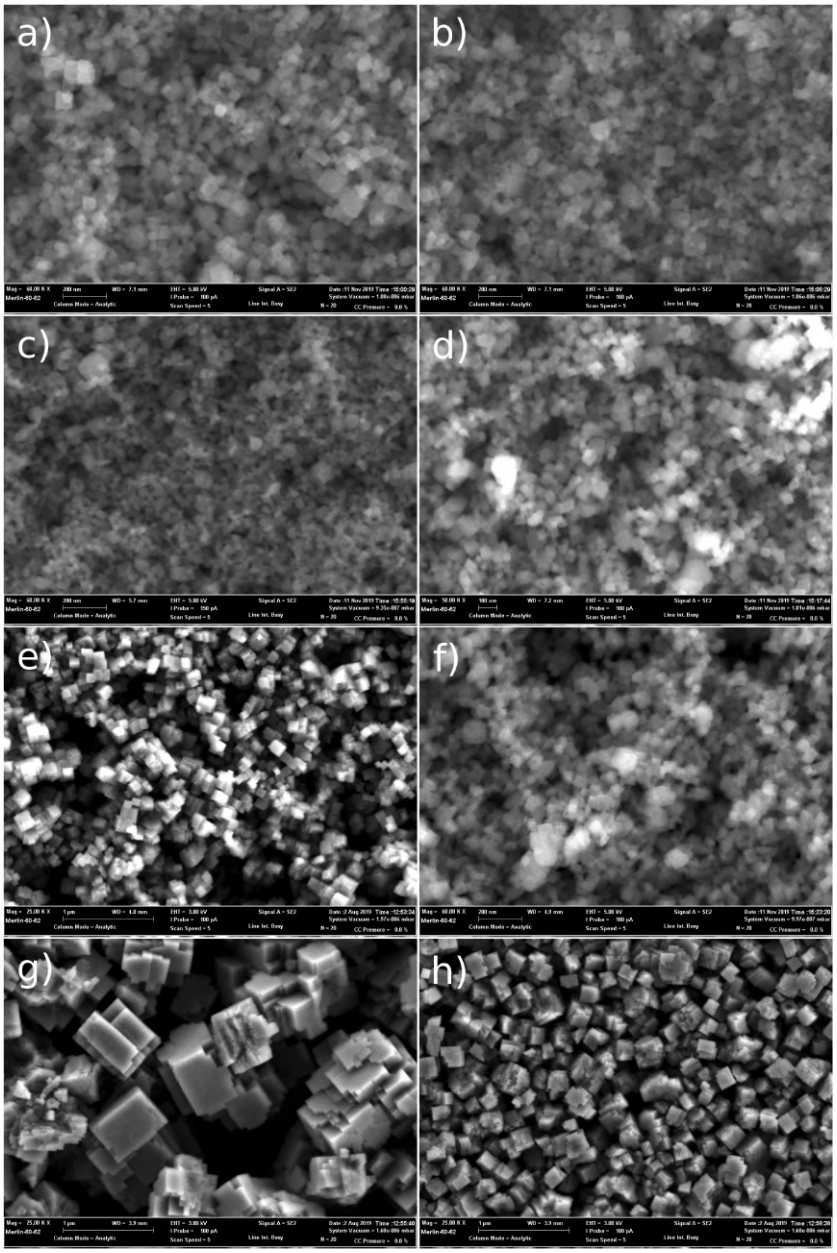

Figure 8.5: SEM micrographs of sample prepared with [Mn] = 125mM. The [citrate]:[Mn] of (a) and (b), (c) and (d), (e) and (f), and (g) and (h) are 1, 2.5, 5, and 10 respectively. The [KCl] of (a), (c), (e), and (g) is 0M and the [KCl] of (b), (d), (f), and (h) is 1:5M.

water-content trend. The spectra, shown in Figure 8.6, contain two peaks arising from water: a broad peak between 3100 and $3600 cm^{-1}$ and sharper

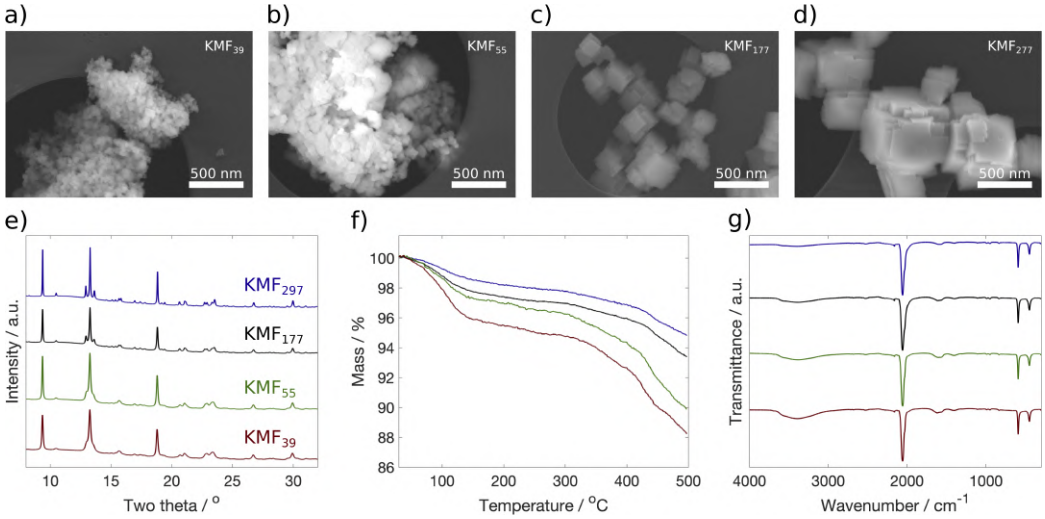

Figure 8.6: Characterisation of the four selected KMF materials. (a-d) SEM micrographs of KMF_{39}, KMF_{55}, KMF_{177}, and KMF_{297} respectively; (e) Synchrotron XRD, (f) FTIR, and (g) TGA of the four selected materials.

peak at about $1650cm^{-1}$. Both of these decrease in intensity as the samples increase in particle size. Sharp peaks at 2057, 592, and $449cm^{-1}$ correspond to the framework vibrations $\nu(CN)$, $\delta(FeCN)$ and $\nu(FeC)$ respectively. The structural distortion of the materials away from cubic, observed in the synchrotron XRD data, effects slightly different environments for the Fe-CN-Mn bonds. This gives rise to the shoulder observed on the peak at $2057cm^{-1}$.

8.3.2 Electrochemistry of manganese hexacyanoferrate

After high-throughput selection of 4 promising PBA candidates and thorough materials characterization, the 4 samples were subjected to electrochemical tests in a half-cell configuration to select the best performing one. The sam-

Sample	[Mn] (mM)	[citrate]:[Mn]	[KCl] (M)	d (nm)	x	1-y	w
KMF_{39}	125	1	1.5	39	1.92	0.95	0.78
KMF_{55}	125	5	1.5	55	1.86	0.94	0.52
KMF_{177}	125	10	1.5	177	1.91	0.97	0.43
KMF_{297}	75	10	1.5	297	1.89	0.98	0.28

Table 8.1: Synthesis parameters of the four selected materials and results of their characterization including particle size (d), composition values (x, 1-y, w)

ples were cycled at C/10 in a coin cell with potassium metal as counter and reference electrode and an ionic liquid electrolyte, 1 mol/kg KFSI in $Pyr_{1;3}FSI$. The specific capacity versus cycle number for the samples is plotted in Figure 8.7a. Ordered by first-cycle specific capacities, the materials are KMF_{55} ($133 mAh{\cdot}g^{-1}$) > KMF_{39} ($129 mAh{\cdot}g^{-1}$) > KMF_{177} ($111 mAh{\cdot}g^{-1}$) > KMF297 ($90 mAh{\cdot}g^{-1}$, though it quickly increases to $100 mAh{\cdot}g^{-1}$, possibly due to a surface activation process[16,17]). The decrease in the specific capacity with the increase of the particle size suggests that at some particle size above 55nm either the electronic or ionic conductivity of the material limit the potassium-insertion reaction. It is possible the heavily distorted diffusion channels and large K-ion size result in poor bulk diffusion.
On the other hand the cyclability of the samples is much greater for the larger particles. In fact, the trend in capacity retention after 30 cycles (30th cycle discharge capacity compared to the maximum) is the opposite to that of 1st-cycle specific capacity. While capacity fade in PBA electrodes has been attributed to numerous factors including phase transformations, manganese(III) disproportionation, cathode dissolution, and parasitic reactions with crystalline water, the correlation with particle size suggests in this case the decreasing capacity stems from surface specific phenomena. The improved cyclability of KMF_{297} and KMF_{177} is associated with high coulombic efficiency. Indeed after a first cycle coulombic efficiency of 77% and 80% respectively (Figure 8.7b), the η_C steadily increases to over 98% in the following cycles, and finally stabilizes above 99.3% by the 25th cycle. As a comparison with the literature, although the exact values of η_C in half-cells are not often reported, they range between 90% and $\approx$ 97%.[16,20] Higher η_C has been proved only with FEC, but this additive is not compatible with the graphite anode.[17] Despite being often neglected, the relevance of the coulombic efficiency for practical applications should not be underestimated. As a matter of fact, it has been proved a close correlation between steady coulombic efficiency and the full battery cycle life.[23] Here, the optimization of particle size, the high cathodic stability of the ionic liquid electrolyte,[24] and the suppressed Al-corrosion due to the high concentration of FSI anions in the electrolyte,[18] all contribute to the remarkably high coulombic efficiency.

KM_{177} was selected as the best compromise between cyclability and specific capacity, and was therefore further analysed. Over the first 100 cycles KM_{177} retains 87.4% of the first-cycle specific capacity (Figure 8.7b). The results of the rate test in a three-electrode cell are reported in Figure 8.7c-d. In the initial charge, the specific capacity is above the theoretical value (164 vs $155 mAh{\cdot}g^{-1}$). This may result from decomposition of the electrolyte and surface driven side reactions, as reported in literature.[17] Figure 8.7c at C/20

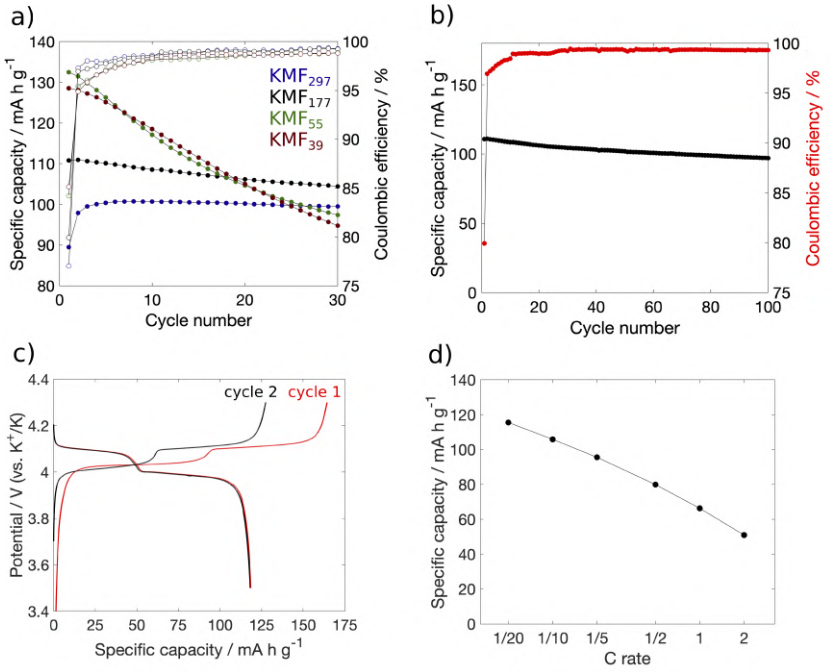

Figure 8.7: Cycling results for the KMF cathode: a) half cell charge and discharge capacity at C/10 for the four selected PBAs, from the smallest particle size to the biggest: KMF_{39}, KMF_{55}, KMF_{177}, and KMF_{297}; b) capacity retention of KMF_{177} over the first 100 cycles at C/10 in two electrode configuration; c) first and second galvanostatic provile at C/20, and e) rate capability of KMF_{177} at C rater from C/20 to 2C.

the capacity is $119 mAh \cdot g^{-1}$. When increasing the current in both the charge and discharge, the cathode retains 89% at C/10, 80% at C/5 and 67% at C/2, 56% at 1C and 43% at 2C. This specific capacity,while lower than the theoretical value and lower than other reported rate capabilities[14] is likely due to a combination of the slower kinetics discussed above as well as the use of an ionic-liquid electrolyte, which has a lower potassium-ion transference number relative to organic electrolytes used in previous studies[24] The latter may be improved by optimizing the potssium salt concentration in the ionic liquid.

The charge-discharge profiles of the KMnHCFe show two distinct plateaus assigned to the change in the oxidation state of the Fe and Mn respectively. Two redox process are evidenced from the differential capacity plot (Figure 8.8). At C/20, they are centered in charge at 3.99 V and 4.10 V, and in discharge at 4.04 V and 4.11 V respectively. The corresponding average potentials, calculated by dividing the energy density measured in the half-cell

by the capacity[25] are V_{cat} 4.02 V and V_{an} 4.08 V. All potentials are given versus the K^+/K redox couple.

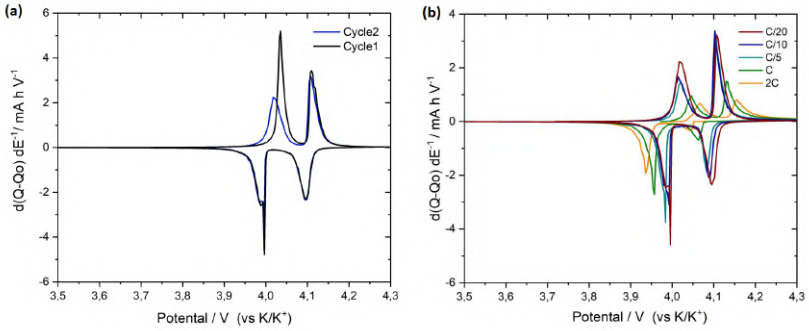

Figure 8.8: Differential capacity plot of the KM_{177} KMnHCFe as obtained from the three electrode cell rate test. (a) 1^{st} and 2^{nd} cycle at C/20; (b) 2^{nd} cycle at at different rates C/20, C/10, C/5, C/2, C, 2C.

8.4 Electrochemistry of a graphite anode

To understand the feasibility of pairing this optimized PBA potassium-ion cathode with a graphite anode in a practical full-cell battery, the electrochemical intercalation of potassium into graphite in an ionic-liquid electrolyte was evaluated. The cycle life and rate capability of the graphite anode in the 1 mol/Kg KFSI $Pyr_{1,3}FSI$ electrolyte are reported in Figure 8.9. The first and second charge-discharge profiles of the cycle life test are reported in Figure 8.9a The galvanostatic profiles have several steps, with the longest plateau located at 0.20 and 0.25V versus the K^+/K redox couple upon K^+ intercalation and deintercalation, respectively. Figure 8.9b shows the high cyclability of the graphite anode. Indeed, after 5 SEI forming cycles at C/20, the capacity stabilizes at 235 $mAh{\cdot}g^{-1}$ at C/5. The charge discharge coulombic efficiency, after gradually increasing in the early cycles, reaches over 99.9%, proving that the FSI-containing ionic liquid can form a stable SEI on the graphite electrode. Indeed, despite the non negligible expansion of the interlayer distance that occurs during cycling (60% along the c axis,[26]) the capacity retention was 99% after 400 cycles. The graphite anode can deliver significant capacity even at high rates. The relatively similar capacities at C/20, C/10 and C/5 (246, 243 and 241$mAh{\cdot}g^{-1}$), agrees well with the negligible variation of the average working potential as reported in the differential capacity plot. Worth to be mentioned, even at 2C, the main reduction peak is

centered at 0.115 V, a value well above 0 V. This significantly reduces safety concerns regarding potassium metal plating and/or dendrite formation on the electrode. In terms of rate capability, even at C and 2C, the graphite retains 94% and 88% of the low rate, C/20 capacity, respectively.

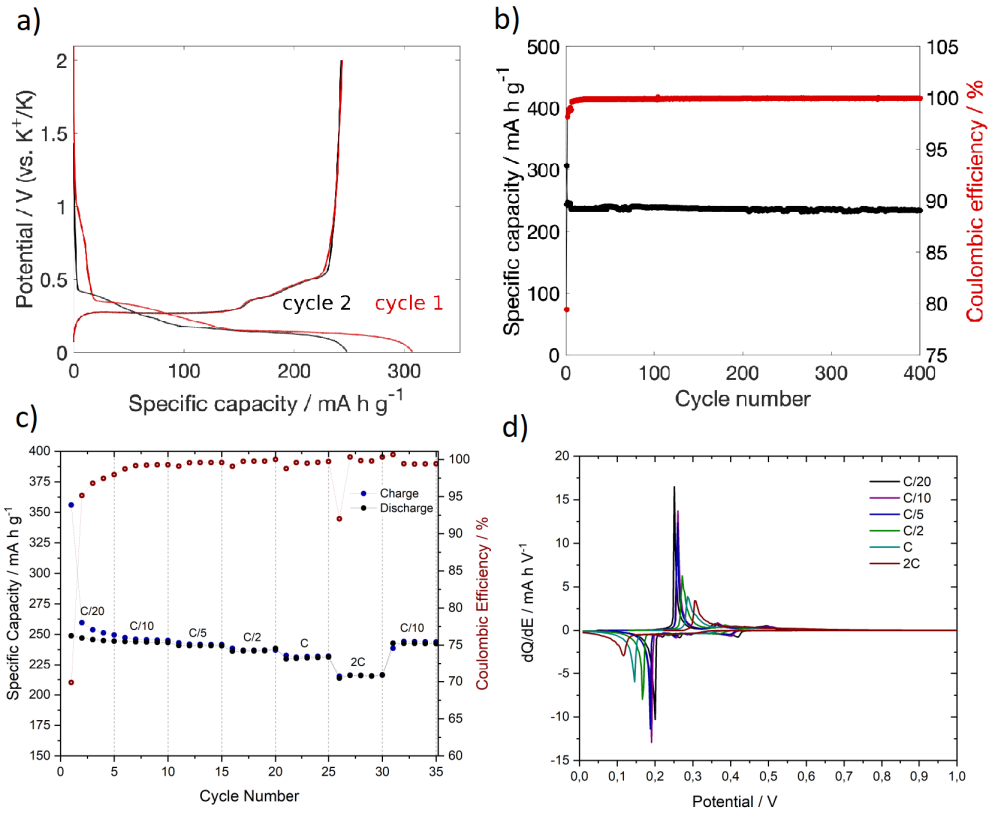

Figure 8.9: Galvanostatic cycling results for the graphite anode: (a) Coulombic efficiency and capacity evolution for the K^+ intercalation (blue) and deintercalation (black) for 250 cycles, cycles 1-5 at C/20 and 6-250 at C/5 in a two-electrode Cell; (b) Charge and discharge profiles for selected cycles (1 at C/20 dashed line, and 6,10,50,100,150,200,250 at C/5) as obtained from the cycling stability test; (c) Rate capability of graphite in a three-electrode cell; (d) Differential capacity plot for different currents applied as obtained from the rate capability test.

To study the potassium intercalation mechanism into graphite, operando XRD was performed. In agreement with what reported in literature, Figure 8.10 illustrates a multi-stage structural evolution of the graphite during the first cycle.[19,27] Several identifiable, stage-n graphite intercalation compounds (GICs) are found, where the n index is the number of graphene layers

between intercalation planes.[27] In the first region (between 2 V and 0.33 V) non significant changes in the structure are found, indicating a probable decomposition of the electrolyte (and SEI formation) rather than K^+ intercalation into the graphite. Between 0.33 V and and 0,20 V first the KC_{48} (stage-4) and then the KC_{36} (Stage-3) appear. Below 0,20 V, down to 0,15 V the KC_{24} (stage-2) appears. Finally further reduction leads to the fully potassiated graphite KC_8 (stage-1) as demonstrated by the appearing of the peak at 33.5^o. In the following anodic, the phases appearing is reversed, and at the end of the discharge the original (002) peak of the graphite is restored, confirming the high reversibility of the process. Additionally, in this ionic liquid electrolyte we don't observe a shoulder, corresponding to an additional phase, on the (002) peak in the depotassiated state that is reported for other electrolytes.[27,28]

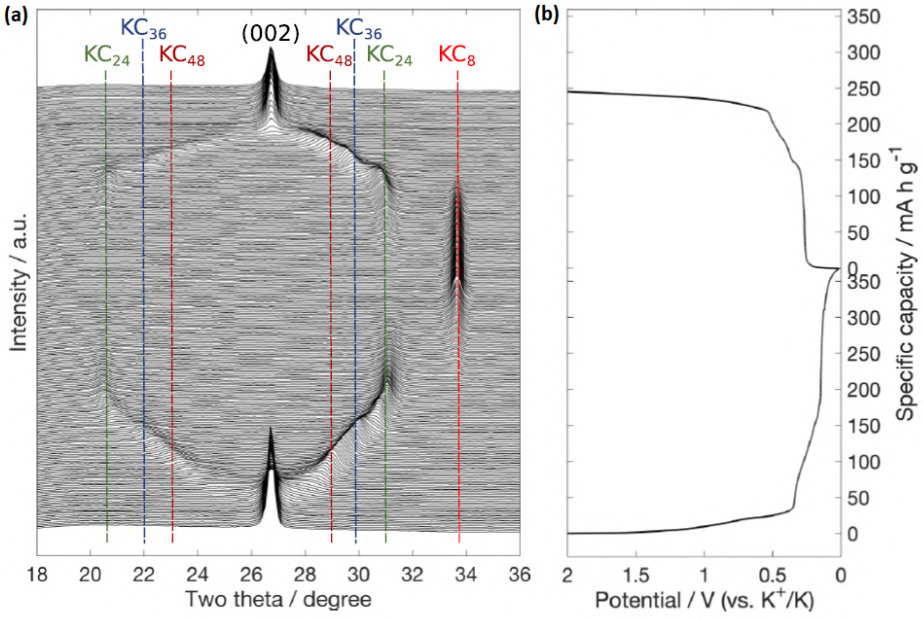

Figure 8.10: (a) *Operando* X-Ray diffraction patterns, and (b) Potential versus capacity profiles of the K^+ ion insertion at C/20. The major peaks for the intermediates KC 48 ,KC 36 , KC 24 and KC 8 are highlighted.

8.5 Conclusions

In summary, its was investigated and optimized the synthesis of KMnHCFe as a cathode material for K-ion batteries. Systematic investigation of synthesis

conditions allowed for minimization of vacancies and water whilst achieving a fine control of particle size. Operating for the first time in a KFSI-containing ionic-liquid electrolyte KMnHCFe showed improved coulombic efficiency over 9.3%, and capacity retention of 87.4% after 100 cycles. The electrochemical performance showed a pronounced dependence on particle size with smaller particles having larger specific capacity but poor cyclability, and larger particles having lower capacity but better cyclability. Poor electronic conductivity or bulk cation mobility might hinder specific capacity whilst surface specific reactions appear to be the primary cause of capacity decay, rather than phase transformations. Graphite has shown excellent performance in the same electrolyte demonstrating that this system is a viable chemistry for high-performance K-ion batteries.

Bibliography

[1] E. A. Olivetti, G. Ceder, G. G. Gaustad, and X. Fu, "Lithium-Ion Battery Supply Chain Considerations: Analysis of Potential Bottlenecks in Critical Metals," *Joule*, vol. 1, no. 2, pp. 229–243, 2017.

[2] J.-Y. Hwang, S.-T. Myung, and Y.-K. Sun, "Sodium-ion batteries: present and future," *Chem. Soc. Rev.*, vol. 46, no. 12, pp. 3529–3614, 2017.

[3] L. Chen, M. Fiore, J. E. Wang, R. Ruffo, D.-K. Kim, and G. Longoni, "Readiness Level of Sodium-Ion Battery Technology: A Materials Review," *Adv. Sustain. Syst.*, vol. 1700153, p. 1700153, 2018.

[4] Y. Okamoto, "Density functional theory calculations of alkali metal (Li, Na, and K) graphite intercalation compounds," *J. Phys. Chem. C*, vol. 118, no. 1, pp. 16–19, 2014.

[5] W. Luo *et al.*, "Potassium Ion Batteries with Graphitic Materials," *Nano Lett.*, vol. 15, no. 11, pp. 7671–7677, 2015.

[6] S. Komaba, T. Hasegawa, M. Dahbi, and K. Kubota, "Potassium intercalation into graphite to realize high-voltage/high-power potassium-ion batteries and potassium-ion capacitors," *Electrochem. commun.*, vol. 60, pp. 172–175, 2015.

[7] J. Y. Hwang, S. T. Myung, and Y. K. Sun, "Recent Progress in Rechargeable Potassium Batteries," *Adv. Funct. Mater.*, vol. 28, no. 43, pp. 1–45, 2018.

[8] Y. Hironaka, K. Kubota, and S. Komaba, "P2- and P3-K_xCoO_2 as an electrochemical potassium intercalation host," *Chem. Commun.*, vol. 53, no. 26, pp. 3693–3696, 2017.

[9] H. Kim *et al.*, "Investigation of Potassium Storage in Layered P3-Type $K_{0.5}MnO_2$ Cathode," *Adv. Mater.*, vol. 29, no. 37, pp. 1–6, 2017.

[10] K. Chihara, A. Katogi, K. Kubota, and S. Komaba, "$KVPO_4F$ and $KVOPO_4$ toward 4 volt-class potassium-ion batteries," *Chem. Commun.*, vol. 53, no. 37, pp. 5208–5211, 2017.

[11] K. Hurlbutt, S. Wheeler, I. Capone, and M. Pasta, "Prussian Blue Analogs as Battery Materials," *Joule*, vol. 2, no. 10, pp. 1950–1960, 2018.

[12] A. Zhou, Z. Xu, H. Gao, L. Xue, J. Li, and J. B. Goodenough, "Size-, Water-, and Defect-Regulated Potassium Manganese Hexacyanoferrate with Superior Cycling Stability and Rate Capability for Low-Cost Sodium-Ion Batteries," *Small*, vol. 1902420, p. 1902420, 2019.

[13] X. Wu, Z. Jian, Z. Li, and X. Ji, "Prussian white analogues as promising cathode for non-aqueous potassium-ion batteries," *Electrochem. commun.*, vol. 77, pp. 54–57, 2017.

[14] G. He and L. F. Nazar, "Crystallite Size Control of Prussian White Analogues for Nonaqueous Potassium-Ion Batteries," *ACS Energy Lett.*, 2017.

[15] B. Huang *et al.*, "Prussian Blue $K_2FeFe(CN)_6$ Doped with Nickel as a Superior Cathode : An Efficient Strategy to Enhance Potassium Storage Performance Prussian Blue $K_2FeFe(CN)_6$ Doped with Nickel as a Superior Cathode : An Efficient Strategy to Enhance Potassium," 2019.

Chapter 9

Conclusions and Outlook

The present doctoral was focused on the investigation of functional materials for sodium-ion and potassium-ion batteries. Facile synthetic routes for advanced materials were pursued, and an in-depth investigation on the alkali-metal ion uptake reaction mechanism was carried out.
The results on nanostructured cobalt oxide conversion-type anode for SIBs, highlighted the importance of morphology control of the active material, and stressed the relevance of the reaction intermediates that form during the reaction. Indeed by *ex situ* X-Ray diffraction analysis, it was reported that after the first reduction, incomplete oxidation gives CoO, rather than Co_3O_4. This fact has significant consequences on the following de/sodiation cycles, as it may account for the decreased capacity after the first reduction.
A second, less expensive and more environmentally friendly, conversion-type anode anode candidate based on iron (III) oxide was analyzed. 1D nanofibres were be produced by cheap and easy scalable electrospinning method. The main issues of the oxide have been addressed by nanostructuring and by the addition of an aliovalent element during the synthesis of the oxide. It was found that the addition of Silicon, remarkably increased the transport properties, and significantly affected the crystal structure and morphology of the resulting material. Despite the voluntary exclusion of a carbon matrix during the synthesis, that might have improved the electrochemical performances, good rate capability and reasonable capacity retention were registered. Those properties were ascribed to the intrinsic properties of the nanostructured Si-doped fibers. Interestingly the fibrous morphology was maintained even after cycling, whereas the binder did not seem to be stable, as proven by the Raman and SEM analysis. This result suggests that meaningful performance improvement may arise from systematic study of the effect of the binder rather that focusing solely on the nanostructuring of the active material. Beyond the specific performances obtained for each

of the two conversion anodes that have been analyzed, it has been observed that different intermediates appear during the conversion reaction in SIBs. Compared to the analogous conversion reactions in LIBs it can be observed that the reaction for SIBs does not necessarily follow the same path, and that while the full reversible conversion of the TM oxide has been proved, the same does not always apply for SIBs where the obtained capacities are generally lower.

The research activity on potassium ion batteries focused on the selection of an appropriate electrolyte and the optimization of the cathode synthesis. A high throughput research activity allowed the investigation of a wide parameter space for the synthesis of the PBA cathode that lead to the selection of the most promising candidates. Their electrochemical properties were then analyzed and high capacity retention and extremely high, if compared to the literature, coulombic efficiency were proven. On the other hand, in the same electrolyte the graphite also revealed impressive long term stability (99% capacity retention after 400 cycles), excellent rate capability and reversible reaction mechanism as proved by the operando XRD analysis. Thanks to the natural abundance of graphite, and the easy co-precipitation synthesis of the manganese hexacyanoferrate, suitable for a low-cost industrial scale-up, potassium ion batteries based on these two active materials might find in the near future commercial application, provided that high energy and long term capacities can be maintained in full-cell KIBs.

As pointed out by the research work, all the different components of the cell must be carefully selected. In particular, the oxidative and reductive stability of the electrolyte, as well as the suppression of parasite reactions that may reduce the long term cyclability must never be neglected. Despite the fact that the different active materials for KIBs could in the future improve the performances of the current most promising ones, the results here presented revealed that ionic liquid electrolytes may be the ideal candidate for high voltage, high energy potassium full cells, as it has been proved that the employed electrolyte is compatible with both the anode (graphite) and the cathode (KMnHCFe) in half-cell.